Multiscale Modeling of Granular Materials

Yang Liu

Submitted in Partial Fulfillment of the
Requirements for the Degree
of Doctor of Philosophy
in the Graduate School of Arts and Sciences

Columbia University
2015

ABSTRACT

Multiscale Modeling of Granular Materials

Yang Liu

Granular materials have a “discrete” nature whose global mechanical behaviors are originated from the grain scale micromechanical mechanisms. The intriguing properties and non-trivial behaviors of a granular material pose formidable challenges to the multiscale modeling of these materials. Some of the key challenges include upscaling of coarse-scale continuum equation form fine-scale governing equations, calibrating material parameters at different scales, alleviating pathological mesh dependency in continuum models, and generating unit cells with versatile morphological details. This dissertation aims to addressing the aforementioned challenges and to investigate the mechanical behavior of granular materials through multiscale modeling.

Firstly, a three-dimensional nonlocal multiscale discrete-continuum model is presented for modeling the mechanical behavior of granular materials. We establish an information-passing coupling scheme between DEM that explicitly replicates granular motion of individual particles and a finite element continuum model, which captures nonlocal overall response of the granular assemblies. Secondly, a new staggered multilevel material identification procedure is developed for phenomenological critical state plasticity models. The emphasis is placed on cases in which available experimental data and constraints are insufficient for calibration. The key idea is to create a secondary virtual experimental database from high-fidelity models, such as discrete element simulations, then merge both the actual experimental data and secondary database as an extended digital database to determine material parameters for the phenomenological macroscopic critical state plasticity model. This expansion of database provides additional constraints necessary for calibration of the phenomenological critical state plasticity models.

Thirdly, a regularized phenomenological multiscale model is investigated, in which elastic properties are computed using direct homogenization and subsequently evolved using a simple three-parameter orthotropic continuum damage model. The salient feature of the model is a unified regularization framework based on the concept of effective softening strain. The unified regularization scheme is employed in the context of constitutive law rescaling and the staggered nonlocal approach to alleviate pathological mesh dependency. Lastly, a robust parametric model is presented for generating unit cells with randomly distributed inclusions. The proposed model is computationally efficient using a hierarchy of algorithms with increasing computational complexity, and is able to generate unit cells with different inclusion shapes.

Contents

List of Figures

List of Tables

Acknowledgments

From my heart I thank my husband Hao Sun who steadfastly loves me, supports me, and encourages me. He is a continuous source of inspiration that supports me to keep moving forward and underpins my persistence during my Ph.D. study at Columbia. It is his continued support that makes this work possible.

I would like to express my deepest gratitude to my doctoral supervisor Professor Jacob Fish for his continuous guidance and encouragement throughout my graduate study. Beyond his wealth of knowledge in the field of multiscale science and engineering, his energetic, creative and open mind to problem-solving have been motivational for me. His logical thoughts and expression with unique clarity make the courses and discussions more accessible and interesting, from which I benefited significantly. It is my privilege to work with him and I cannot thank him more for his persistent mentorship and his support of funding over my years of Ph.D. study.

During the last two years at Columbia, I enjoyed tremendous support from my co-advisor Professor WaiChing Sun, who has dedicated time and expertise unreservedly in mentoring me step-by-step and introduced me to a new research field of geomechanics, especially for granular materials. Professor Sun has taught me many valuable lessons, offered me plentiful advice and guidance in pursuing higher quality of work and independent thinking. His rigorous treatment of the subject matter has had a strong influence on the way I approach research and strengthened my desire as a dedicated scholar for a consistent and clear understanding of material response. I greatly appreciate the help and support he has given me. I treat it as my fortune to work with him.

I wish to extend my gratitude to my Ph.D. defense committee (Professors Jacob Fish, WaiChing Sun, Haim Waisman, Kristin Myers and Pierre Gentine) for their valuable comments, remarks and suggestions in completion of my dissertation.

I would like also to express my acknowledgement to Professor Huiming Yin who was my advisor during my master’s study at Columbia. He was very supportive during the period when I did independent research with him. My thanks are also due to other professors in the Department of Civil Engineering and Engineering Mechanics for their supports and guidance during my graduate studies.

I’m also indebted to many of my exceptional colleagues at Columbia. I’m greatly thankful to Vasilina Filonova, a respectful scientist and a great friend, who generously offered her expertise to help me at the early stage of my Ph.D. study. I also would like to thank Zifeng Yuan and Zheng Yuan for their collaborative efforts much of my work would not have been possible. I wish to gratefully acknowledge my other friends and colleagues at Columbia who made my Ph.D. life enjoyable. To name a few: Kailin Wang, Nan Hu, Yang Jiao, Yongxiang Wang, Dongming Feng, Dimitrios Fafalis, David Tal, Olga Brudastova, Mahesh Bailakanavar, Sergey Kuznetsov, Zhijun Cai, Kun Wang, Seonhong Na, etc.

Finally, my sincere thanks are given to my parents, Dezhou Liu and Runhua Hao, who always love and encourage me. Without their support, I could not have accomplish the Ph.D.

To my husband and my parents
who love, encourage and support me all the time

Chapter 1

Introduction

The introductory chapter presents a general introduction and outline of this dissertation.

Granular materials are ubiquitous in nature and industries, such as geophysics, geotechnical engineering, architecture, pharmaceutical and energy production. They surround our day-to-day life in various forms with the grains size as small as powder, sand, rice and coal, to sizes as large as icebergs and asteroids (see Figure 1.1).

A Granular material consists of solid particles, voids and interstitial air and/or liquid. Due to its amorphous structure, granular media can exhibits states as solid-like (quasi-static), liquid-like (granular flow) or gas-like. It can also switch its behavior from one state to another. In fact, many characterize granular materials as a new phase of matter due to its unique behaviors in each of these states, which are different from that of ordinary solids, liquids or gases. The intriguing properties and non-trivial behaviors of such an unusual form of matter have drawn physicists' interests.

Figure 1.1 Examples of typical granular materials: medicine manufacturing, sand dune, civil infrastructure engineering, etc.

(a) (b) (c)

Figure 1.2 Examples of accidents caused by granular material system failure: (a) landslide spurred by 1991 El earthquake, (b) avalanches, and (c) collapse of a silo

In addition to the academic curiosity, the study of granular behavior is also motivated by practical needs. One of the arduous issues in practice is the failure of a granular system, for instance, landslides, snow avalanches and collapse of granular containers, as shown in Figure 1.2 for a few among many other examples. The failure of granular systems could cause severe economic loss and casualties. For example, the transportation infrastructure is at risk of landslides in many areas worldwide [1]. An estimate of the total annual cost of landslide damage in the United States is in excess of one billion USD [2], which makes landslide one of the most costly natural disasters. Indeed, the pressing demand for resolving these practical issues, as well as the interests in encoding the physics behind many of the peculiar behaviors of granular materials, accelerated the development of predictive models capable of predicting the collective behavior of granular materials.

The development of predictive and robust models for granular materials remains a formidable challenge. Continuum theories, both classical [3] and generalized ones [4], have been widely applied for the analysis of granular behavior in engineering length scale by invoking nonlinear phenomenological models, such as elasticity [5], plasticity [6-8] and elastoplasticity [9-17]. In phenomenological models, granular materials are fundamentally treated as continua with material parameters being fitted to match the experimental data. The phenomenological models are able to capture many of the salient features of granular media, for instance, shear-dilatancy effects, stress-path dependency, pressure sensitivity, fabric anisotropy, liquefaction and cyclic mobility. Therefore, continuum approach remains the most widely used approach due to its versatility and efficiency. However, limitations of the continuum approach become evident when dealing with problems of increasing complexity, such as deformation bands [18, 19], landslides [20], and coupled thermo-hydro-chemo-mechanical processes during radioactive disposal [21], etc. Terzaghi [22] reflected on the very existence of this problem in soil mechanics and envisioned that:

> *"The way out of the difficulty lies in dropping the old fundamental principles and starting again from the elementary fact that the sand consists of individual grains."*

Micromechanics of granular materials, as an emerging discipline, was established to understand granular behavior from its most basic constituents, i.e. grains [23, 24]. First proposed by Cundall and Stack [25], the discrete (distinct) Element Methods have been extensively used to investigate micromechanical features of the granular assemblies. The widespread adoption of DEM in micromechanical analysis for granular materials has been has been reported in [26-29] including successful utilization in practice [30, 31]. Nevertheless, resolving kinematics of individual grains comes with the price of insurmountable computational cost for larger systems and longer simulation times. On the experimental side, over the past few years we have witnessed an explosion in the use of high-resolution tomographic techniques, which has enabled 2D and 3D measurements of microstructure, contact forces, and grain kinematics of natural geomaterials, and allowed for an increased understanding of the observed phenomena at the macroscale [32, 33]. As we gain more understanding at a granular scale from both advanced experimental measurements and DEM simulations, a key challenge that remains is to develop models that can accurately and efficiently predict the behavior of granular materials by integrating information at multiple scales.

Multiscale methods have emerged in mechanics to bridge different spatial and temporal scales [34]. Numerical methods for solving the representative volume element (RVE) problem, also known as *computational homogenization* methods, have been employed to derive overall behavior of heterogeneous media [35-39] (i.e. composite materials, polymers, metallic polycrystal, mixture of fluids) from the knowledge of fine-scale constituents with various types of boundary conditions. Remarkably, some efforts are being made lately to obtain realistic models for granular materials based on multiscale philosophy [40-50]. For instance, Wellmann and Wriggers [48] introduced an Arlequin DEM-FEM model that divides the spatial domain into discrete, continuum and overlapping subdomains. Li and Wan [51] and Regueiro and Yan [47] proposed bridging scale method which uses a handshake domain to couple particulate model with higher-order continua.

The homogenization-based multiscale discrete-continuum coupling formulation links the discrete representation with a continuum formalism at a finite strain. Miehe et al. [42, 46] extended Hill-Mandel microhomogeneity condition from continuous heterogeneous systems to granular media. Stránský and Jirásek [52] , Nguyen et al. [53] and Guo and Zhao [50] proposed a conceptually similar approach where homogenized stress measures and the tangent operator inferred from periodic discrete element simulations conducted on a representative volume element (RVE) are directly used to update an otherwise conventional small strain implicit finite element model [34, 54-56]. Andrade and Tu [45] proposed a staggered multiscale constitutive model in which evolutions of the yield surfaces and plastic potential are governed by DEM simulations or meso-scale experiments.

These methods have been successful to capturing most of the characteristic behavior of granular materials. Nevertheless, the application of multiscale modeling to granular materials is still in its embryonic stage due to the multidisciplinary nature of the problem, high computational cost and pathological mesh dependency [50]. Increasingly higher demands for predictive and efficient models continue posing challenges for numerical modeling of granular materials, many of which have not been overcome. These include but not limited to:

1) How to derive macroscopic continuum equation from a fine-scale discrete governing equation?
2) How to obtain good set of material parameters across different scales that can represent the overall behavior of granular material, such as sand?
3) How to alleviate mesh size dependency when using continuum models?
4) How to efficiently generate unit cells with versatile morphological details?

1.1 Dissertation outline

This dissertation focuses on the investigation of resolving the aforementioned issues by developing efficient predictive multiscale methods capable of realistic modeling of the mechanical behavior of granular materials. The first two chapters (Chapters 2 and 3) are the central theme of the research work, followed by two supporting chapters (Chapters 4 and 5) for detailed demonstration of the proposed methods. The following summarizes the outline of this dissertation:

- **Chapter 2**: This chapter presents a three-dimensional nonlocal multiscale discrete-continuum model for modeling mechanical behavior of granular materials. In the proposed multiscale scheme, we establish an information-passing mechanism between the discrete element method (DEM), which explicitly replicates granular motion of individual particles, and a finite element continuum model, which captures nonlocal macroscopic response of the granular assemblies. The resulting multiscale discrete-continuum coupling method retains the simplicity and efficiency of a continuum-based finite element model while circumventing mesh pathology in the post-bifurcation regime by means of a staggered nonlocal operator. We demonstrate that the multiscale coupling scheme is able to capture the plastic dilatancy and pressure-sensitive frictional responses commonly observed inside dilatant shear bands, without employing a phenomenological plasticity model at a macroscopic level. In addition, internal variables that govern path dependent behaviors, are now inferred directly from granular physics, without introducing unnecessary empirical relations and phenomenology. Simple shear and biaxial compression tests are used to analyze the onset and evolution of shear bands in granular materials and sensitivity to mesh density. The robustness and accuracy of the proposed multiscale model are verified in comparisons with single-scale benchmark DEM simulations.

- **Chapter 3:** This chapter presents a new staggered multilevel material identification procedure for phenomenological critical state plasticity models. The emphasis is placed on cases in which available experimental data and constraints are insufficient for calibration. The key idea is to create a secondary virtual experimental database from high-fidelity models, such as discrete element simulations, then merge both the actual experimental data and secondary database as an extended digital database to determine material parameters for the phenomenological macroscopic critical state plasticity model. The calibration procedure therefore consists of two steps. First, the material parameters of the DEM simulations are identified via the standard optimization procedure. Then, the calibrated DEM simulations are used to expand the experimental database with new simulated loading histories. This expansion of database provides additional constraints necessary for calibration of the phenomenological critical state plasticity models. The robustness of the proposed material identification framework is demonstrated in the context of the Dafalias-Manzari critical state plasticity model.
- **Chapter 4:** This chapter presents a regularized phenomenological multiscale model where elastic properties are computed using direct homogenization and subsequently evolved using a simple three-parameter orthotropic continuum damage model. The salient feature of the model is a unified regularization framework based on the concept of effective softening strain. The unified regularization scheme has been employed in the context of constitutive law rescaling and the staggered nonlocal approach. We show that an element erosion technique for crack

propagation when exercised with one of the two regularization schemes (i) possesses a characteristic length, (ii) is consistent with the fracture mechanics approach, and (iii) does not suffer from pathological mesh sensitivity.

- **Chapter 5:** This chapter presents a parametric model for generating unit cells with randomly distributed inclusions. The proposed algorithm possesses (i) robustness by yielding unit cells with inclusion volume fraction of up to 78%, (ii) computationally efficiency accomplished through a hierarchy of algorithms with increasing computational complexity, and (iii) versatility by generating unit cells with different inclusion shapes. A statistical study aimed at determining the effective size of the unit cell is conducted. The method has been applied to various random inclusion microstructure composites including: (i) polyurea or polyethene coating consisting of hard and soft domains (segments) employed for energy absorption in military and industrial applications, and (ii) fiber framework called fiberform embedded in an amorphous matrix used as heat shield on space crafts to prevent structural damage during reentry into the atmosphere.

Chapter 2

A Nonlocal Multiscale Discrete-Continuum Model for Predicting Mechanical Behavior of Granular Materials

In this chapter, a three-dimensional nonlocal multiscale discrete-continuum model is presented for modeling the mechanical behavior of granular materials. We establish an information-passing coupling between DEM, which explicitly replicates granular motion of individual particles, and a finite element continuum model, which captures nonlocal overall response of the granular assemblies. This chapter is reproduced from the paper co-authored with Waiching Sun, Zifeng Yuan and Jacob Fish, which was accepted for publication in the International Journal for Numerical Methods in Engineering [57].

2.1 Introduction

While the macroscopic response of granular materials may appear to be similar to that of continua, it essentially represents a collective behavior of interacting particles. For example, the rearrangement and crushing of particles, collapse of void space, buckling and splitting of force chains may result in path dependent behaviors at macroscopic scale, such as plastic dilatancy and contraction, non-associative plastic flow and strain localization.

Over the last three decades, computer simulations of granular motion have gained increasing attention. Several classes of models have been proposed to replicate the behaviors of granular media including:

(i) discrete approaches that explicitly model the particulate interactions among particle contacts at the grain scale,

(ii) continuum approaches that characterize path dependent responses with internal variables and constitutive laws at macroscopic scales, and

(iii) multiscale approaches that concurrently or by means of information-passing links both (i) and (ii).

The continuum approach has been widely used in mining, petroleum and geotechnical engineering problems to approximate the collective behavior of granular assemblies at the field scale. Phenomenological plasticity models that successfully resolve macroscopic behavior of specific types of granular materials, such as sand, silt and powder, have been extensively reported in the literature [6, 9, 58-65]. However, if no length scale is introduced in the phenomenological plasticity models, spurious mesh dependence may still occur at the post-bifurcation regime. Furthermore, phenomenological model relies on the usage of internal variables to replicate path dependent behaviors. It remains a difficult task to directly link or even replicate all different dissipation mechanisms originating from the grain scales, such as granular vertex and force chain buckling [18, 66, 67], by the evolution of internal variables alone.

The discrete element method (DEM) provides a simple but computationally intensive solution to resolve the aforementioned deficiencies of continuum approaches for granular media. In DEM, motion of grains is explicitly resolved based on contacts and long-range interactive mechanisms among particles [25, 44, 68-71]. Nevertheless, since DEM explicitly models and tracks the motion of each individual particle in the grain assembly, the computational cost is often too high for practical engineering problems that are in large spatial and time scales.

To overcome this issue, various concurrent and information-passing multiscale methods have been proposed to couple grain-scale simulations with macroscopic continuum-scale finite element analyses [42, 45-48, 50-53, 72]. For instance, Wellmann and Wriggers [48] introduced an Arlequin DEM-FEM model that divides the spatial domain into discrete and continuum subdomains. Parts of the discrete and continuum subdomains are overlapped with each other to create a handshake region such that spurious reflection can be suppressed. Li and Wan [51] and Regueiro and Yan [47] propose bridging scale method which uses a handshake domain to couple particulate model with higher-order continua.

As mentioned in Chapter 1, the homogenization-based multiscale discrete-continuum coupling technique is pioneered by Miehe et al. [42, 46] in which a micro-to-macro transition is established by locally attaching microstructures with macro-continuum at finite strain. Macroscopic stress tensor is then obtained from the DEM by deforming a periodic Lagrangian frame that contains the granular microstructures. Miehe et al. [42, 46] extended Hill-Mandel microhomogeneity condition from continuous heterogeneous systems to granular media. This study reveals that the responses obtained via the linear displacement and uniform stress boundary conditions represent the upper and lower bounds of the stiffness, while the periodic boundary condition is the optimal choice at which coarse-scale properties converges faster with respect to the RVE size.

Stránský and Jirásek [52] , Nguyen et al. [53] and Guo and Zhao [50] proposed a conceptually similar approach where homogenized stress measures and the tangent operator inferred from periodic discrete element simulations conducted on a representative volume element (RVE) are directly used to update an otherwise conventional small strain implicit finite element model [34, 54-56]. Andrade and Tu [45] proposed a staggered multiscale constitutive model in which evolutions of the yield surfaces and plastic potential are governed by DEM simulations or meso-scale experiments. This multiscale constitutive model is then used to update the Cauchy stress and consistent tangent operator of an implicit small strain finite element model. These information-passing DEM-FEM coupling approaches have proven to be stable. Nevertheless, both Nguyen et al. [53] and Guo and Zhao [50] concluded that the implicit DEM-FEM coupling model suffers two drawbacks – (i) the large number of DEM iteration steps required to reach local convergence and (ii) the pathological mesh dependence occurred after the onset of strain localization. Furthermore, while the computational cost of the information-passing DEM-FEM coupling model is substantially lower than of a single-scale DEM, the Newton-Raphson scheme used to update the finite element solution often requires multiple DEM simulations to achieve convergences. This can be a significant issue in the post softening regime where stress-strain curves obtained from DEM are typically bumpy and sensitive to perturbations. According to Guo and Zhao [50], the information-passing multiscale scheme may require as much as 48 DEM simulations for each quadrature point. Except [42, 46], the aforementioned hierarchical DEM-FEM coupling method are all formulated in the geometrically linear regime and thus may not be suitable for the shear band formation problems where significant plastic spin may develop as shown in [19].

In the present chapter, we develop a nonlocal multiscale discrete-continuum model based on the Generalized Mathematical Homogenization (GMH) originally developed for linking atomistic-continuum scales [34, 54-56]. GMH belongs to the category of information-passing multiscale methods, which evolve a coarse-scale model by advancing a sequence of fine-scale models in small windows (or RVEs) placed at the quadrature points of the finite element model. Consequently, GMH gives rise to a constitutive law-free coarse scale equations where the coarse scale continuum model is directly driven by discrete element simulations at the grain scales. The primary goal of the present work is to develop a hierarchical DEM-FEM coupling scheme that: (i) resolves both the overall and fine-scale response of the granular media, (ii) is computationally efficient, and (iii) overcomes pathological mesh sensitivity in the post-bifurcation regime. The contribution of the present work are summarized below:

(i) Alleviating mesh sensitivity in post-bifurcation regime. Previous hierarchical DEM-FEM coupling schemes have proven to be mesh dependence in [26, 27] after the onset of strain localization. The proposed multiscale approach remedies this issue by applying a modified staggered nonlocal approach proposed in [73, 74] to define the unit cell problem for the stress homogenization.

(ii) Formulating the two-scale continuum-discrete problem via the GMH framework. This treatment allows us to derive the Cauchy stress expression directly from the equilibrium equations of particle and provide a consistent framework that links the continuum (coarse-scale) and discrete (fine-scale) representations of the granular assemblies based on multiscale asymptotic analysis. We also establish the connection between the GMH and the Hill-Mandel condition and prove that the latter is a specific case of GMH in which coarse and fine scales are in the same temporal scales. [23, 24, 75].

The rest of the chapter is organized as follows. In Section 2.2, the governing equations at a scale of particles are briefly reviewed. The theoretical background established via GMH to obtain constitutive-law free coarse scale equations are then described, followed by the computational aspects of the proposed nonlocal multiscale scheme. Numerical examples, including a cyclic simple shear test, the monotonic simple shear test and the biaxial compression test, are presented in Section 2.3 to verify the model against a single-scale DEM simulation. Observations and conclusions are presented in Section 2.4.

2.2 Method

In this section, we provide the theoretical basis for the non-local multiscale scheme that couples the grain-scale discrete mechanics simulations and the macroscopic continuum model via a modified version of GMH, as depicted in Figure 2.1. We first formulate the micro-macro transition for the granular assemblies via a multiscale asymptotic analysis. This treatment allows one to associate the macroscopic quadrature point with unit cell consisting of particles. We then provide a brief description of the coarse scale finite element model that replicates the continuum scale behaviors and the unit cell discrete element method that replaces the macroscopic phenomenological internal variables to provide incremental constitutive update to the macroscopic problem. Due to the usage of the conditionally stable explicit scheme, we analyze the relations of the coarse- and fine-scale critical time step. The staggered scheme used to integrate the nonlocal quadrature is also discussed.

2.2.1 Micro-macro-transition for granular assemblies via asymptotic expansion

We consider a unit cell consisting of n particles. With the interior domain of the unit cell, these particles may exert contact force and torque on their neighboring particles. The initial position of particle I is denoted a $\mathbf{X}^I$, and its displacement is denoted as $\mathbf{u}^I$. Thus, the current position of I^{th} particle is

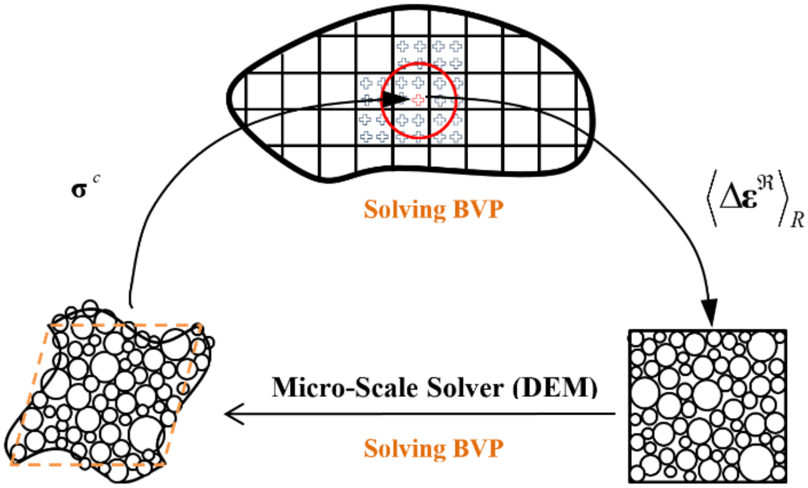

Figure 2.1 Information flow in the nonlocal two-scale discrete-continuum model. Note that $\left\langle \Delta\boldsymbol{\varepsilon}^{\Re} \right\rangle_R$ is the nonlocal coarse-scale corotational strain increment and $\boldsymbol{\sigma}^c$ is the coarse-scale Cauchy stress

$$\mathbf{x}^I = \mathbf{X}^I + \mathbf{u}^I \tag{2.1}$$

The distance of two particles I and J in the initial configuration is

$$\mathbf{X}^{IJ} = \mathbf{X}^J - \mathbf{X}^I \tag{2.2}$$

and in the current configuration is

$$\mathbf{x}^{IJ} = \mathbf{x}^J - \mathbf{x}^I = \mathbf{X}^{IJ} + \mathbf{u}^J \;\; \mathbf{X}^J, t \;\; - \mathbf{u}^I \;\; \mathbf{X}^I, t \tag{2.3}$$

Given the interaction between particles *I* and *J*, the EOM for particle *I* can thus be expressed by

$$m^I \ddot{\mathbf{u}}^I = \sum_{J \neq I} \mathbf{f}^{IJ}(\mathbf{x}^{IJ}) + \mathbf{F}^I_{\text{ext}} \tag{2.4}$$

where m^I is the mass of particle I ; $\ddot{\mathbf{u}}^I$ and $\dot{\mathbf{u}}^I$ are the acceleration and velocity of particle center of mass, respectively; $\mathbf{f}^{IJ}$ is the internal contact force applied to particle I by particle J ; $\mathbf{F}^I_{\text{ext}}$ is resultant external force applied to particle I , such as boundary force or body force. The superscript J denotes the neighboring particles that interact with particle I , such that $\left|\mathbf{x}^J - \mathbf{x}^I\right| < r_c$, with r_c being the cutoff radius. The mass of particle m^I , interval force $\mathbf{f}^{IJ}$ and external force $\mathbf{F}^I_{\text{ext}}$ are assumed to be periodic functions due to local periodicity of the grain assembly.

A particle moves against its neighboring particles by sliding and/or rolling at contact points. While the dominant role of sliding was considered in classical theories of strength and dilatancy of granular materials [76], previous research, such as Oda and Iwashita [77], suggest that rolling, rather than sliding, is a dominant micro-deformation mechanism leading to extensive dilatancy of granular media. Mühlhaus and Vardoulakis [78] conducted a bifurcation analysis based on a micropolar theory and successfully predicted the thickness of a shear band, as well as the shear band direction. Brown and Evans [79] questioned the need to incorporate micropolar terms for granular media, based on the fact that the coupled stress might be extremely small in most circumstances. In this chapter, we do not incorporate the rolling and torsional resistances. Since rotational stiffness is not introduced in our DEM model, higher-order kinematic measures, such as particles rotation gradient is not incorporated in the homogenized responses. The homogenized Cauchy stress tensor components are symmetric and no couple stress is required to formulate a complete set of the governing equations.

In the multiscale discrete-continuum method, two distinct spatial coordinates are employed to describe the heterogeneity at a grain level: (i) the coarse-scale coordinate, denoted by $\mathbf{X}$, in the coarse-scale domain $\mathbf{\Omega}$, at which the grain scale features are invisible, and (ii) the grain-scale or fine-scale coordinate, denoted by $\mathbf{Y}$, in the discrete unit cell domain $\boldsymbol{\Theta}$. Assuming that the dimension of heterogeneity is significantly smaller than the characteristic size of the macroscopic problem, the macro- and micro-scale coordinate systems of the reference configuration are related by

$$\mathbf{Y} = \mathbf{X}/\xi \tag{2.5}$$

where ξ is a small positive scaling parameter that $0 < \xi << 1$. The corresponding spatial scales in the current configuration are denoted by $\mathbf{x}$ and $\mathbf{y}$, respectively, and are related by $\mathbf{y} = \mathbf{x}/\xi$. We assume that the coarse-scale coordinate $\mathbf{X}$ takes continuous series of values and displacements $\mathbf{u}(\mathbf{X},\mathbf{Y},t)$ are continuous and differentiable in $\mathbf{X}$, while the fine-scale coordinate $\mathbf{Y}$ is discrete.

We follow the derivation steps in [34, 54-56] to derive the two-scale formation. However, unlike atomistic simulations that involve multiple time scales due to atomistic vibrations, a single time scale is considered. The first two material time derivatives of the displacement field are given by

$$\frac{d\mathbf{u}(\mathbf{X},\mathbf{Y}^I,t)}{dt} = \dot{\mathbf{u}}^I; \quad \frac{d^2\mathbf{u}(\mathbf{X},\mathbf{Y}^I,t)}{dt^2} = \ddot{\mathbf{u}}^I \tag{2.6}$$

Prior to carrying out the multiple scale asymptotic analysis it is necessary to rescale Equation (2.4). We start by considering the continuum equations of motion $\rho_0\ddot{\mathbf{u}}(\mathbf{X},t) - \nabla_{\mathbf{X}} \cdot \mathbf{P} = 0$ where ρ_0 is the mass density; $\mathbf{P}$ is the first Piola-Kirchhoff stress tensor; $\nabla_{\mathbf{X}} \cdot \mathbf{P}$ denotes the divergence of stress tensor $\mathbf{P}$. For homogeneous media, stress derivatives are of order one, whereas for heterogeneous media, for which certain components of stresses are discontinuous, stress derivatives are of $O(\xi^{-1})$. Assuming that the material density $\rho_0 \sim O(1)$ and the characteristic size of the unit cell $l \sim O(\xi)$ so that the volume of the unit cell $\Theta_0 \sim O(\xi^3)$. Thus, the mass $m \sim \rho_0\Theta_0 \sim O(\xi^3)$. Dividing Equation (2.4) by volume of the unit cell, yields

$$k_1\rho_0\ddot{\mathbf{u}}^I = \frac{1}{k_2\xi^3}\sum_{J\neq I}\mathbf{f}^{IJ}(\mathbf{x}^{IJ}) + \frac{1}{k_3\xi^3}\mathbf{F}^I_{\mathrm{ext}} \tag{2.7}$$

where k_1 and k_2 are order one constants. Comparing Equation (2.7) to the continuum equations of motion we obtain

$$\mathbf{f}^{IJ}(\mathbf{x}^{IJ}) \sim O(\xi^2), \quad \mathbf{F}_{ext} \sim O(\xi^2) \tag{2.8}$$

Then we introduce the following $O(1)$ normalized quantities

$$\bar{m} = m\big/\xi^3 \sim O(1)\ ;\ \bar{\mathbf{f}}^{IJ} = \mathbf{f}^{IJ}\big/\xi^2 \sim O(1)\ ;\ \bar{\mathbf{F}}_{ext} = \mathbf{F}_{ext}\big/\xi^2 \sim O(1) \tag{2.9}$$

Therefore Equation (2.4) can be rewritten as

$$\bar{m}\ddot{\mathbf{u}}^I = \frac{1}{\xi}\sum_{J\neq I}\bar{\mathbf{f}}^{IJ} + \frac{1}{\xi}\bar{\mathbf{F}}_{ext} \tag{2.10}$$

A multiscale asymptotic expansion is employed to approximate the displacement field

$$\mathbf{u}(\mathbf{X},\mathbf{Y},t) = \mathbf{u}^{(0)}(\mathbf{X},t) + \xi\mathbf{u}^{(1)}(\mathbf{X},\mathbf{Y},t) + \ldots \tag{2.11}$$

where the leading order displacement $\mathbf{u}^{(0)}$ is termed the coarse-scale displacement, $\mathbf{u}^c \equiv \mathbf{u}^{(0)}$. It is assumed to be independent of the fine-scale coordinate. Inserting Equation (2.11) into Equation (2.6) yields

$$\begin{aligned}\dot{\mathbf{u}}^I &= \dot{\mathbf{u}}^c + O(\xi)\\ \ddot{\mathbf{u}}^I &= \ddot{\mathbf{u}}^c + O(\xi)\end{aligned} \tag{2.12}$$

We denote the displacement of particle I by $u_i^I = u_i(\mathbf{X},\mathbf{Y}^I,t)$ with $\mathbf{X} = \mathbf{X}^I$. The displacements of the neighboring particle $u_i^J(\mathbf{X}^J,\mathbf{Y}^J,t)$ can be expanded using a Taylor series around point $\mathbf{X}$ as

$$u_i^J = u_i(\mathbf{X},\mathbf{Y}^J,t) + \frac{\partial u_i(\mathbf{X},\mathbf{Y}^J,t)}{\partial X_j}X_j^{IJ} + \frac{1}{2}\frac{\partial^2 u_i(\mathbf{X},\mathbf{Y}^J,t)}{\partial X_j\partial X_k}X_j^{IJ}X_k^{IJ} + \ldots \tag{2.13}$$

From Equation (2.13) we have

$$\begin{aligned} u_i^J - u_i^I &= u_i \;\; \mathbf{X}, \mathbf{Y}^J, t \;\; - u_i \;\; \mathbf{X}, \mathbf{Y}^I, t \;\; + \frac{\partial u_i \;\; \mathbf{X}, \mathbf{Y}^J, t}{\partial X_j} X_j^{IJ} + \\ &+ \frac{1}{2} \frac{\partial^2 u_i \;\; \mathbf{X}, \mathbf{Y}^J, t}{\partial X_j \partial X_k} X_j^{IJ} X_k^{IJ} + \ldots \end{aligned} \tag{2.14}$$

Inserting Equation (2.5) into Equation (2.14) yields

$$\begin{aligned} u_i^J - u_i^I &= u_i \;\; \mathbf{X}, \mathbf{Y}^J, t \;\; - u_i \;\; \mathbf{X}, \mathbf{Y}^I, t \;\; + \xi \frac{\partial u_i \;\; \mathbf{X}, \mathbf{Y}^J, t}{\partial X_j} Y_j^{IJ} \\ &+ \frac{1}{2} \xi^2 \frac{\partial^2 u_i \;\; \mathbf{X}, \mathbf{Y}^J, t}{\partial X_j \partial X_k} Y_j^{IJ} Y_k^{IJ} + \ldots \end{aligned} \tag{2.15}$$

Inserting the asymptotic expansion Equation (2.11) into Equation (2.15) yields

$$\begin{aligned} u_i^J - u_i^I &= \xi \left(u_i^{\;1} \;\; \mathbf{X}, \mathbf{Y}^J, t \;\; - u_i^{\;1} \;\; \mathbf{X}, \mathbf{Y}^I, t \;\; + \frac{\partial u_i^c \;\; \mathbf{X}, t}{\partial X_j} Y_j^{IJ} \right) \\ &+ \frac{1}{2} \xi^2 \left(\frac{\partial u_i^{\;1} \;\; \mathbf{X}, \mathbf{Y}^J, t}{\partial X_j} Y_j^{IJ} + \frac{1}{2} \frac{\partial^2 u_i^c \;\; \mathbf{X}, t}{\partial X_j \partial X_k} Y_j^{IJ} Y_k^{IJ} \right) + \ldots \end{aligned} \tag{2.16}$$

Inserting Equation (2.16) into Equation (2.3) yields

$$\begin{aligned} \mathbf{x}^{IJ} &= \mathbf{X}^{IJ} + \mathbf{u}^J - \mathbf{u}^I = \xi \boldsymbol{\varphi}^{IJ} + \xi^2 \boldsymbol{\psi}^{IJ} + \ldots \\ \mathbf{y}^{IJ} &= \mathbf{x}^{IJ} \big/ \xi = \boldsymbol{\varphi}^{IJ} + \xi \boldsymbol{\psi}^{IJ} + \ldots \end{aligned} \tag{2.17}$$

where

$$\begin{aligned} \varphi_i^{IJ} &= F_{ij}^c \;\; \mathbf{X} \;\; Y_j^{IJ} + u_i^{\;1} \;\; \mathbf{X}, \mathbf{Y}^J, t \;\; - u_i^{\;1} \;\; \mathbf{X}, \mathbf{Y}^I, t \\ \psi_i^{IJ} &= \frac{\partial u_i^{\;1} \;\; \mathbf{X}, \mathbf{Y}^J, t}{\partial X_j} Y_j^{IJ} + \frac{1}{2} \frac{\partial^2 u_i^c \;\; \mathbf{X}}{\partial X_j \partial X_k} Y_j^{IJ} Y_k^{IJ} \end{aligned} \tag{2.18}$$

Herein, $F_{ij}^c \;\; \mathbf{X}, t$ denotes the coarse-scale deformation gradient, expressed as

$$F_{ij}^c \;\; \mathbf{X} \;\; = \delta_{ij} + \frac{\partial u_i^c \;\; \mathbf{X}}{\partial X_j} \tag{2.19}$$

The contact force $\mathbf{f}^{IJ}$ is a function of $\mathbf{x}^{IJ}$ so that

$$\begin{aligned} \bar{f}_i^{IJ} &= \bar{f}_i^{IJ}\ \ \xi\mathbf{y}^{IJ}\ \ = \bar{f}_i^{IJ}\ \ \xi\boldsymbol{\varphi}^{IJ} + \xi^2\boldsymbol{\psi}^{IJ} + \dots \\ &= \bar{f}_i^{IJ}\ \ \xi\boldsymbol{\varphi}^{IJ}\ \ + \left.\frac{\partial \bar{f}_i^{IJ}}{\partial y_k^{IJ}}\frac{\partial y_k^{IJ}}{\partial x_j^{IJ}}\right|_{\mathbf{y}^{IJ}=\boldsymbol{\varphi}^{IJ}} \xi^2\psi_j^{IJ} + O\ \ \xi^2 \\ &= \tilde{\bar{f}}_i^{IJ} + \xi \left.\frac{\partial \bar{f}_i^{IJ}}{\partial y_j^{IJ}}\right|_{\mathbf{y}^{IJ}=\boldsymbol{\varphi}^{IJ}} \psi_j^{IJ} + O\ \ \xi^2 \end{aligned} \tag{2.20}$$

where

$$\tilde{\bar{f}}_i^{IJ} = \tilde{\bar{f}}_i^{IJ}\ \ \xi\boldsymbol{\varphi}^{IJ} \tag{2.21}$$

Inserting Equations (2.12) and (2.20) into Equation (2.10) yields

$$\bar{m}^I\ddot{u}_i^c\ \ \mathbf{X},t\ \ = \frac{1}{\xi}\sum_{J\neq I}\left(\hat{\bar{f}}_i^{IJ} + \xi \left.\frac{\partial \bar{f}_i^{IJ}}{\partial y_j^{IJ}}\right|_{\mathbf{y}^{IJ}=\boldsymbol{\varphi}^{IJ}} \psi_j^{IJ}\right) + \frac{1}{\xi}\bar{F}_{ext,i}\ \ \mathbf{u}^I \tag{2.22}$$

Collecting terms of equal power of ξ gives the equations of motion at different scales

$$O\ \ \xi^{-1}\ \ :\quad \sum_J \tilde{f}_i^{IJ} + \bar{F}_{ext,i}\ \ \mathbf{u}^I\ \ = 0 \tag{2.23}$$

$$O\ \ 1\ \ :\quad m\ddot{u}_i^c\ \ \mathbf{X},t\ \ = \sum_J\left(\left.\frac{\partial f_i^{IJ}}{\partial y_j^{IJ}}\right|_{\mathbf{y}^{IJ}=\boldsymbol{\varphi}^{IJ}} \psi_j^{IJ}\right) \tag{2.24}$$

Equation (2.23) is a quasi-static unit cell problem. We now focus on the coarse scale problem.

Summation over all particles and then dividing the equation by the volume of the unit cell $\left|\Theta_0\right|$ for the initial configuration give

$$\frac{1}{\left|\Theta_0\right|}\sum_I m^I\ddot{u}_i^c\ \ \mathbf{X},t\ \ = \frac{1}{\left|\Theta_0\right|}\sum_I\sum_J \left.\frac{\partial f_i^{IJ}}{\partial y_j^{IJ}}\right|_{\mathbf{y}^{IJ}=\boldsymbol{\varphi}^{IJ}} \psi_j^{IJ} \tag{2.25}$$

It is noted that the density is defined as

$$\rho_0^c = \frac{1}{\left|\Theta_0\right|}\sum_I m^I \tag{2.26}$$

so that

$$\rho_0^c \ddot{u}_i^c \;\; \mathbf{X}, t \;\; = \frac{1}{\left|\Theta_0\right|}\sum_I\sum_J \left.\frac{\partial f_i^{IJ}}{\partial y_j^{IJ}}\right|_{\mathbf{y}^{IJ}=\boldsymbol{\varphi}^{IJ}} \psi_j^{IJ} \tag{2.27}$$

Considering Equations (2.17) and (2.18), we have

$$\begin{aligned} f_{i,X_j}^{IJ} &= \frac{\partial f_i^{IJ}}{\partial y_k^{IJ}}\frac{\partial y_k^{IJ}}{\partial X_j} = \frac{\partial f_i^{IJ}}{\partial y_k^{IJ}}\frac{\partial \varphi_k^{IJ}}{\partial X_j} + O \;\; \xi \\ &= \frac{\partial f_i^{IJ}}{\partial y_k^{IJ}}\left(\frac{\partial^2 u_k^c \;\; \mathbf{X}, t}{\partial X_m \partial X_j} Y_m^{IJ} + \frac{\partial u_k^{\;\;1} \;\; \mathbf{X}, \mathbf{Y}^J, t}{\partial X_j} - \frac{\partial u_k^{\;\;1} \;\; \mathbf{X}, \mathbf{Y}^I, t}{\partial X_j}\right) + O \;\; \xi \end{aligned} \tag{2.28}$$

In the RHS of Equation (2.27)

$$\begin{aligned} &\left.\frac{\partial f_i^{IJ}}{\partial y_j^{IJ}}\right|_{\mathbf{y}^{IJ}=\boldsymbol{\varphi}^{IJ}} \psi_j^{IJ} \\ &= \left.\frac{\partial f_i^{IJ}}{\partial y_j^{IJ}}\right|_{\mathbf{y}^{IJ}=\boldsymbol{\varphi}^{IJ}} \left(\frac{\partial u_j^{(1)}\left(\mathbf{X}, \mathbf{Y}^J, t\right)}{\partial X_m} + \frac{1}{2}\frac{\partial^2 u_j^c\left(\mathbf{X}\right)}{\partial X_m \partial X_k} Y_k^{IJ}\right) Y_m^{IJ} \\ &= \frac{1}{2}\left.\frac{\partial f_i^{IJ}}{\partial y_j^{IJ}}\right|_{\mathbf{y}^{IJ}=\boldsymbol{\varphi}^{IJ}} \left(\frac{\partial u_j^{(1)}\left(\mathbf{X}, \mathbf{Y}^J, t\right)}{\partial X_m} - \frac{\partial u_j^{(1)}\left(\mathbf{X}, \mathbf{Y}^I, t\right)}{\partial X_m} + \frac{\partial^2 u_j^c\left(\mathbf{X}\right)}{\partial X_m \partial X_k} Y_k^{IJ}\right) Y_m^{IJ} \\ &\quad + \frac{1}{2}\left.\frac{\partial f_i^{IJ}}{\partial y_j^{IJ}}\right|_{\mathbf{y}^{IJ}=\boldsymbol{\varphi}^{IJ}} \left(\frac{\partial u_j^{(1)}\left(\mathbf{X}, \mathbf{Y}^J, t\right)}{\partial X_m} + \frac{\partial u_j^{(1)}\left(\mathbf{X}, \mathbf{Y}^I, t\right)}{\partial X_m}\right) Y_m^{IJ} \\ &= \frac{1}{2}\frac{\partial}{\partial X_j}\left(f_i^{IJ} Y_j^{IJ}\right) + \frac{1}{2}\left.\frac{\partial f_i^{IJ}}{\partial y_j^{IJ}}\right|_{\mathbf{y}^{IJ}=\boldsymbol{\varphi}^{IJ}} \left(\frac{\partial u_j^{(1)}\left(\mathbf{X}, \mathbf{Y}^J, t\right)}{\partial X_m} + \frac{\partial u_j^{(1)}\left(\mathbf{X}, \mathbf{Y}^I, t\right)}{\partial X_m}\right) Y_m^{IJ} \\ &= \frac{1}{2\xi}\frac{\partial}{\partial X_j}\left(f_i^{IJ} X_j^{IJ}\right) + \frac{1}{2}\left.\frac{\partial f_i^{IJ}}{\partial y_j^{IJ}}\right|_{\mathbf{y}^{IJ}=\boldsymbol{\varphi}^{IJ}} \left(\frac{\partial u_j^{(1)}\left(\mathbf{X}, \mathbf{Y}^J, t\right)}{\partial X_m} + \frac{\partial u_j^{(1)}\left(\mathbf{X}, \mathbf{Y}^I, t\right)}{\partial X_m}\right) Y_m^{IJ} \end{aligned} \tag{2.29}$$

Inserting Equation (2.29) into Equation (2.27) yields

$$
\begin{aligned}
\rho_0^c \ddot{u}_i^c(\mathbf{X},t) &= \sum_I \sum_J \frac{1}{|\Theta_0|}\frac{1}{2}\frac{\partial}{\partial X_j}\left(f_i^{IJ} X_j^{IJ}\right) \\
&+ \sum_I \sum_J \frac{1}{|\Theta_0|}\frac{1}{2}\left.\frac{\partial f_i^{IJ}}{\partial y_j^{IJ}}\right|_{\mathbf{y}^{IJ}=\boldsymbol{\varphi}^{IJ}} \left(\frac{\partial u_j^{(1)}(\mathbf{X},\mathbf{Y}^J,t)}{\partial X_m} + \frac{\partial u_j^{(1)}(\mathbf{X},\mathbf{Y}^I,t)}{\partial X_m}\right) Y_m^{IJ}
\end{aligned}
\tag{2.30}
$$

It is shown that the second term of Equation (2.30) will vanish. Recall Equation (2.3),

$$
\mathbf{x}^{JI} = \mathbf{x}^I - \mathbf{x}^J = \mathbf{X}^I - \mathbf{X}^J + \mathbf{u}^I - \mathbf{u}^J = -\mathbf{x}^{IJ} = \xi\boldsymbol{\varphi}^{JI} + \xi^2 \boldsymbol{\psi}^{JI}(\mathbf{X},\mathbf{Y},t) + \ldots \tag{2.31}
$$

where

$$
\begin{aligned}
\varphi_i^{JI} &= F_{ij}^c(\mathbf{X},t)\, Y_j^{JI} + u_i^{(1)}(\mathbf{X},\mathbf{Y}^I,t) - u_i^{(1)}(\mathbf{X},\mathbf{Y}^J,t) = -\varphi_i^{IJ} \\
\psi_i^{JI} &= \frac{\partial u_i^{(1)}(\mathbf{X},\mathbf{Y}^I,t)}{\partial X_j} Y_j^{JI} + \frac{1}{2}\frac{\partial^2 u_i^c(\mathbf{X})}{\partial X_j \partial X_k} Y_j^{JI} Y_k^{JI} = -\psi_i^{IJ}
\end{aligned}
\tag{2.32}
$$

According to Newton’s third law, we have

$$
\mathbf{f}^{IJ} = -\mathbf{f}^{JI} \tag{2.33}
$$

From Equations (2.32) and (2.33), we have the relationship as follows

$$
\frac{\partial f_i^{IJ}}{\partial y_j^{IJ}} = -\frac{\partial f_i^{JI}}{\partial y_j^{IJ}} = -\frac{\partial f_i^{JI}}{\partial\left(-y_j^{JI}\right)} = \frac{\partial f_i^{JI}}{\partial y_j^{JI}} \tag{2.34}
$$

The summation of the second term of Equation (2.30) gives

$$
\begin{aligned}
&\sum_I \sum_J \frac{1}{|\Theta_0|}\frac{1}{2}\left.\frac{\partial f_i^{IJ}}{\partial y_j^{IJ}}\right|_{\mathbf{y}^{IJ}=\boldsymbol{\varphi}^{IJ}} \left(\frac{\partial u_j^{(1)}(\mathbf{X},\mathbf{Y}^J,t)}{\partial X_m} + \frac{\partial u_j^{(1)}(\mathbf{X},\mathbf{Y}^I,t)}{\partial X_m}\right) Y_m^{IJ} \\
&= \sum_I \sum_J \frac{1}{|\Theta_0|}\frac{1}{2}\left.\frac{\partial f_i^{IJ}}{\partial y_j^{IJ}}\right|_{\mathbf{y}^{IJ}=\boldsymbol{\varphi}^{IJ}} \left(\frac{\partial u_j^{(1)}(\mathbf{X},\mathbf{Y}^J,t)}{\partial X_m} + \frac{\partial u_j^{(1)}(\mathbf{X},\mathbf{Y}^I,t)}{\partial X_m}\right)\left(Y_m^J - Y_m^I\right)
\end{aligned}
\tag{2.35}
$$

For any pair (I,J) which participates the summation, we have

$$
\begin{aligned}
&\frac{1}{2}\frac{\partial f_i^{IJ}}{\partial y_j^{IJ}}\Bigg|_{\mathbf{y}^{IJ}=\boldsymbol{\varphi}^{IJ}}\left(\frac{\partial u_j^{(1)}\left(\mathbf{X},\mathbf{Y}^J,t\right)}{\partial X_m}+\frac{\partial u_j^{(1)}\left(\mathbf{X},\mathbf{Y}^I,t\right)}{\partial X_m}\right)\left(Y_m^J-Y_m^I\right)\\
&+\frac{1}{2}\frac{\partial f_i^{JI}}{\partial y_j^{JI}}\Bigg|_{\mathbf{y}^{JI}=\boldsymbol{\varphi}^{JI}}\left(\frac{\partial u_j^{(1)}\left(\mathbf{X},\mathbf{Y}^I,t\right)}{\partial X_m}+\frac{\partial u_j^{(1)}\left(\mathbf{X},\mathbf{Y}^J,t\right)}{\partial X_m}\right)\left(Y_m^I-Y_m^J\right)\\
&=\frac{1}{2}\frac{\partial f_i^{IJ}}{\partial y_j^{IJ}}\Bigg|_{\mathbf{y}^{IJ}=\boldsymbol{\varphi}^{IJ}}\left(\frac{\partial u_j^{(1)}\left(\mathbf{X},\mathbf{Y}^J,t\right)}{\partial X_m}+\frac{\partial u_j^{(1)}\left(\mathbf{X},\mathbf{Y}^I,t\right)}{\partial X_m}\right)\left(Y_m^J-Y_m^I\right)\\
&+\frac{1}{2}\frac{\partial f_i^{IJ}}{\partial y_j^{IJ}}\Bigg|_{\mathbf{y}^{IJ}=\boldsymbol{\varphi}^{IJ}}\left(\frac{\partial u_j^{(1)}\left(\mathbf{X},\mathbf{Y}^I,t\right)}{\partial X_m}+\frac{\partial u_j^{(1)}\left(\mathbf{X},\mathbf{Y}^J,t\right)}{\partial X_m}\right)\left(Y_m^I-Y_m^J\right)=0
\end{aligned}
\tag{2.36}
$$

Finally, the coarse-scale equation of motion is expressed as

$$
\rho_0^c\ddot{u}_i^c\ \ \mathbf{X},t\ \ =\sum_I\sum_J\frac{1}{\left|\Theta_0\right|}\frac{1}{2}\frac{\partial}{\partial X_j}\ \ f_i^{IJ}X_j^{IJ}
\tag{2.37}
$$

One can rewrite Equation (2.37) as

$$
\begin{aligned}
&\rho_0^c\ddot{u}_i^c\ \ \mathbf{X},t\ \ -\frac{\partial P_{ij}\ \ \mathbf{X},t}{\partial X_j}=0\\
&P_{ij}\ \ \mathbf{X},t\ \ =\frac{1}{2\left|\Theta_0\right|}\sum_I\sum_J f_i^{IJ}X_j^{IJ}
\end{aligned}
\tag{2.38}
$$

Alternatively, we have

$$
P_{ij}\ \ \mathbf{X},t\ \ =\frac{1}{\left|\Theta_0\right|}\sum_{I=1}^{n}\sum_{J>I}f_i^{IJ}X_j^{IJ}
\tag{2.39}
$$

where n denotes the total number of particles in the unit cell.

Equation (2.39) can be also derived in the current configuration. Considering the relationship between the first Piola-Kirchhoff stress and Cauchy stress, we have

$$
\begin{aligned}
&\mathbf{P}=J\boldsymbol{\sigma}\cdot\mathbf{F}^{-T}\\
&\boldsymbol{\sigma}=\mathbf{P}\cdot\mathbf{F}^{T}\big/J
\end{aligned}
\tag{2.40}
$$

where J is the determinant of deformation gradient. Inserting Equation (2.39) into Equation (2.40) yields

$$\begin{aligned}\sigma_{ij} &= \frac{1}{J}P_{ik}F_{jk} = \frac{1}{J}\frac{1}{\left|\Theta_0\right|}\sum_{I=1}^{n}\sum_{J>I} f_i^{IJ}X_k^{IJ}F_{jk} \\ &= \frac{1}{\left|\Theta\right|}\sum_{I=1}^{n}\sum_{J>I} f_i^{IJ} \quad F_{jk}X_k^{IJ}\end{aligned} \tag{2.41}$$

where $\left|\Theta\right|$ denotes the volume of the unit cell in the current configuration. From Equations (2.17) and (2.18), we have

$$\begin{aligned}\mathbf{x}^{IJ} &= \xi \;\; \mathbf{F}^c \cdot \mathbf{Y}^{IJ} + \mathbf{u}^{\,1} \quad \mathbf{X}, \mathbf{Y}^J, t \;\; - \mathbf{u}^{\,1} \quad \mathbf{X}, \mathbf{Y}^I, t \quad + O \;\; \xi^2 \\ &= \mathbf{F}^c \cdot \mathbf{X}^{IJ} + O \;\; \xi\end{aligned} \tag{2.42}$$

Inserting Equation (2.42) into Equation (2.41) yields

$$\sigma_{ij} = \frac{1}{\left|\Theta\right|}\sum_{I=1}^{n}\sum_{J>I} f_i^{IJ} \quad F_{jk}X_k^{IJ} \quad = \frac{1}{\left|\Theta\right|}\sum_{I=1}^{n}\sum_{J>I} f_i^{IJ}x_j^{IJ} + O \;\; \xi \tag{2.43}$$

According to Equation (2.39) and (2.41), both the first Piola-Kirchhoff stress and Cauchy stress can be derived from the multiscale asymptotic analysis. The coarse-scale problem that governs macroscopic continuum behavior and the unit cell problem that replaces the macroscopic phenomenological constitutive laws can be expressed in the current configuration, which read,

(a) Coarse-scale problem

$$\begin{aligned}\rho^c \ddot{\mathbf{u}}^c \;\; \mathbf{x}, t \;\; - \nabla_{\mathbf{x}} \cdot \boldsymbol{\sigma}^c &= \mathbf{0} \\ \boldsymbol{\sigma}^c \;\; \mathbf{x}, t &= \frac{1}{\left|\Theta\right|}\sum_{I=1}^{n}\sum_{J>I} \mathbf{f}^{IJ}\mathbf{x}^{IJ}\end{aligned} \tag{2.44}$$

(b) Unit cell problem

$$\sum_J \mathbf{f}_i^{IJ} + \mathbf{F}_{ext,i} \;\; \mathbf{u}^I \;\; = \mathbf{0} \tag{2.45}$$

where $\ddot{\mathbf{u}}^c$ denotes the coarse-scale acceleration; $\rho^c = \frac{1}{\left|\Theta\right|}\sum_I m^I$ and $\left|\Theta\right|$ are the coarse-scale mass density and the unit cell volume in the current configuration, respectively; n

is the number of particles in the unit cell; $\boldsymbol{\sigma}^c$ is the coarse-scale Cauchy stress and $\mathbf{x}^{IJ}$ is the vector connecting the centers of two particles; $\nabla \cdot$ denotes the divergence operator; superscript c denotes the coarse-scale features. The Cauchy stress obtained in Equation (2.44)b is identical to the classical homogenized Cauchy stress obtained using Principal of Virtual Work [23, 24, 44, 75].

Note that the inertia term in Equation (2.4) only enters the coarse-scale equation of motion, whereas the unit cell problem remains quasi-static. This is due to the fact that the coarse-scale wave length is assumed to be much larger than the RVE size. This approach is commonly used for low rates of loading and for short observation times [34, 80]. However, in those problems with high rates of loading and long observation times, particle interfaces in a granular media may cause reflection and refraction of stress waves, giving rise to dispersion and attenuation of waves within material microstructure [81], which cannot be accounted for by the approach developed in this chapter.

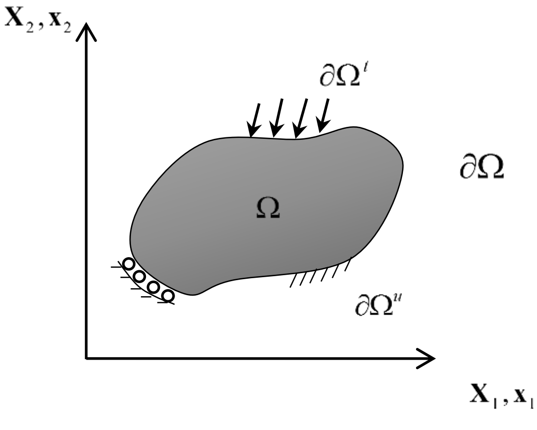

Figure 2.2 Schematics of the coarse-scale boundary value problem (in the initial configuration)

2.2.2 Coarse-scale problem: FEM

In the macroscopic continuum scale, the trajectories of individual particles are not considered. Instead, we associate each coarse-scale material point with a representative elementary volume or unit cell in which effective continuum properties can be derived. As a result, the coarse scale displacement field is interpolated by the finite element basis function and possesses C^0 continuity. The initial and boundary conditions for the coarse-scale problem described by Equation (2.44) are given as

$$\mathbf{u}^c \;\; \mathbf{x},0 \;\; = \mathbf{0}; \qquad \dot{\mathbf{u}}^c \;\; \mathbf{x},0 \;\; = \mathbf{0} \tag{2.46}$$

$$\mathbf{u}^c \;\; \mathbf{x},t \;\; = \bar{\mathbf{u}} \;\; \mathbf{x},t \qquad \text{on} \quad \partial\Omega^u; \qquad \boldsymbol{\sigma}^c \cdot \mathbf{n} = \bar{\mathbf{t}} \qquad \text{on} \quad \partial\Omega^t \tag{2.47}$$

where the essential (displacement) boundary $\partial\Omega^u$ and the natural (traction) boundary $\partial\Omega^t$ satisfy $\partial\Omega^u \bigcup \partial\Omega^t = \partial\Omega$ and $\partial\Omega^u \bigcap \partial\Omega^t = 0$, as shown in Figure 2.2; $\dot{\mathbf{u}}^c$ is the velocity vector; $\bar{\mathbf{u}}$ and $\bar{\mathbf{t}}$ represent prescribed displacements and tractions on $\partial\Omega^u$ and $\partial\Omega^t$, respectively; $\mathbf{n}$ is the unit outward norm of the boundary.

The weak form of the coarse-scale problem in Equation (2.44)a is stated as follows. Find $\mathbf{u}^c \;\; \mathbf{x},t \;\; \in \mathcal{U}$ in Ω such that

$$\int_\Omega \nabla_{\mathbf{x}} \cdot \mathbf{w}^c \;\; \cdot \boldsymbol{\sigma}^c d\Omega = \int_{\partial\Omega^t} \mathbf{w}^c \cdot \bar{\mathbf{t}} d\Omega - \int_\Omega \rho^c \mathbf{w}^c \cdot \ddot{\mathbf{u}}^c d\Omega \qquad \forall \mathbf{w}^c \in \mathcal{W} \tag{2.48}$$

where the trial and test function spaces are defined as

$$\begin{aligned} \mathcal{U} &= \;\; \mathbf{u}^c \mid \mathbf{u}^c \in \mathcal{H}^1, \mathbf{u}^c = \bar{\mathbf{u}}^c \text{ on } \partial\Omega^u \\ \mathcal{W} &= \;\; \mathbf{w}^c \mid \mathbf{w}^c \in \mathcal{H}^1, \mathbf{w}^c = 0 \text{ on } \partial\Omega^u \end{aligned} \tag{2.49}$$

where $\mathbf{u}^c$ and $\mathbf{w}^c$ are the coarse-scale trial and test functions, respectively, and $\mathcal{H}^1$ is the Sobolev space of order one.

Consider the following discretization of the coarse-scale trial and test functions

$$\begin{aligned} {}^h\mathbf{u}^c \;\; \mathbf{x},t \;\; &= \sum_{A\in\aleph} \mathbf{N}_{\mathrm{A}} \;\; \mathbf{x} \;\; \mathbf{d}^c_{\mathrm{A}} \;\; t \\ {}^h\mathbf{w}^c \;\; \mathbf{x},t \;\; &= \sum_{A\in\aleph} \mathbf{N}_{\mathrm{A}} \;\; \mathbf{x} \;\; \mathbf{w}^c_{\mathrm{A}} \;\; t \end{aligned} \tag{2.50}$$

which yields a semidiscrete momentum equation

$$\mathbf{M}\ddot{\mathbf{d}}^{c}\ \ t\ \ = \mathbf{f}^{\text{ext}}\ \ t\ \ - \mathbf{f}^{\text{int}}\ \ \mathbf{d}^{c}\ \ t \tag{2.51}$$

where $\mathbf{N}_{\mathrm{A}}$ is a shape function corresponding to node A; $\aleph$ represents the set of nodes in the mesh; $\mathbf{d}_{\mathrm{A}}^{c}\ \ t$ and $\mathbf{w}_{\mathrm{A}}^{c}\ \ t$ denote the nodal degrees-of-freedom of trial and test functions, respectively; the superscript h represents the discretized quantities; $\mathbf{d}^{c}$ and $\ddot{\mathbf{d}}^{c}$ are the coarse-scale nodal displacements and accelerations, respectively; $\mathbf{M}$, $\mathbf{f}^{\text{int}}$ and $\mathbf{f}^{\text{ext}}$ are the coarse-scale mass matrix, internal force and external force vectors, respectively, defined as

$$\mathbf{M} = \int_{\Omega} \rho^{c} \mathbf{N}^{T} \mathbf{N} d\Omega; \quad \mathbf{f}^{\text{int}} = \int_{\Omega} \mathbf{B}^{T} \boldsymbol{\sigma}^{c} d\Omega; \quad \mathbf{f}^{\text{ext}} = \int_{\Omega} \mathbf{N}^{T} \bar{\boldsymbol{t}}^{c} d\Omega \tag{2.52}$$

where $\mathbf{N}$ and $\mathbf{B}$ are the coarse-scale shape functions and their symmetric gradients, respectively; $\boldsymbol{\sigma}^{c}$ is the coarse-scale Cauchy defined by Equation (2.44)b.

In the present work, the continuum coarse-scale problem in Equation (2.51) is integrated using explicit central difference method [82]. Lumped mass is used in the coarse-scale simulations. Unlike the conventional macroscopic finite element approach, the constitutive responses are not obtained from macroscopic constitutive law but rather from homogenized responses of particle assemblies associated with every quadrature points in the finite element mesh.

2.2.3 Discrete element unit cell problem

Consider a collection of particles within the interior domain of a cuboidal unit cell. This collection of particles is surrounded by an exterior layer of one-particle thickness. This exterior layer deforms periodically in space and may interact with the particles inside the unit cell but its motion is completely controlled by the prescribed periodic boundary conditions provided by the coarse-scale problem. The particle-to-particle and particle-to-boundary interactions are both simulated via discrete element method and the quasi-static macroscopic responses of the unit cell are subsequently homogenized from each unit cell and passed to the coarse-scale solver.

The quasi-static solution of the unit cell problem in Equation (2.45) can be obtained by seeking the steady-state solution of an explicit dynamic relaxation DEM problem with incremental loading steps or by directly solving the nonlinear system of equations via an implicit scheme. In practice, the implicit scheme is rarely used for DEM problems. As the nonlinearity of responses may stem from both the nonlinear and path dependent contact laws and the changes of topologies of grain contacts, it is easier to implement and use explicit scheme to obtain the quasi-static solution of DEM assemblies. The dynamic relaxation problem can be viewed as an iterative process in which pseudo-dynamics processes are emulated in an artificial time scale. This iterative process is considered complete when a deformed configuration of the granular assembly with all the forces and moment in equilibrium is found. Using numerical examples to provide evidences, Bardet and Proubet [83] show that both mass scaling and viscous damping can be used to enhance computational efficiency (by reducing number of iterative steps) without significantly altering the approximated quasi-static configurations of the DEM assemblies. In this chapter, an explicit central difference leap-frog pseudo-time integrator and artificial damping are both employed to obtain the quasi-static solution [25].

2.2.3.1 Contact models for discrete element simulations in unit cells

A simplified contact model, the frictional Hertz-Mindlin mechanism with viscous damping, is used to represent the particle contact mechanism. Cohesive bonding and rolling resistance between the particles are not considered in this chapter. Incremental changes to the normal and tangential contact forces, f_n^f and f_t^f , at each contact are determined by the particle shear modulus G_g^f, Poisson ratio ν^f, radii of the contacting grains R_1 and R_2, and the fine-scale normal and tangential displacements at the contact, $d\delta^f$ and ds^f [49],

$$df_n^f = k_n^f d\delta^f; \qquad k_n^f = \frac{\sqrt{2}G_g^f\sqrt{R^e}}{1-\nu^f}\;{\delta^f}^{\;1/2} \tag{2.53}$$

$$df_t^f = k_t^f ds^f; \qquad k_t^f = \frac{2\sqrt{2}G_g^f\sqrt{R^e}}{2-\nu^f}\;{\delta^f}^{\;1/2} \tag{2.54}$$

where δ^f is the indentation at the contact and R^e is the effective radius,

$$R^e = \frac{2R_1R_2}{R_1+R_2} \tag{2.55}$$

Superscript f denotes fine-scale features. The fine-scale tangential force is governed by the friction coefficient μ^f, such that $\left|f_t^f\right| \le \mu^f f_n^f$. For stabilization, a viscous damping force is employed

$$f_{s,vis}^f = C^f \dot{s}^f \tag{2.56}$$

where C^f and $\dot{s}^f$ are the viscosity and the tangential sliding velocity at contact. In case of slow, quasi-static loading conditions, the mass damping c^I and contact damping C^f must be sufficient to dissipate high frequency vibrational modes without impeding particle motion that arise from particle interactions or the boundary conditions.

2.2.3.2 Dynamic relaxation scheme of unit cell problem

For a given unit cell, the stress of the DEM assemblies depends on the fine-scale material parameters, microstructural attributes, such as particle size distribution and spatial heterogeneity, and the loading path and time-history that leads to the current configuration [84, 85]. If the wavelength of the traveling signal is significantly larger than the particle dimensions, the quasi-static stress homogenized from the forces and branch vectors of the quasi-static configuration of unit cell can be used to update stress measures of the macroscopic dynamics problem without introducing significant errors.

Various criteria have been proposed to detect the quasi-static state of DEM dynamic relaxation problem [84, 86, 87]. In this work, we use the unbalanced force index I_{uf} introduced by Ng [84],

$$I_{uf} = \sqrt{\frac{\left(\frac{1}{n_p}\sum_{1}^{n_p} \text{unbalanced forces}\right)^2}{\left(\frac{1}{n_c}\sum_{1}^{n_c} \text{contact forces}\right)^2}} \tag{2.57}$$

where n_p and n_c denote the number of particles and number of contacts, respectively. The size of the pseudo-time or load step are calibrated such that the unbalanced force index I_{uf} is always kept smaller than a threshold value, .e.g. 0.01. This treatment ensures that the artificial damping introduced for dynamics relaxation does not significantly affect the simulated friction angle and shear strength. Mass scaling is also used to enable the usage of larger pseudo-time step and to reduce computational cost. In each pseudo-time step, the incremental displacement is prescribed to the particles at the boundary of the unit cell such that the unit cell deforms with the strain increment prescribed by the macroscopic problem. One particular interesting finding from Andrade and Tu [45] is that the granular assemblies with more particles typically require a small strain increment and more loading steps to maintain static equilibrium. Notice that if an identical quasi-static boundary value problem is simulated by both DEM and DEM-FEM models, the pure DEM model will require much more increment loading steps than the DEM-FEM counterpart [45]. In this sense, the DEM-FEM model can be considered as a divide-and-conquer tactic tool to coarsen load increments and increase efficiency of numerical simulations for large scale quasi-static granular mechanics problems.

2.2.4 Numerical algorithms for the nonlocal multiscale discrete-continuum model

The two-scale problem, consisting of the discrete unit cell problem subjected to periodic boundary conditions and the coarse-scale equations of motion, is two-way coupled. In this section, we focus on algorithmic details. The two-scale problem described by Equations (2.44) and (2.45) is solved sequentially as follows:

(i) Solve the dynamics relaxation problem at coarse scale using a corotational finite element model and compute the coarse-scale strain increment of each local quadrature.

(ii) Obtain the nonlocal coarse-scale strain increment using the staggered nonlocal operator and evaluate the nonlocal corotational strain increment.

(iii) Prescribing periodic boundary conditions to the unit cells on the nonlocal corotational coarse-scale strain increment of the corresponding nonlocal quadrature.

(iv) Obtain new static equilibrium states of the granular assemblies compatible to the prescribed boundary condition via DEM and compute the corotational coarse-scale Cauchy stress by Equation (2.44)b.

(v) Transform the corotational coarse-scale Cauchy stress to the fixed global frame and compute residual vector. Go back to (i) for next step.

To account for the geometric nonlinear effect, we employ a corotational formulation [88] where a local corotational coordinate frame, denoted by $\Re$, is attached to each finite element quadrature point and rotated with the deforming material. To preserve the characteristic length scale and eliminate pathological mesh dependence, we use a staggered nonlocal operator that explicitly introduces an intrinsic length scale and thus limits the shear band thickness when strain localization occurs. The interaction radius, denoted by *R*, is assumed to be an intrinsic material property.

In step (i), the coarse-scale incremental strain $\Delta\boldsymbol{\varepsilon}^{c}_{n+1/2}\ \mathbf{x},t$ is obtained from the solution of the coarse-scale problem at each quadrature point, in each time step. Due to strong size dependence that has been observed in granular materials we define a nonlocal coarse-scale strain increment [73, 74] $\left\langle \Delta\boldsymbol{\varepsilon}^{c}_{n+1/2}(\mathbf{x}_I) \right\rangle_R$ as follows

$$\begin{aligned}\left\langle \Delta\boldsymbol{\varepsilon}^{c}_{n+1/2}(\mathbf{x}_I)\right\rangle_R &= \sum_{\boldsymbol{\xi}_J\in Q_I} \alpha^{*}(\mathbf{x}_I,\boldsymbol{\xi}_J)\phi^{*}(\boldsymbol{\xi}_J)\\ \phi^{*}(\boldsymbol{\xi}_J) &= \begin{cases}\Delta\boldsymbol{\varepsilon}^{c}_{n+1/2}(\boldsymbol{\xi}_I) & \text{if } \boldsymbol{\xi}_J = \mathbf{x}_I\\ \Delta\boldsymbol{\varepsilon}^{c}_{n+\alpha}(\boldsymbol{\xi}_J) & \text{if } \boldsymbol{\xi}_J \neq \mathbf{x}_I\end{cases}\end{aligned} \tag{2.58}$$

where $\Delta\boldsymbol{\varepsilon}^{c}_{n+\alpha}$ denotes the coarse-scale strain computed on the fly, i.e. α is $\pm\ 1/2$, which represents either previous or current time step. $\Delta\boldsymbol{\varepsilon}^{c}_{n+1/2}$ is the coarse-scale strain at the current time t_{n+1}; $\mathbf{x}_I$ denotes the position of the current quadrature point I; Q_I is a set of quadrature points $\boldsymbol{\xi}_J \in Q_I$ adjacent to point $\mathbf{x}_I$ that satisfy

$$Q_I \,\big|\, \left|\mathbf{x}_I - \boldsymbol{\xi}_J\right| \le R, \forall\boldsymbol{\xi}_J \in Q_I \tag{2.59}$$

where R denotes the characteristic radius. $\alpha^{*}(\mathbf{x}_I,\boldsymbol{\xi}_J)$ is defined in Chapter 4.

Prior to exerting $\left\langle \Delta\boldsymbol{\varepsilon}^{c}_{n+1/2}(\mathbf{x}_I)\right\rangle_R$ onto the unit cell, it is rotated to the corotational frame, to yield the nonlocal corotational coarse-scale strain increment $\left\langle \Delta\boldsymbol{\varepsilon}^{\Re}_{n+1/2}(\mathbf{x}_I)\right\rangle_R$:

$$\left\langle \Delta\boldsymbol{\varepsilon}^{\Re}_{n+1/2}(\mathbf{x}_I)\right\rangle_R = \Re^{c}_{n+1/2}(\mathbf{x}_I)^{T} \cdot \left\langle \Delta\boldsymbol{\varepsilon}^{c}_{n+1/2}(\mathbf{x}_I)\right\rangle_R \cdot \Re^{c}_{n+1/2}(\mathbf{x}_I) \tag{2.60}$$

where $\Re^{c}_{n+1/2}(\mathbf{x}_I)$ denotes the coarse-scale rotation obtained from the polar decomposition of the coarse-scale deformation gradient $\mathbf{F}^{c}_{n+1/2}(\mathbf{x}_I)$ at a quadrature point $\mathbf{x}_I$ defined as

$$\mathbf{F}^{c}_{n+1/2}(\mathbf{x}_I) = \frac{\partial \mathbf{x}_{n+1/2}}{\partial \mathbf{X}} \tag{2.61}$$

and $\mathbf{x}_{n+1/2}$ is the coordinate at the midstep. Instead of directly prescribing the local strain increment as periodic boundary conditions applied on the boundaries of unit cells, the proposed model employs the coarse-scale strain increment $\left\langle \Delta\boldsymbol{\varepsilon}^{\Re}_{n+1/2}(\mathbf{x}_I) \right\rangle_R$ obtained from the macroscopic solver to obtain the corotational coarse-scale Cauchy stress $\boldsymbol{\sigma}^{\Re}_{n+1} \ \mathbf{x},t$ through Equation (2.44)b using DEM, which is then rotated back to the global Cartesian coordinate system.

$$\boldsymbol{\sigma}^{c}_{n+1} = \ \Re^{c}_{n+1} \ \cdot \boldsymbol{\sigma}^{\Re}_{n+1} \cdot \ \Re^{c}_{n+1} \ {}^{T} \tag{2.62}$$

The resulting coarse scale stress $\boldsymbol{\sigma}^{c}_{n+1} \ \mathbf{x},t$ is passed back to coarse-scale finite element engine to continue the iterative process. The aforementioned nonlocal discrete-continuum model is implemented by integrating FOOF [89], a macroscale FE solver, and OVAL [90], a microscale DEM solver. The numerical algorithm that links between the macro- and micro- scale solvers is shown in the flow chart in Figure 2.3. At each nonlocal quadrature point in the FE mesh, the FE solver executes the DEM unit cell problem in the corotational frame subjected to the nonlocal coarse-scale incremental strain $\left\langle \Delta\boldsymbol{\varepsilon}^{\Re}_{n+1/2}(\mathbf{x}_I) \right\rangle_R$. The fine-scale DEM solver evolves the discrete unit cell using explicit time integration to compute the coarse-scale Cauchy stress required to advance the coarse-scale problem. The particle arrangement, i.e. particle positions, velocities, and contact information, at the end of the coarse-scale time step are stored, to allow the new DEM simulation to begin from the final state of the previous time step. Each integration point has its own “restart” out-of-core file. The numerical implementation of the corotational formulations is illustrated in Box 2.1.

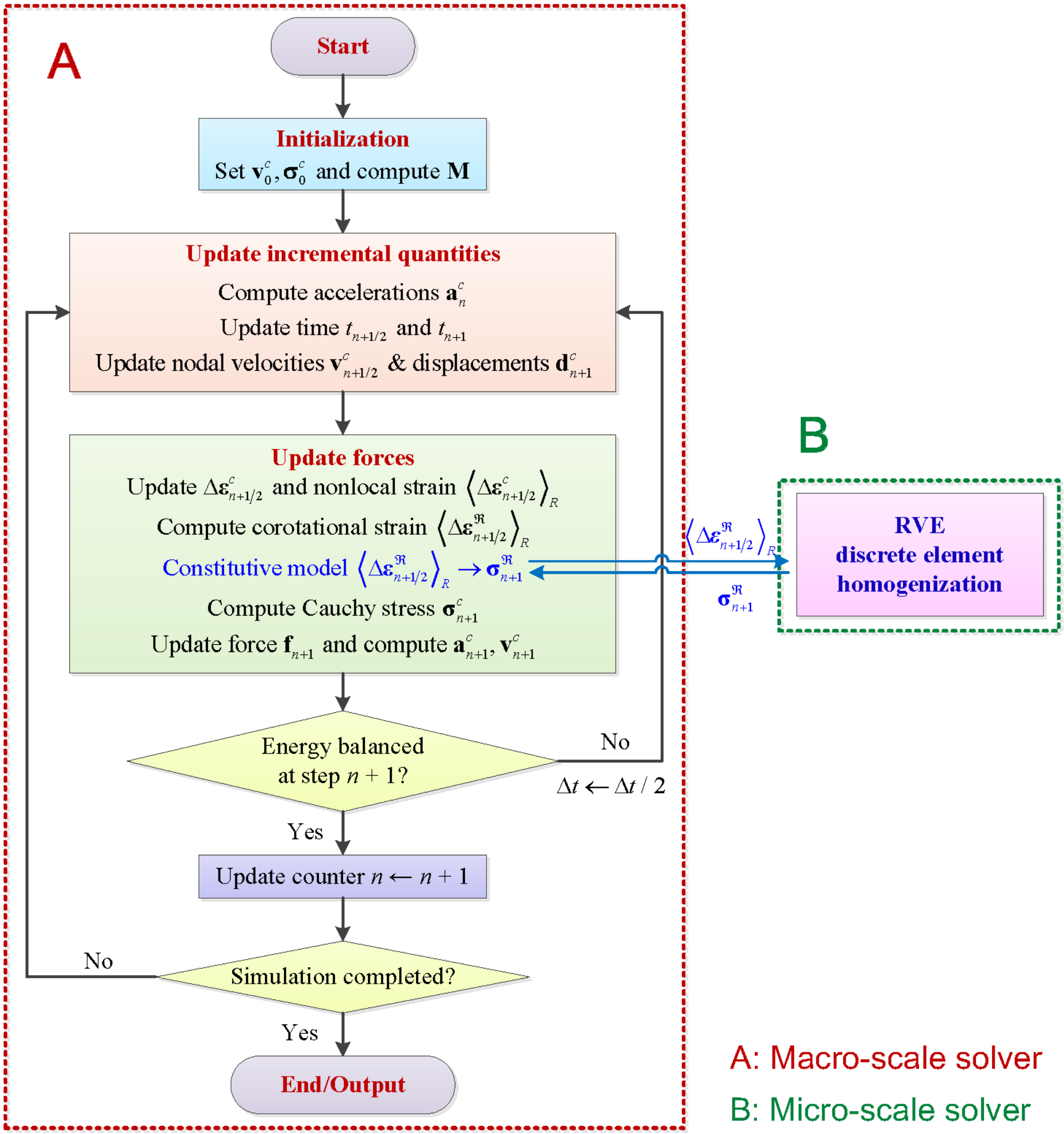

Figure 2.3 The overall framework integrating FE and DEM solvers for solving the two-scale problem

Box 2.1 The numerical implementation of the co-rotational DEM-FEM scheme for large deformation problems

Stress updating procedure for coarse-scale corotational framework

Step 1. Compute the coarse-scale deformation gradients at step $n+1/2$ and $n+1$

$$\mathbf{F}^c_{n+1} = \frac{\partial\left(\mathbf{X}+\mathbf{u}^c_{n+1}\right)}{\partial \mathbf{X}};$$
$$\mathbf{F}^c_{n+1/2} = \frac{\partial\left(\mathbf{X}+\mathbf{u}^c_{n+1/2}\right)}{\partial \mathbf{X}}$$

Step 2. Compute polar decompositions at step $n+1/2$ and $n+1$

$$\mathbf{F}^c_{n+1} = \Re^c_{n+1}\cdot\mathbf{U}^c_{n+1}$$
$$\mathbf{F}^c_{n+1/2} = \Re^c_{n+1/2}\cdot\mathbf{U}^c_{n+1/2}$$

Step 3. Compute the coarse-scale strain increment over the step from the **B** matrix for the coarse-scale finite element

$$\Delta\tilde{\boldsymbol{\varepsilon}}^c_{n+1/2} = \mathbf{B}_{n+1/2}\left(\mathbf{u}^c_{n+1}-\mathbf{u}^c_{n}\right)$$

$\Delta\boldsymbol{\varepsilon}^c_{n+1/2} \leftarrow \Delta\tilde{\boldsymbol{\varepsilon}}^c_{n+1/2}$ (convert 6×1 vector to symmetric tensor)

Step 4. Apply the nonlocal operator $\left\langle\cdot\right\rangle_R$ on the coarse-scale strain increment $\Delta\boldsymbol{\varepsilon}^c_{n+1/2}$ yields the nonlocal strain increment $\left\langle\Delta\boldsymbol{\varepsilon}^c_{n+1/2}\right\rangle_R$, and then rotate the nonlocal strain increment to the corotational frame

$$\left\langle\Delta\boldsymbol{\varepsilon}^{\Re}_{n+1/2}\right\rangle_R = \left(\Re^c_{n+1/2}\right)^T\cdot\left\langle\Delta\boldsymbol{\varepsilon}^c_{n+1/2}\right\rangle_R\cdot\left(\Re^c_{n+1/2}\right)$$

Invoke the DEM to solve for the coarse-scale corotational Cauchy stress at $n+1$

$$\boldsymbol{\sigma}^{\Re}_{n+1} \leftarrow \text{DEM} \leftarrow \left\langle\Delta\boldsymbol{\varepsilon}^{\Re}_{n+1/2}\right\rangle_R$$

Step 5. The coarse-scale corotational Cauchy stress is rotated back to the global

2.2.4.1 Temporal Stability of the coupled explicit DEM-FEM problems

The objective of the unit cell dynamics relaxation problems is to obtain stress measures from the granular configurations in the static equilibrium. As a result, both the mass and damping coefficients used in the DEM is not related to the actual physical quantities, but are parameters manipulated by the users to obtain non-oscillatory overall responses. While the original physical meanings of the mass and damping are lost in dynamics relaxation problem, both the explicit dynamics and dynamics relaxation problem still share the same form of governing equations and can be integrated in time by the conditionally stable explicit scheme. The critical pseudo-time step of the DEM problem therefore takes the same form as a damped mass-spring system, i.e.,

$$\Delta t_n^f \leq \Delta t_{cr}^f = \frac{2}{\omega_{\max}^f}(\sqrt{1+\xi^{f2}} - \xi^f) \tag{2.63}$$

where Δt_{cr}^f denotes the critical time step of the macroscopic problem; ξ^f denotes the fraction of critical damping corresponding to the highest natural frequency of the granular system $\omega_{\max}^f$. Assuming that there is no rotational stiffness introduced in the DEM contact model, the natural frequencies of the translational and rotational vibration of each particle read (Oñate and Rojek [43]),

$$\omega_n^f = \sqrt{\frac{k_n^f}{m^f}} \;\; ; \;\; \omega_\theta = \sqrt{\frac{k_\theta^f}{I_{\text{sphere}}}} = \sqrt{\frac{5k_t^f}{2m^f}} \;\; ; \;\; k_\theta^f = k_t^f R^2 \;\; ; \;\; I_{\text{sphere}} = \frac{2}{5} m^f R^2 \tag{2.64}$$

where I_{sphere} is the rotational inertia of the spherical particles and m^f is the mass of the particle. The critical time step of the DEM simulation can be obtained via Equation (2.63) where the highest natural frequency is approximated by $\omega_{\max}^f \approx \max(\omega_n^f, \omega_\theta)$. In practice, the DEM dynamics relaxation problems are often conducted with a fixed time step, while mass of the particles are tuned to ensure the stability between two pseudo-time steps.

On the other hand, the stable time step for the coarse-scale system is governed by the highest frequency ($\omega^c_{\max}$) of the course-scale incremental finite element problem

$$\Delta t^c_n \leq \Delta t^c_{cr} = \frac{2}{\omega^c_{\max}}(\sqrt{1+\xi^{c2}} - \xi^c) \tag{2.65}$$

where Δt^c_{cr} denotes the critical time step of the macroscopic problem; ξ^c denotes the fraction of critical damping corresponding to the highest natural frequency of the macro-scale FEM model. The critical step defined in Equation (2.65) also applies to the case where mass scaling and damping are applied to the macroscopic problem to obtain static equilibrium solution. Nevertheless, the critical macroscopic time step of the dynamic relaxation DEM-FEM problem is larger than that of the explicit DEM-FEM dynamics problem, as the damping and mass scaling are likely to filter out high frequency responses. Note that the critical time step of the fine-scale DEM and coarse-scale FEM can be related by,

$$\Delta t^c_{cr} = \alpha \Delta t^f_{cr} \ ; \ \alpha = \psi \frac{\omega^f_{\max}}{\omega^c_{\max}} \ ; \ \psi = \frac{\sqrt{1+\xi^{c2}} - \xi^c}{\sqrt{1+\xi^{f2}} - \xi^f} \tag{2.66}$$

where α is the optimal time step ratio between the fine and coarse scale systems. Notice that since the highest value frequency of the fine system is typically the higher one, α is usually larger than one.

2.3 Numerical examples

In this section, four numerical examples are presented to demonstrate the accuracy, efficiency and versatility of the proposed multiscale method in predicting the mechanical behavior of granular materials. Examples shown in this section provide evidences that the multiscale DEM-FEM model is able to replicate the single-scale DEM benchmark results. Refinement study indicates that the thickness of shear bands predicted by the nonlocal multiscale model is not sensitive to the mesh sizes of the continuum model.

2.3.1 Unit cell

The initial configuration of the unit cell is given in Figure 2.4. The unit cell was compacted into a dense and isotropic assembly from an initially sparse random arrangement of particles, which contains 4096 spherical grains with diameters ranging from 0.43mm to 1.18mm. The porosity after compaction was 0.338, with an initial average coordination number of 5.6 contacts per particle. The initial normal stresses in all directions were nearly equal to the mean stress of 416kPa. The initial response of the unit cell is assumed to be macroscopically homogeneous.

Periodic boundaries were employed on all sides of the unit cell in the numerical examples presented in this chapter. Such boundaries impose kinematic constrains on each boundary particle, allowing grains to pass from the parallelepiped unit cell domain to a fictitious adjacent one and simulate an infinitely periodic (repeated) system. Period boundaries are computationally advantageous over the rigid platens for providing a more uniform particle fabric throughout the assembly [46, 91]. Previous work done by [27, 92, 93] have found that homogenized responses inferred from periodic cell are less sensitive to boundary effects.

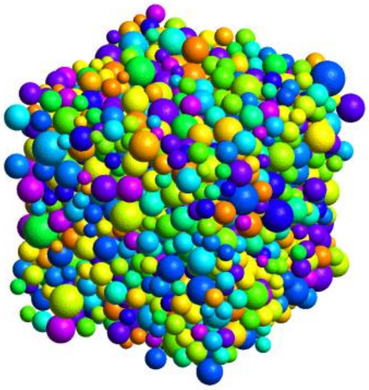

Figure 2.4 The initial configuration of the unit cell

The micro-model parameters given in Table 2.1 were used as input microscopic parameter in the following numerical examples, where shear modulus and Poisson ratio are the parameters for Hertz-Mindlin contact model. The mechanical properties of the material were obtained from pure DEM tests on the unit cell, e.g. the uniform compression test was used to get bulk modulus and the simple shear test to get the shear modulus [94]. The measured mechanical properties are shown in Table 2.2.

Table 2.1 Model parameters for DEM computation

29.0	Shear modulus G (GPa)
0.15	Poisson ratio
0.50	Coefficient of friction at particle contacts
0.00	Viscosity coefficient for translational body damping
0.00	Viscosity coefficient for rotational body damping
0.12	Viscosity coefficient for contact damping

Table 2.2 Material properties estimated from unit cell tests

Young's Modulus E (Mpa)	Poisson Ratio ν	Bulk Modulus K (Mpa)	Shear Modulus G (Mpa)
584	0.2	335	241

Accuracy and efficiency of the proposed multiscale technique rely crucially on the appropriate selection of the size of the unit cell so that it remains a representative volume element (RVE). In particular, the unit cell size must be small enough to ensure computational efficiency but large enough to remain representative. One common approach to estimate the size of the RVE is to vary the sizes of the unit cells and study the scale of fluctuation of the coarse-scale properties [34, 95-98]. Meier *et al* [99] and Guo and Zhao [50] applied this approach to discrete element models. Guo and Zhao [50] generated multiple granular assembles composed of different numbers of particles and studied the least amount of particles required to maintain the isotropy of the fabric tensor. They concluded that at least 400 particles required to constitute an RVE composed of particles of poorly graded grain size distribution. In the numerical examples presented in this chapter, the grain assembles used to calculate the Gauss point responses are composed of at least 4000 particles and has been examined in previous study to ensure the isotropy of the initial fabric tensor.

All simulations presented in this section are conducted with a three-dimensional eight-node hexahedral finite element integrated via the one-point Gaussian quadrature rule. The hour-glass control stabilization procedure in [100-102] is used to eliminate spurious zero-energy modes in the macroscopic finite element model. While the usage of one-point integration rule is a rather simple and well-known numerical treatment, the benefits for the DEM-FEM coupling scheme is significant. It improves both the speed and accuracy of the multiscale simulations by cutting 87.5% of the expensive 3D DEM unit cell simulations in [50, 53] that might cause volumetric locking problems otherwise.

2.3.2 One element verification tests

The multiscale model was first verified by comparing the global response of a single element (biaxial compression test and simple shear test) against the RVE response from pure DEM tests. This verification procedure is first introduced in [50] to test the accuracy and robustness of the developed information-passing DEM-FEM coupling scheme at material point level.

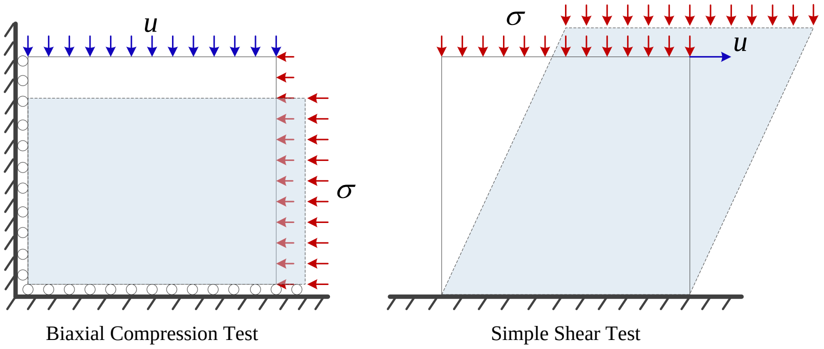

Figure 2.5 The boundary conditions for single element tests

The single element and its boundary conditions are depicted in Figure 2.5. In the simple shear test, the single element was subjected to a constant volume shear loading by keeping the confining pressure on the top to be constant. In the biaxial compression test, a vertical displacement was applied on the top surface and constant confining pressure was exerted on the surrounding surfaces. In both cases, the constant confining pressure was 416kPa, which was identical with the initial mean stress of the unit cell.

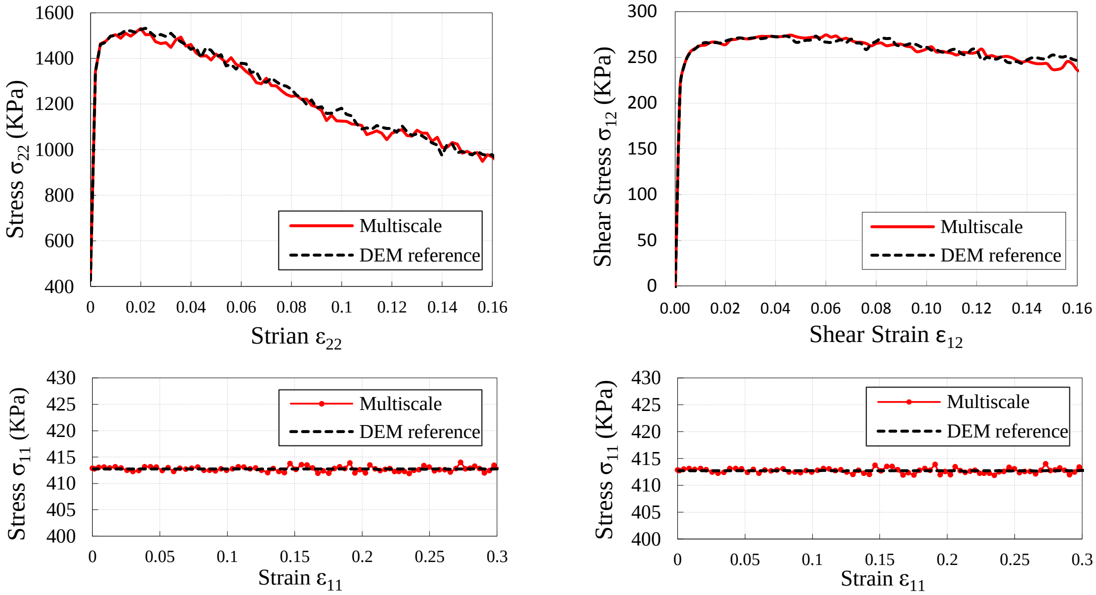

(a) Biaxial Compression (b) Simple Shear

Figure 2.6 The comparison of stress-strain curves between the multiscale simulation and DEM reference in the one element tests: (a) biaxial compression and (b) simple shear

The comparison of stress-strain curves are shown in Figure 2.6 for the one element tests using the multiscale DEM-FEM model and single-scale DEM. It can be observed that the multiscale approach gives almost identical prediction with those from the DEM simulations. This example verifies that the proposed multiscale discrete-continuum approach can replicate the elasto-plastic response of granular material accurately.

2.3.3 Wave propagation in dry granular rod

The modeling of wave propagation in granular media, such as wave attenuation and dispersion, is an active research area with implications for seismic soil-structure interaction, and foundation vibration [30, 31, 103-105]. Continuum-based analytical and computational modeling techniques have been widely used to investigate the seismic wave propagation [106, 107]. The path dependent responses of soil are often captured via macroscopic phenomenological models [30, 31, 63, 108]. While the cost of the continuum simulations is relatively low, the physical underspin of the phenomenological approach in the softening regimes is weak. On the other hand, dynamics discrete element simulations are also utilized by a number of researchers to study the micromechanics of wave propagation in granular matters [28, 109-111]. The upshot of the discrete element approach is the availability of microstructural information. However, the high computational cost of DEM has often limited the size of the simulations and thus making DEM not feasible to simulate field-scale site responses. The objective of this example is to demonstrate the potential of using the newly established DEM-FEM method to overcome the shortcomings of both continuum and discrete element approaches. To the best knowledge of the authors, this is the first time information-passing DEM-FEM scheme being used to simulate dynamics responses of granular layers.

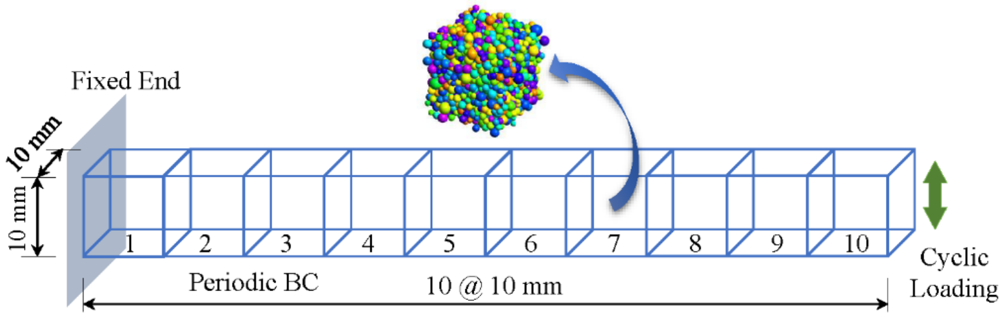

Figure 2.7 The boundary condition and macroscopic mesh of the sample for wave propagation in the granular rod

The one-dimensional domain has a dimension of 10mm×10mm×100mm, with its left hand side boundary totally fixed. Periodic boundaries were applied to the four surrounding surfaces of the rod to reduce boundary effect, as shown in Figure 2.7. At the macroscopic scale, the domain was discretized by 10 finite elements of equal sizes. The density of the model was $\rho = 1650\,\mathrm{kg/m^3}$. The right hand side of the rod was subjected to a vertically displacement-controlled sinusoidal cyclic load with frequency of $f = 10\,\mathrm{kHz}$ and maximum shearing displacement amplitude of $a = 0.1\,\mathrm{mm}$. The time duration of the whole simulation was $1\mathrm{ms}$ and the coarse-scale time increment was taken as $\Delta t = 1\mu\mathrm{s}$.

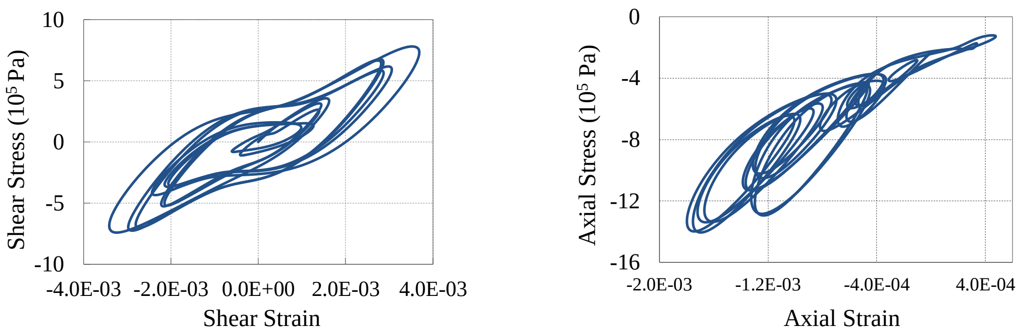

(a) Stress-strain curves

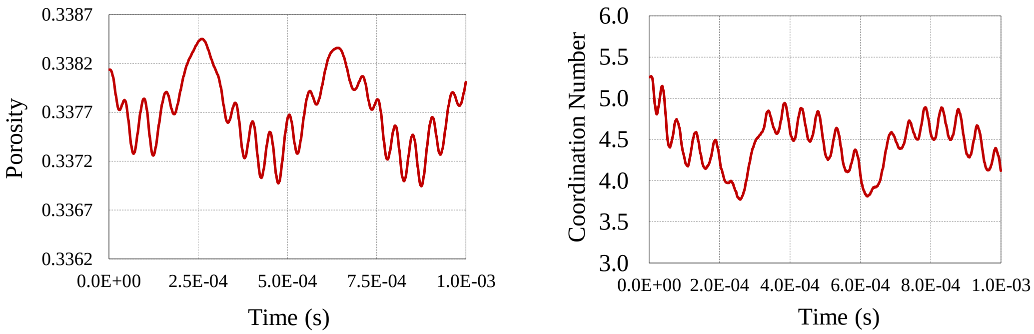

(b) Averaged microstructural properties versus time

Figure 2.8 Dynamic responses for element 9 at its Gauss point

The homogenized shear and compressive stress-strain responses of the quadrature point of element 9 are shown in Figure 2.8(a). We observe that the hysteresis and dissipative responses of non-cohesive frictional granular materials are successfully captured. Unlike previous macroscopic approaches where microstructural attributes are only taken into account indirectly via the evolution of internal variables, the multiscale approach is able to provide important microstructural measurements, such as coordination number and porosity of each unit cell as shown in Figure 2.8(b). This numerical experiment suggests that the proposed multiscale model is capable of modeling the dynamic responses of granular materials subjected to cyclic loadings within limited computational resources. This is a major departure from the previous DEM modeling efforts, in which particles are enlarged artificially for the sake of reducing the computational cost [112].

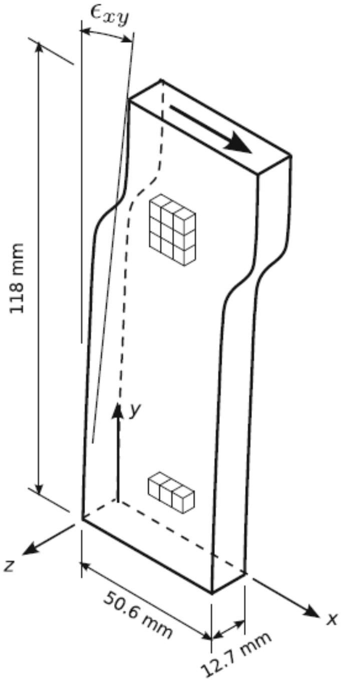

Figure 2.9 Geometric model and the boundary conditions for the simple shear test **[49]**

2.3.4 Shear band in a simple shear simulation on a dense grain assembly

In this example, the proposed model was further validated by a simple shear test on a dense grain assembly. Multiscale simulation results were compared with those from a single-scale DEM simulation conducted in [49]. The geometries and loading conditions are schematically shown in Figure 2.9. The model dimensions were 50.6mm × 118mm × 12.7mm. It was fixed at its bottom and sheared horizontally at its top boundary. Periodic boundary conditions were applied to the four surrounding surfaces to ensure a shear band develops along the full *x*-*x* width when passing across the periodic side boundaries. The domain of the numerical specimen was discretized into a uniform coarse mesh with $12 \times 5 \times 1$ elements. The grain assemblies assigned to all quadrature points are initially identical and thus the numerical specimen is macroscopically homogeneous. As a result, the shear band in a simple shear test may occur at any height, which makes the location of the band unpredictable. The previous DEM simulation results reported in [49] indicate that a shear band forms along a horizontal plane which is located at about three-quarters of the assembly height from its fixed boundary, a result likely to be caused by subtle imperfection within the grain assembly. To match the location of shear band in the DEM and DEM-FEM simulations, we artificially imposed an imperfection inside the shear band to break the symmetry and homogeneity of the sample. The unit cell with imperfection was created by randomly taking out 25 particles from the original unit cell. It should be noted that the initial state of the unit cell, e.g. mean stress, porosity and coordination number, needs to be identical with those of the grain assembly in the single scale DEM test. To maintain a quasi-static loading condition, the mass scaling technique was used in the coarse-scale finite element method for the entire model throughout the simulation.

Figure 2.10 through Figure 2.13 show the macroscopic mechanical behavior of the shear band during shear loading with constant vertical stress $p_0 = 416\,\mathrm{kPa}$. In the multiscale simulation results, the overall shear strain was computed from the horizontal displacement u_1 measured at the top surface divided by the initial height $h = 118\,\mathrm{mm}$ while the shear stress was obtained from the reaction force at the fixed end in the direction of shearing divided by the area of the bottom surface. Good agreements are observed in these figures between the results predicted by both the multiscale model and the DEM. For example, Figure 2.10 shows the shear stress-strain response of the grain assembly. Both shear stress and mean stress (see Figure 2.10 and Figure 2.11) reach their peak value and remaining nearly level until $\varepsilon_{12} = 6\%$, followed by an abrupt softening between the strains $\varepsilon_{12} = 6\%$ to $\varepsilon_{12} = 8\%$. Then at $\varepsilon_{12} = 8\%$ to 20%, shear and mean stress fluctuate at the critical state where porosity remains constant. Plastic dilatancy is observed in Figure 2.12 where the porosity of the assembly increases monotonically even as the compressive mean stress increases. As shear loading proceeds, porosity converges to a constant level after the shear stress reaches to its residual condition. This increase of volume is ascribed to the re-arrangement of particles in dense spherical packings and dense sands as they rise up over neighboring particles [49, 113]. Figure 2.13 shows the average coordination number of the entire assembly. By comparing the multiscale and pure DEM simulations, we can see that the multiscale model is able to replicate the evolution of coordination number, which decreases rapidly in early, pre-peak stress stage and eases down to a nearly constant in a gently sloping stretch throughout the subsequent peak, softening and residual periods.

The deformed configurations and averaged porosity along the assembly height at axial strain $\varepsilon_{12} = 12\%$ obtained from multi- and single- scale simulations are compared in Figure 2.14(a). The porosity curve obtained from the multiscale simulation is composed of 12 discrete points, each of which is an average of the porosities of a row of macroscopic element. Both the multiscale and DEM simulations indicate that the shear band is about 13-16mm, a quantity of great importance and will be used as a measure of the characteristic length in the size effect studies in the next example. The L_2 norms of the Euler angles of each particle in the unit cells inside and outside the shear band are plotted in Figure 2.14(b) to analyze the evolutions of microstructural attributes inside the deformation band. Consistent to the finding in the single-scale benchmark, the multiscale model predicts that particles inside the shear band rotate more than those outside the band. No grain-scale deformation band was found inside the unit cells of the multiscale model.

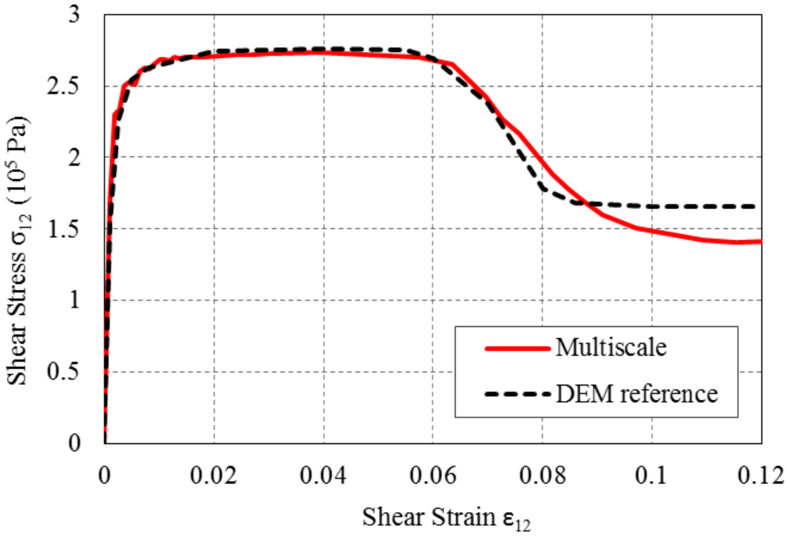

Figure 2.10 Shear stress-strain response during simple shear loading

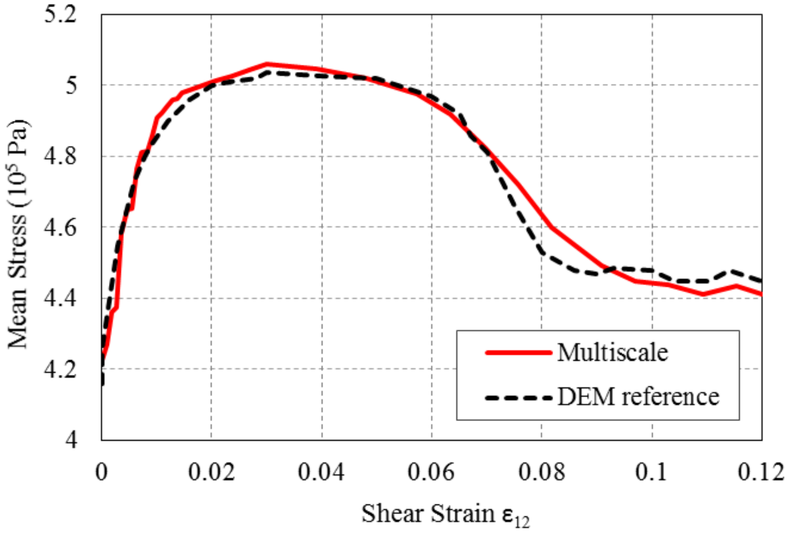

Figure 2.11 Mean stress versus shear strain during simple shear loading

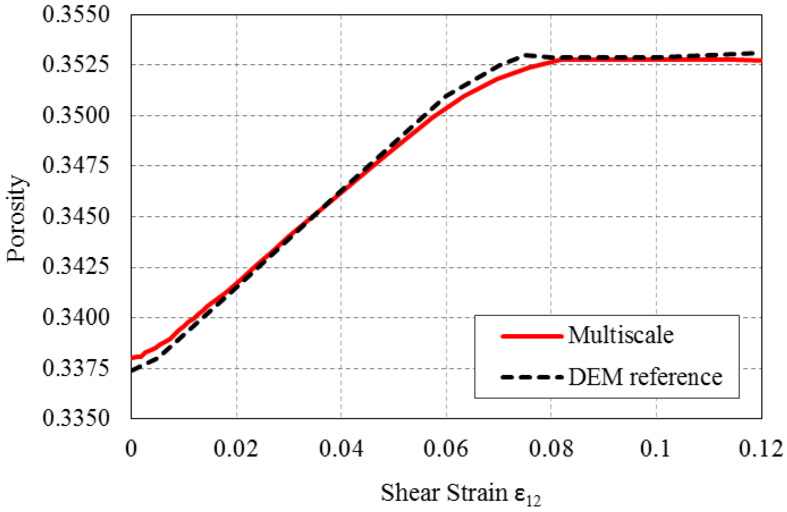

Figure 2.12 Porosity versus shear strain during simple shear loading

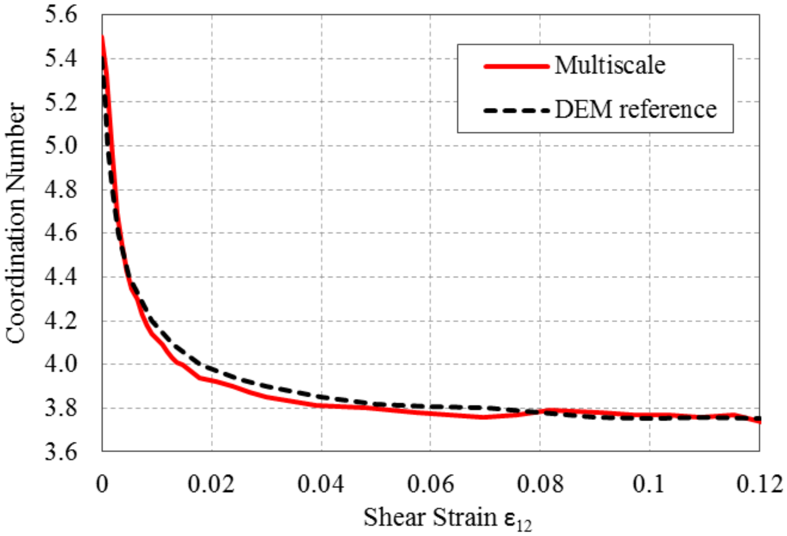

Figure 2.13 Coordination number versus shear strain during simple shear loading

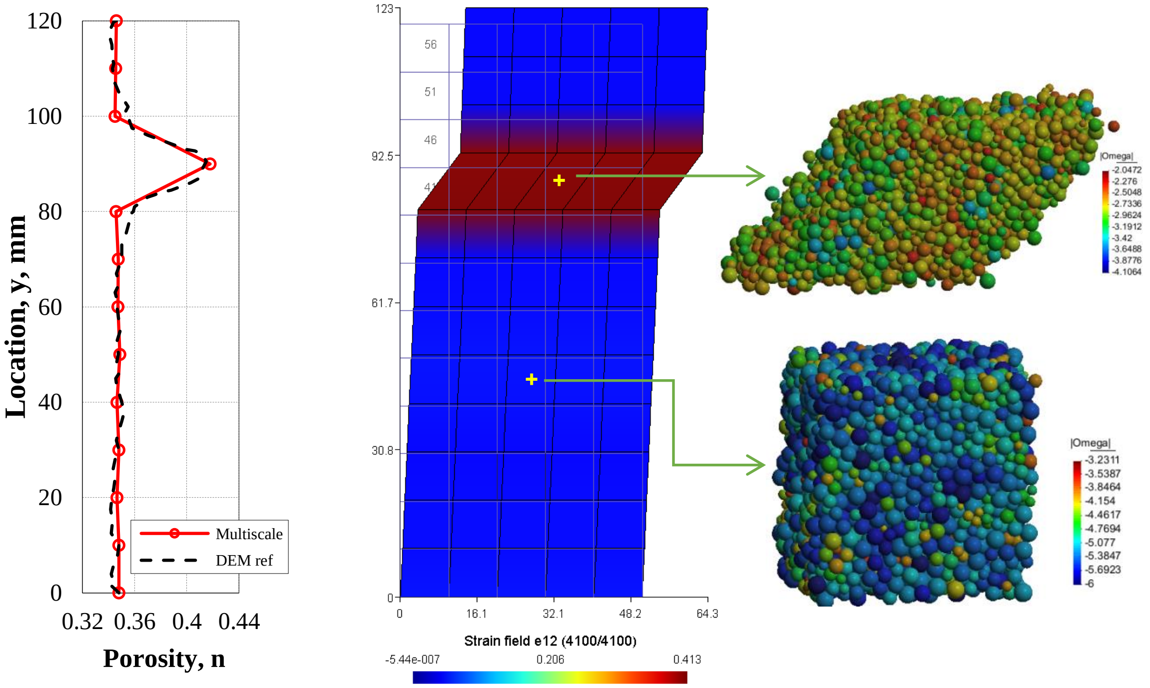

(a) Porosity along height (b) Microstructural attributes inside and outside the shear band

Figure 2.14 Profiles of (a) porosity and (b) overall deformed shape of the assembly as well as particles rotations of unit cells inside and outside the shear band at strain

Given the same computational resource, the CPU time for the multiscale simulation for the simple shear test with the current coarse mesh is 22 hours, which is much shorter than the CPU time used to complete the pure DEM counterpart (about one month). Therefore, it is evident that the proposed multiscale approach can reduce the computational cost significantly while making accurate prediction of the mechanical behaviors for granular materials. This enormous saving in simulation time is attributed to (1) the efficient bridging of the different spatial scales, (2) the introduction of multiple time-step scheme, which allows the coarse-scale problem to evolve at a much larger time step without causing stability issues, and (3) the usage of the reduced integration elements with hourglass control, which both reduces solution times substantially and eliminates shear locking while maintaining spatial stability.

2.3.5 Shear band in a plane strain biaxial compression test

Strain localization is of great importance to engineering applications, as it is often a precursor to progressive failure in granular materials. If no length scale is introduced, the onset of strain localization in numerical simulations may cause the loss of ellipticity (for static cases) or hyperbolicity (for dynamic cases) of the boundary value problem. This undesired ill-posedness may lead to pathological mesh dependence. To circumvent this issue in continuum models, various localization limiters have been introduced, including: (i) nonlocal or gradient models of which the constitutive response is governed by a gradient or integral of at least one internal variable(s) or strain measure [114-116], (ii) a rate-dependent constitutive law [82], and (iii) formulations that permit displacement discontinuities [117-121].

Pathological mesh size dependency has also been observed in the previous multiscale DEM-FEM coupling simulations [50, 53]. This pathological mesh size dependency is due to the ill-posedness of the macroscopic finite element model [82]. The proposed multiscale approach remedies this situation via a modified staggered *nonlocal* approach. To test whether this staggered nonlocal operator successfully introduces an intrinsic length scale and limits the shear band thickness when strain localization occurs, two sets of biaxial compression tests were carried out using the local and nonlocal multiscale model, respectively. The geometry, boundary conditions and the macroscopic meshes of the model are shown in Figure 2.15(a). The dimensions of the specimen were $40\mathrm{mm} \times 105\mathrm{mm} \times 5\mathrm{mm}$. A displacement controlled vertical load was monotonically applied on the top surface of the model. The confining pressure applied on vertical boundaries remained constantly throughout the loading. The asymmetric boundary condition was used at the bottom surface, in order to break symmetry and to initiate the localization. Three finite element meshes depicted in Figure 2.15(b) were considered. For the nonlocal multiscale model, the characteristic length was chosen to be $2R = 13.5\mathrm{mm}$, which is the same with the unit cell size, and is also consistent with the shear band width observed in the previous example.

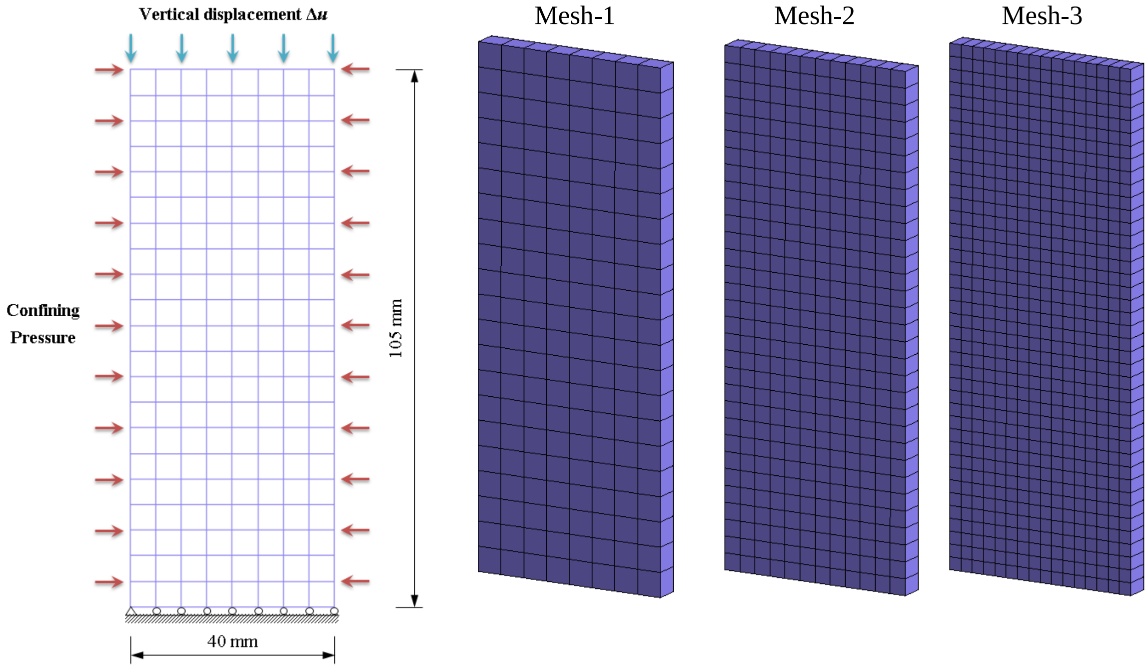

(a) Model geometry and boundary conditions

(a) Three meshes with 28×8×1, 31×12×1 and 41×16×1 elements, respectively

Figure 2.15 (a) The model dimensions and boundary conditions and (b) three meshes considered in the biaxial compression tests

The global stress-strain responses for different meshes predicted by local and nonlocal multiscale models are shown in Figure 2.16 and Figure 2.17, respectively. As can be seen in both figures, all three cases of meshes yield an identical, relatively elastic, pre-peak stress-strain behavior and alike peak stresses. The slight kink shown in the elastic regime is due to the wave reflection from the bottom boundary of the model, which may be removed by modifying the mass scaling factor. As loading proceeded, strain localization emerged and finally developed into a shear band. Even with the potential regularizations provided by the rate-dependence of the contact laws, the constitutive responses obtained from local multiscale model still exhibits mesh dependence in the post-bifurcation region, as shown in Figure 2.16 and Figure 2.17. On the other hand, Figure 2.18 shows the post-bifurcation stress-strain responses obtained from the nonlocal multiscale model. We observed that the softening responses in three cases are closer. The three curves converges to an identical stress level although the early stage softening slopes show moderate discrepancy.

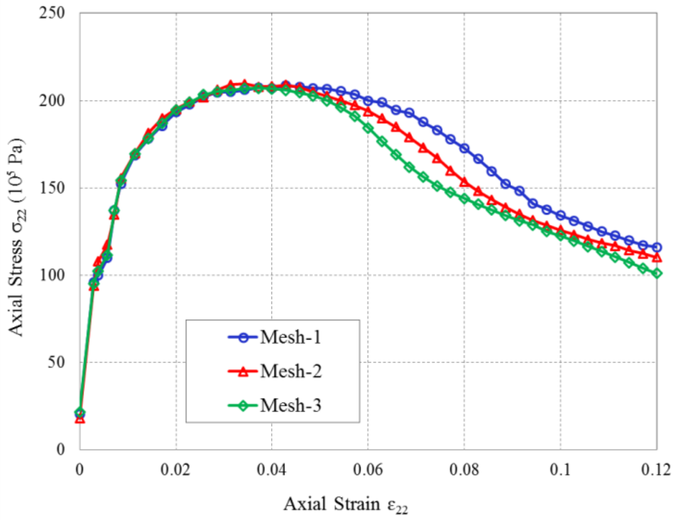

Figure 2.16 Compressive stress versus strain curves for different meshes using local multiscale model

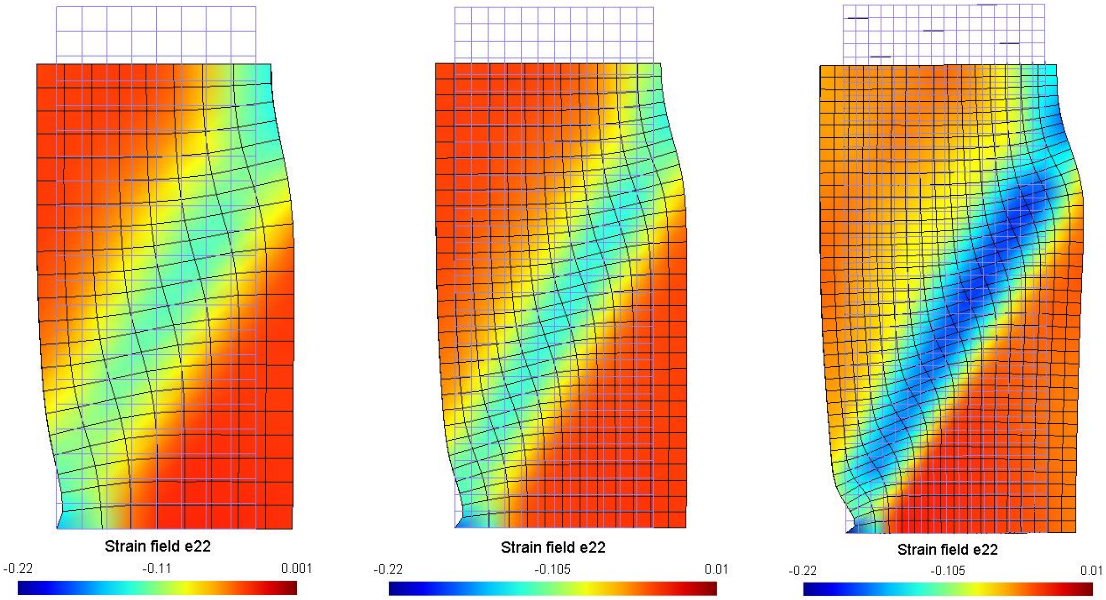

Figure 2.17 Contour plots of compressive strain for three meshes (local multiscale model)

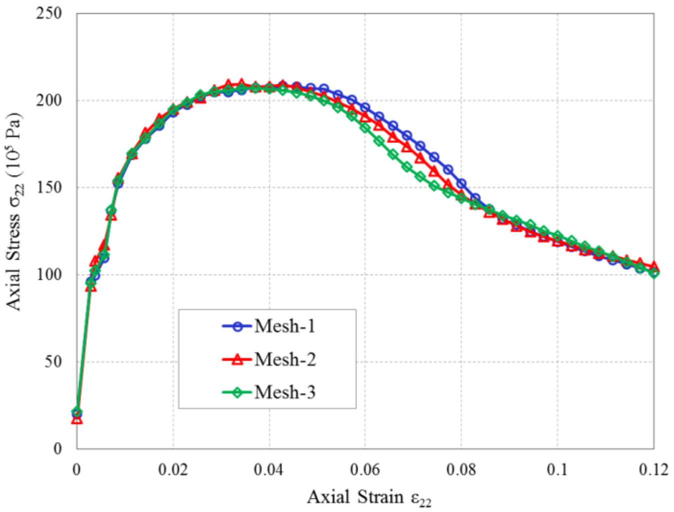

Figure 2.18 Compressive stress versus strain curves for different meshes using nonlocal multiscale model

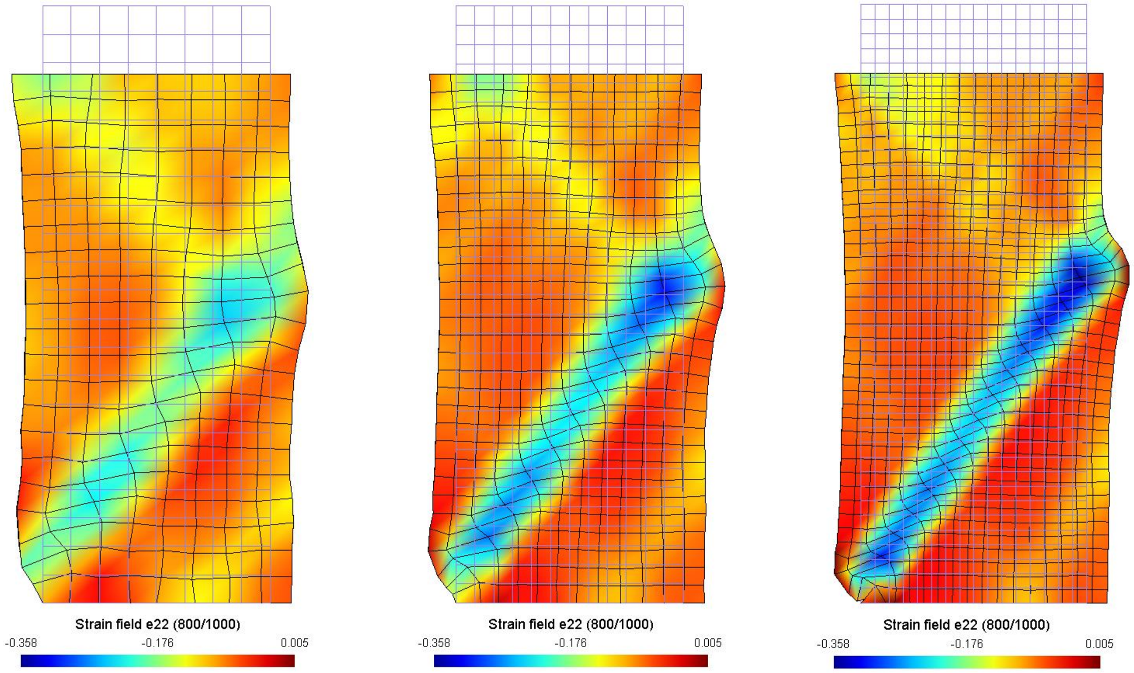

Figure 2.19 Contour plots of compressive strain for three meshes (nonlocal multiscale model)

The contour plots of vertical compressive strain for three meshes are shown in Figure 2.19. By comparing the stress-strain curves and the vertical strain distribution shown in Figure 2.16 to Figure 2.19, one may observe that the nonlocal multiscale scheme is able to deliver more consistent responses in the refinement study. Notice that the post-pack branch of the finest mesh of the stress-strain curve not always giving the softest response. This is attributed to the fact that there are not sufficiently material points in the coarse mesh to obtain an accurate integration for the nonlocal strain. As a result, the length scale of the coarse mesh is slightly larger than the fine mesh counterparts. In all numerical simulations, we found no shear band generated in the DEM assemblies. This absence of grain-scale shear band can be attributed by the particle shapes, the absence of rotational stiffness, lack of enrichment mode for the macroscopic finite element and the usage of periodic boundary condition as opposed to minimal kinematic boundary conditions. Detail examinations of these factors are out of the scope of the current study, but will be considered in the future.

The contour plots of vertical compressive strain for three meshes are shown in Figure 2.19. Similar localization behaviors and band widths are observed in simulation results for different meshes predicted by the proposed nonlocal multiscale model. It can be seen that the shear band width shows little dependency on mesh size.

2.4 Conclusions

In this chapter, we present a nonlocal multiscale discrete-continuum model for granular media. The proposed multiscale model effectively bridges two spatial scales, the coarse (continuum) scale and the fine (discrete) scale, by an information-passing coupling scheme based on the Generalized Mathematical Homogenization (GMH) theory. Each nonlocal quadrature point in the coarse-scale mesh is associated with a unit cell consisting of a granular assembly. The nonlocal strain obtained from the FEM solvers is converted into periodic boundary conditions for the grain-scale simulations occurred in the unit cells, which in return provide the nonlocal constitutive update at the macroscopic level via upscaling. This proposed model is verified via four benchmark problems. Good agreement has been observed by comparing the numerical solutions obtained via the multiscale DEM-FEM model with the single-scale DEM benchmark. The numerical examples demonstrate that the proposed multiscale discrete-continuum model is capable of reproducing both the dynamic and quasi-static behaviors of granular materials and simulation results obtained for bifurcation problems are practically mesh size independent. The multiple spatial scales and multi-step framework also presents a significant cost reduction compared to the direct DEM simulations.

Chapter 3

Determining Material Parameters for Critical State Plasticity Models Based On Multilevel Extended Digital Database

In this chapter, a new staggered multilevel material identification procedure is proposed for phenomenological critical state plasticity models. The key idea is to create a secondary virtual experimental database from high-fidelity models, such as discrete element simulations, then merge both the actual experimental data and secondary database as an extended digital database to determine material parameters for the phenomenological macroscopic critical state plasticity model. This chapter is reproduced from the paper co-authored with Waiching Sun and Jacob Fish, which was accepted for publication in the Journal of Applied Mechanics [122].

3.1 Introduction

Due to the complexity of granular material behaviors, phenomenological constitutive models must strike a balance between simplicity and predictability. While more comprehensive phenomenological models may be more robust and accurate for a given situation, the calibration of material parameters for such models are typically more complicated. Due to the larger set of internal variables required to describe the path dependent behavior more accurate, comprehensive constitutive models often require a sizable datasets composed of multiple stress paths, loading and drainage conditions in order to generate sufficient constraints for calibrations. Nevertheless, the demand to generate, measure, store, and track the sufficient data through numerical experiment can be costly and time consuming and therefore make the comprehensive models less appealing or even deemed to be impractical. The goal of this research is to accelerate the use of comprehensive constitutive models by means of an extended material database.

Over the past four decades, numerous constitutive models have been developed to describe the characteristic behavior of granular materials. The framework of elastoplastic modeling is well suited to simulate the path-dependent responses of granular materials, i.e., plastic strain, shear-dilatancy effects, stress-path dependency, pressure sensitivity, rotation of principal stress axes, fabric anisotropy, liquefaction and cyclic mobility, localization and shear banding [8, 10-13, 108, 123-129]. The critical state concept in combination with the elastoplasticity theory has been rather successful for constructing simple and pertinent constitutive models for sand and other cohesionless granular materials [14, 130-132]. Recently, these critical state models have been modified to incorporate stress anisotropy due to the evolution of fabric, and the anisotropic kinematic hardening responses for cyclic loading [16, 17, 65, 133, 134]. The improved accuracy, nevertheless, comes with the price of increased material parameter set. Consequently, it becomes no longer feasible to identify material parameters by visual inspection. Instead, one must constitute a constrained optimization problem designed to identify material parameters that minimizes the errors of numerical simulations characterized by an objective function and a set of constraints through an iterative process [135]. The discrepancy between experimental data and numerical simulations in a least square sense comprises the objective function, which depends on constitutive law parameters. A optimization algorithm, such as the gradient-based methods [136, 137], swarm intelligence-based algorithms [138, 139], and neural networks [140], is employed to seek material parameters that minimize the error defined by the objective function. There have been a number of attempts to calibrate constitutive model parameters for sands (e.g. Toyoura sand [15, 141], Nevada sand [137, 142, 143] and pea-gravels [144]). Various material identification schemes [145, 146] adopted finite element based inverse analysis to account for spatial heterogeneity. By utilizing a spatially dependent objective function, these algorithms exploit information from measured inhomogeneous deformation fields in comparison to the finite element solution to identify material parameters. This approach [147] has been recently employed to identify material parameters for granular materials by utilizing full-field displacement measurements. Spatially varying constitutive model parameters can be then obtained from such a calibration process.

The identification of material parameters for phenomenological constitutive laws relies heavily on experimental data obtained from laboratory tests or field studies. Since the cost and time involved to conduct physical tests required for calibration of material parameters is quite prohibitive, a widespread adoption of comprehensive models in practice is quite limited. For instance, to identify the shape and size of a yield surface, one may need to record the yield stress for multiple stress paths with different confining pressures. Such an extensive experimental data is rarely justifiable in practice due to considerable cost involved. A more cost-efficient alternative is to conduct only a limited numbers of tests and replace the rest of tests with virtual high-fidelity simulations. For instance, a small-scale physics-based high-fidelity model can be used to generate the required computational (virtual) data, which is then merged with an available limited experimental data to form so-called an Extended Digital Database (EDD). Experiments (both laboratory and virtual) housed in the EDD are then used to explore the new features of the comprehensive phenomenological constitutive material models and to identify their parameters. Such a framework is one of the key components of the Integrated Computational Material Engineering (ICME) [148], with a wide variety of engineering applications ranging from informatics-based material design to comprehensive data mining tools [149, 150] and wing design optimization in aerodynamics [151, 152].

In the present chapter, we propose a staggered multilevel approach for parameter identification of the phenomenological critical state plasticity models based on the EDD. By this approach, a secondary virtual experimental data is created from the high-fidelity models, such as the discrete element simulations (DEM), and then merged with the experimental database. The calibration procedure therefore consists of two steps: (i) calibration of the material parameters of the DEM to limited experimental database using optimization algorithms, and (ii) formation of EDD by expanding experimental database with the multi-axial loading simulations of the calibrated DEM.

The critical state two-surface plasticity model pioneered by Dafalias and Manzari [15], which incorporates the fabric-dilatancy effect, is used for proof of concept as a lower-fidelity model in comparison to the DEM. The DEM simulations of monotonic and cyclic torsion, directional shear, and various triaxial loads are used to expand the experimental database. The present chapter focusses on the Nevada sand for which experimental data is available.

The rest of the chapter is organized as follows. The proposed identification framework and the salient features of the EDD-based material identification procedure are introduced in Section 3.2, followed by the formulations of the variable-fidelity models, including the DEM and Dafalias-Manzari critical state plasticity model. Calibration of the DEM assemblies and the digital database formation are detailed in Section 3.3. The robustness and the effectiveness of the multilevel material identification process are studied via numerical experiments that calibrate the Dafalias-Manzari critical state plasticity model, hereafter referred as DaMa, to the EDD in Section 3.4 and Section 3.5. Finally, conclusions are drawn in Section 3.6.

3.2 The variable fidelity model framework

3.2.1 Description of the proposed algorithm

The proposed multilevel calibration approach synthesizes both micro-scale and macro-scale analyses. In the micro-scale analysis, a calibration of the geometric and micro-mechanical parameters of the DEM assembly based on the experimental data is carried out. The calibrated DEM simulations are subsequently used to expand the experimental database with new simulated loading histories, creating an extended database that combines the virtual and physical experimental data. This combined dataset is used to calibrate phenomenlogical constitutive model by solving the inverse problem with digital and experimental database that comprise the EDD as constraints. To test whether the calibrated phenomenological model is predictive, experimental data is split into two sets:

1) the training set, which is used for inverse calibration, and (2) the verification set that compares experimential data not included in the first set with the simulated response to assess the accuracy and robustness of forward predictions. The EDD provides the necessary dataset for calibration of multi-parameter phenomenological model, such as DaMa. Figure 3.1 illustrates the basic idea of the proposed multilevel material identification procedure using EDD and optimization.

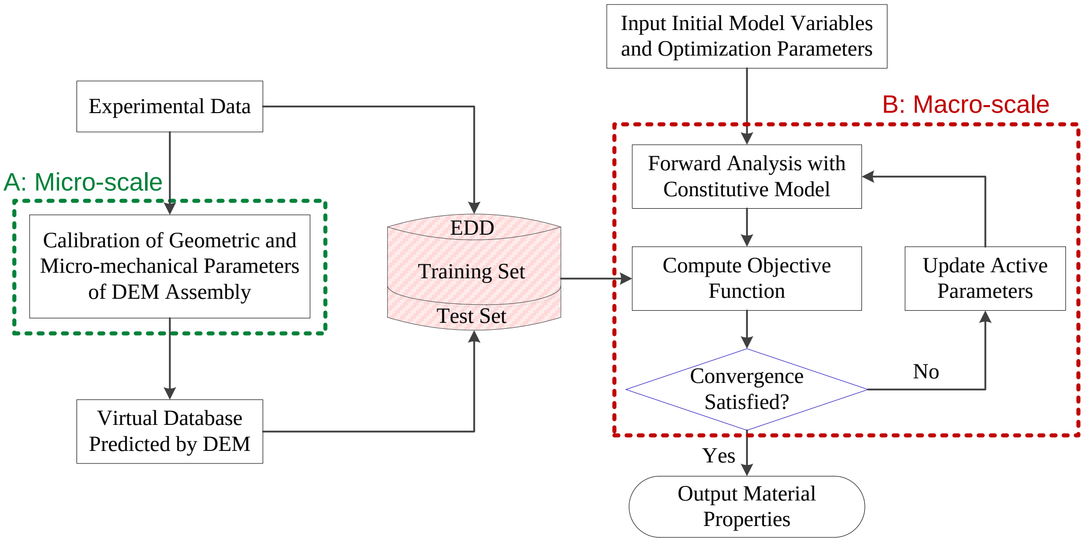

Figure 3.1 The flowchart of the proposed multilevel material identification procedure using EDD and optimization

3.2.2 Physics-based high-fidelity model: DEM

In the proposed calibration framework, we use DEM as the high-fidelity model to expand the experimental data. First proposed by Cundall and Strack [25], the discrete (distinct) element method (DEM) have been widely used to investigate micromechanical features of the granular assemblies. In a DEM assembly, the translational and rotational motions of each particle are obtained by the force and momentum equilibrium equations

$$\begin{aligned} m^J \ddot{\mathbf{u}}^J &= \sum \mathbf{f}^{IJ} + \mathbf{D}^{IJ} - C_g \dot{\mathbf{u}}^J \\ I^J \ddot{\boldsymbol{\theta}}^J &= \sum \mathbf{M}^{IJ} - C_g^* \dot{\boldsymbol{\theta}}^J \end{aligned} \tag{3.1}$$

where m^J and I^J are mass and moment of inertia of particle J, respectively; $\ddot{\mathbf{u}}^J$ and $\ddot{\boldsymbol{\theta}}^J$ are translational and rotational accelerations, $\mathbf{f}^{IJ}$ and $\mathbf{M}^{IJ}$ are inter-particle force and moment respectively exerted on particle J from particle I at contact, $\mathbf{D}^{IJ}$ is contact damping force comprising of normal, $\mathbf{D}_n^{IJ}$, and tangential, $\mathbf{D}_s^{IJ}$, components at the contacts, defined as

$$\mathbf{D}_n^{IJ} = c_n\dot{\mathbf{n}}; \quad \mathbf{D}_t^{IJ} = c_s\dot{\mathbf{s}} \tag{3.2}$$

where $\dot{\mathbf{n}}$ and $\dot{\mathbf{s}}$ are normal and tangential components of the relative velocities between particles I and J; here, c_n and c_s are the corresponding contact damping coefficients. C_g and C_g^* are the coefficients of global damping operating on particle velocities $\dot{\mathbf{u}}^J$ and $\dot{\boldsymbol{\theta}}^J$, respectively [25]. The contact and global damping in the DEM simulations are chosen to adequately damp the higher frequency modes without excessively delay particle motions [49].

The DEM simulation explicitly models the kinetics of individual grains via inter-particle contact laws. In our implementation, we adopt the Jäger contact model [153-155] with a general contact profile in which the sphere is assumed to have a specific local irregularity of the form $A_\alpha r^\alpha$ at the contact region, as shown in Figure 3.2(a).

In the Jäger contact model, the normal force between an asperity of a general form and a hard flat surface is defined as

$$f^n = C_\alpha \zeta^{(1+\alpha^{-1})}, \quad C_\alpha = \frac{4\alpha G_s}{(1-\nu_s)(1+\alpha)}\left(\frac{\Gamma\;\; 1+\alpha\;\big/2}{\sqrt{\pi}A_\alpha\Gamma\;\; 1+\alpha\big/2}\right) \tag{3.3}$$

where ζ denotes the indentation at contact (half of the contact overlap); G_s and ν_s are shear modulus and Poisson's ratio of the grains, respectively; and Γ is the gamma function; α is a variable that describes the local irregularity of contact. Equation (3.2) yields the standard Hertz solution if $\alpha = 2$ and $A_2 = 1\big/\;2R$, representing Hertzian contact along ideally smooth spherical surfaces (Figure 3.2(a)). With a conical asperity with $\alpha = 1$, A_1 corresponds to the outer slope of the cone (Figure 3.2(b)).

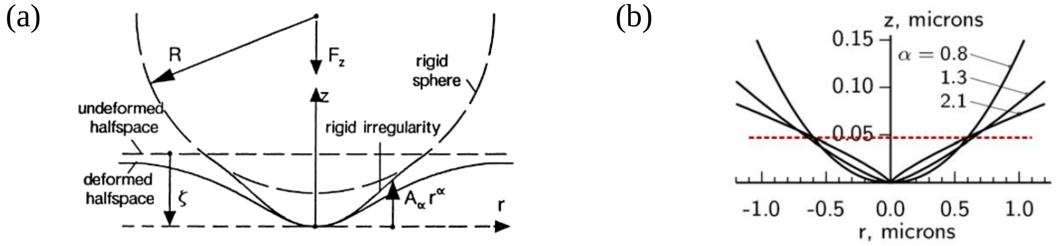

Figure 3.2 Contours of contact asperities (a) general power-form surface contour $z = A_\alpha r^\alpha$ [153]; (b) surface contour with different asperities used in DEM simulations. The figure is reproduced from [156].

The tangential force between two contacting particles is computed with an extension of the Hertz-Mindlin-Deresiewicz theory, which accounts for the three-dimensional arbitrary normal and tangential contact movements. The detailed theoretical argument and numerical implementation are presented in [154, 155]. The equations of motion in Equation (3.1) are solved via an explicit central difference algorithm. Within each incremental updates for the displacement and rotation of each particle, scaled time step and unit mass are used to obtain quasi-static responses via dynamic relaxation [57].

For a unit cell composed of a collection of particles, the macroscopic Cauchy stress tensor of the particle assemblies can be recovered via spatial homogenization [23], virtual work principle [157] or GMH (Generalized Mathematical Homogenization) [57], which all lead to,

$$\sigma_{ij} = \frac{1}{V}\sum_{n=1}^{N_c} l_i^n f_j^n \tag{3.4}$$

where f_j^n is the contact force at contact point n; l_i^n is the branch vector connecting the centers of two contacting particles at n, and N_c the total number of contacting particle pairs in the volume V of the unit cell.

To expand the material database using DEM, one must first calibrate the material parameter of the particle and generate granular assemblies using the physical experimental data. Following this calibration step, the DEM is employed to expand the material database for a specific type of granular materials, such as sand and slit.

3.2.3 Observation-based phenomenological model: Dafalias-Manzari critical state plasticity model

In this study, we adopt the model proposed by Dafalias and Manzari in [15] as the low-fidelity phenomenological model and calibrate it with the expanded database. Notice that the multilevel calibration framework proposed in this study is also applicable to other critical state plasticity models for granular materials (e.g. [158-161]). The Dafalias-Manzari model is selected, as the test bed, because it is relatively easy to implement and has been widely adopted. To enhance the accuracy and predictability of the phenomenological model, a larger set of material parameters is typically required to govern the evolutions of internal variables. For comprehensive phenomenological models for granular materials, such as the critical state plasticity model of Dafalias and Manzari [15] considered in this study, considerable experimental database is required to identify the loci of yield surface and the size and shape of the limited surfaces.

Dafalias and Manzari [15] model (DaMa) is a comprehensive critical state plasticity model employing state parameters for modeling mechanical behavior at various densities and confining pressures under monotonic and cyclic loading conditions. It combines the concepts of bounding surface model and critical state generalized plasticity concept to form an elegant model that accounts for fabric-dilatancy quantity and the effect of fabric changes to predict stress-strain relations under various drainage and loading conditions. For completeness, the multi-axial formulation of the DaMa model is briefly described in this section. Interested readers are referred to the original papers cited above.

In the DaMa model [15], the strain increments are decomposed into elastic and plastic parts. The elastic parameters G_0 and ν define the nonlinear hypo-elastic behavior:

$$G = G_0 p_{at} \frac{(2.97 - e)^2}{1 + e} \left(\frac{p}{p_{at}} \right)^{1/2} ; \quad K = \frac{2(1 + \nu)}{3(1 - 2\nu)} G \tag{3.5}$$

where G_0 is a material constant, ν is Poisson’s ratio, e is the current void ratio, and p_{at} is the atmospheric pressure. Both G_0 and ν are independent of applied stress path and can be obtained from small strain monotonic shearing behavior.

The yield surface is defined as

$$f \ \sigma, \alpha, m \ = \ r_{ij} r_{ij} \ ^{1/2} - \sqrt{2/3} m p = 0 \tag{3.6}$$

$$r_{ij} = \ s_{ij} - \alpha_{ij} \tag{3.7}$$

where m is the size of the yield surface, s_{ij} is the deviatoric stress tensor, and α_{ij} is the deviatoric back stress tensor which describes the kinematic hardening of the yield surface by indicating the location of the center of the yield surface.

The critical state of a soil [14] refers to a continuous flow state with constant stress and constant volume in granular soil. In this model, the critical state of a soil [162] is defined to satisfy simultaneously the conditions $q = q_c$, $p = p_c$, $e = e_c$, $q_c / p_c = M$ as well as the equation of critical state line (CSL) in $e - p$ space [163]

$$e_c = e_0^c - \lambda_c \left(\frac{p_c}{p_{at}} \right)^{\xi} \tag{3.8}$$

where q_c, p_c, M, e_0^c, λ_c and ξ are scalar parameters obtained from interpolating the mean stress $p = \ \sigma_1 + 2\sigma_3 \ / 3$, deviatoric stress $q = \sigma_1 - \sigma_3$ and the void ratio e at the critical state. Here, e_0^c denotes the void ratio at $p_c = 0$. The bounding surface is associated with the maximum peak stresses ratio state that can be attained, and the dilation surface represents the condition at which the contractive soil behavior changes to dilative. The bounding surface and the dilation surface are constructed to comply with the critical state theory in the following form which are dependent on the Lode angle θ:

$$\alpha_{\theta ij}^{a}=\sqrt{2/3}\,\alpha_{\theta}^{a}n_{ij}\ ;\quad n_{ij}=r_{ij}\Big/\sqrt{r_{ij}r_{ij}}\qquad a=b,c,\mathrm{d} \tag{3.9}$$

$$\alpha_{\theta}^{b}=g(\theta,c)\left[M\exp\left(-n^{b}\psi\right)-m\right] \tag{3.10}$$

$$\alpha_{\theta}^{d}=g(\theta,c)\left[M\exp\left(n^{d}\psi\right)-m\right] \tag{3.11}$$

$$\alpha_{\theta}^{c}=g(\theta,c)\left[M-m\right] \tag{3.12}$$

$$g(\theta,c)=\frac{2c}{(1+c)-(1-c)\cos 3\theta};\quad c=\frac{M_{e}}{M_{c}} \tag{3.13}$$

where the superscript a may take three values of b (for bounding surface), d (for dilatancy surface) and c (for critical surface); n^{b} and n^{d} are positive scalar constants which control the size of the two limit surfaces, respectively; $g(\theta,c)$ is the scaling function used for generalization of surfaces from triaxial space to multiaxial space; and c is referring to the ratio between the critical state stress ratios in compression and extension. For simplicity, c is a common parameter for all three surfaces. It is seen from Equations (3.9) to (3.11) that the bounding and dilation surfaces tend to coincide with the critical state surface as $\psi\rightarrow 0$. The yield surface governed by pure kinematic hardening law translates in the stress space. The state parameter $\psi=e-e_{c}$ proposed by Been and Jefferies [164] is used to measure the distance from the current state to the critical state.

The evolution of hardening modulus K_{p} and plastic dilatancy D are described as functions of the relative distance between the image back stress ratios, $\alpha_{\theta ij}^{b}$ and $\alpha_{\theta ij}^{d}$ respectively, and the back stress of the yield surface α_{ij}, given by,

$$K_{p}=\frac{2}{3}ph\left(\alpha_{\theta ij}^{b}-\alpha_{ij}\right)n_{ji} \tag{3.14}$$

$$D=A_{d}\left(\alpha_{\theta ij}^{d}-\alpha_{ij}\right)n_{ji} \tag{3.15}$$

where h is a positive scaling function defined by positive constants h_{0} and c_{h}

$$h = b_0 \Big/ \Big[\ \alpha^b_{\theta ij} - \alpha^{in}_{ij} \ \ n_{ji} \Big] \quad \text{with} \quad b_0 = G_0 h_0 \ \ 1 - c_h e \ \ \ p \big/ p_{at} \ \ ^{-1/2} \tag{3.16}$$

And the positive scaling function A_d for dilatancy is affected by the fabric changes such that

$$A_d = A_0 \ \ 1 + \left\langle z_{ij} n_{ji} \right\rangle \quad \text{with} \quad \dot{z}_{ij} = -c_z \left\langle -\dot{\varepsilon}^p_v \right\rangle \ z_{\max} n_{ij} + z_{ij} \tag{3.17}$$

where z_{ij} denotes the fabric-dilatancy internal variable, A_0 and $z_{\max}$ are material constants which control the pace of evolution of z_{ij} . The Macaulay brackets $\left\langle \bullet \right\rangle$ representing $\left\langle x \right\rangle = x$ if $x > 0$ and $\left\langle x \right\rangle = 0$ if $x \leq 0$. Equations (3.14) to (3.17) dictate the mechanism of the effect of fabric change on dilatancy upon load increment reversals.

Therefore, a total set of 15 model parameters are required to completely define the DaMa model. These parameters can be categorized into three groups, namely, elastic parameters, critical state parameters, and model specific parameters [144, 165, 166]. The parameters in each group are:

- Elastic parameters: G_0 and ν
- Critical state parameters: M , c , λ_c , e^c_0 and ξ
- Model specific parameters: yield surface parameter m , hardening constants h_0, c_h, n^b , dilatancy constants A_0, n^d , and fabric-dilatancy constants $z_{\max}, c_z$

3.2.4 Calibration through constrained optimization

The parameter identification process is formulated as a constrained optimization problem in which the objective is to identify an optimal set of parameters that minimizes the discrepancy between the simulated response by DaMa and the data housed in EDD in the least square sense. In other words, the optimization problem is an iterative process in which material parameters are modified in each trial based on the results of the inverse problem until the predicted data best fits the target data housed in EDD.

Let us denote the model parameters to be calibrated by $\boldsymbol{\theta} \in \Re^{N\times 1}$, where N is the total number of parameters. In the present study, $\boldsymbol{\theta}$ consists of fifteen DaMa model parameters ($N = 15$), i.e., $\boldsymbol{\theta} = \left[G_0, \nu, M, c, \lambda_c, e_0^c, \xi, m, h_0, c_h, n^b, A_0, n^d, z_{\max}, c_z\right]^T$.

We define an objective function representing the discrepancy between the target response quantities from EDD and the predicted data obtained by DaMa model as

$$f(\boldsymbol{\theta}) = \frac{1}{2}\mathbf{r}^T(\boldsymbol{\theta})\,\mathbf{W}\mathbf{r}(\boldsymbol{\theta}) \tag{3.18}$$

where $\mathbf{r}(\boldsymbol{\theta}) \in \Re^{SL\times 1}$ is the residual vector and $\mathbf{W} \in \Re^{SL\times SL}$ is the diagonal weight matrix, given by

$$\mathbf{r}(\boldsymbol{\theta}) = \begin{Bmatrix} \hat{\mathbf{y}}_1(\boldsymbol{\theta}) - \mathbf{y}_1 \\ \hat{\mathbf{y}}_2(\boldsymbol{\theta}) - \mathbf{y}_2 \\ \vdots \\ \hat{\mathbf{y}}_S(\boldsymbol{\theta}) - \mathbf{y}_S \end{Bmatrix}; \quad \mathbf{W} = \begin{bmatrix} \dfrac{w_1}{\mathbf{y}_1^T\mathbf{y}_1}\mathbf{I} & & & \mathbf{0} \\ & \dfrac{w_2}{\mathbf{y}_2^T\mathbf{y}_2}\mathbf{I} & & \\ & & \ddots & \\ \mathbf{0} & & & \dfrac{w_S}{\mathbf{y}_S^T\mathbf{y}_S}\mathbf{I} \end{bmatrix} \tag{3.19}$$

in which $\mathbf{y}_i = \left[y_{i1}, y_{i2}, \ldots, y_{iL}\right]^T$ and $\hat{\mathbf{y}}_i(\boldsymbol{\theta}) = \left[\hat{y}_{i1}(\boldsymbol{\theta}), \hat{y}_{i2}(\boldsymbol{\theta}), \ldots, \hat{y}_{iL}(\boldsymbol{\theta})\right]^T$ are the target response quantities and the predicted data, respectively, of the *i*th data set ($i = 1, 2, \ldots, S$); w_i is the weight coefficient of the *i*th data set; $\mathbf{I} \in \Re^{L\times L}$ is an identity matrix; S is total number of target data sets; and L is total number of data points of the target response quantities.

For example, in our implementation, both the stress-strain behavior and the evolution of void ratio are considered in the curve fitting process for each test (e.g., $L = 2$). Thus, the target response quantities and the predicted data can be expressed as

$$\mathbf{y}_i = \left\{ \frac{q_i}{p_0}, e_i \right\}^T \quad \text{and} \quad \tilde{\mathbf{y}}_i(\boldsymbol{\theta}) = \left\{ \frac{\hat{q}_i(\boldsymbol{\theta})}{p_0}, \hat{e}_i(\boldsymbol{\theta}) \right\}^T \tag{3.20}$$

where q denotes the deviatoric stress, p_0 is the initial mean stress, and e is the void ratio.

The goal is to minimize the objective function $f(\boldsymbol{\theta})$ and to obtain the best set of model parameters. Therefore, the constrained optimization problem can be stated as:

$$\hat{\boldsymbol{\theta}} = \arg\min_{\boldsymbol{\theta}} f(\boldsymbol{\theta}) \qquad \theta_j^{lb} \leq \theta_j \leq \theta_j^{ub} \quad j = 1,2,\ldots,N \tag{3.21}$$

where θ_j^{lb} and θ_j^{ub} denote the lower and the upper bound of the *j*th parameter, and $\hat{\boldsymbol{\theta}}$ denotes the calibrated model parameters that best fit the target database.

We employ the Gauss-Newton Trust Region algorithm [167] to solve the optimization problem in Equation (3.21). In the optimization process, the parameters are updated by the iterative process given by

$$\widehat{\boldsymbol{\theta}}_{k+1} = \widehat{\boldsymbol{\theta}}_k - \left(\widehat{\mathbf{J}}_k^T \widehat{\mathbf{W}} \widehat{\mathbf{J}}_k + \lambda \mathbf{I}\right)^{-1} \widehat{\mathbf{J}}_k^T \widehat{\mathbf{W}} \widehat{\mathbf{r}}(\boldsymbol{\theta}_k) \tag{3.22}$$

where *k* is the iteration number index; $\widehat{\boldsymbol{\theta}}_k$ denotes the active parameter set (i.e., $\widehat{\boldsymbol{\theta}}_k \in \boldsymbol{\theta}_k$); λ is the Levenberg-Marquardt parameter [168] which can be determined iteratively; $\widehat{\mathbf{r}}$ and $\widehat{\mathbf{W}}$ contain components of $\mathbf{r}$ and $\mathbf{W}$, respectively, for model parameters inside the bounds; $\widehat{\mathbf{J}}_k$ is the Jacobian of $\widehat{\mathbf{r}}(\boldsymbol{\theta}_k)$, namely, $\widehat{J}_k^{pj} = \partial \widehat{r}_p(\boldsymbol{\theta}_k) \big/ \partial \theta_j$, where $p = 1,2,\ldots,SL$ and $j = 1,2,\ldots,N$. Herein, we approximate the Jacobian components using central difference method, *v.i.z.*,

$$\widehat{J}^{pj} \approx \frac{\widehat{r}_p(\theta_1,\ldots,\theta_{j-1},\theta_j + \delta\theta_j,\theta_{j+1},\ldots,\theta_N) - \widehat{r}_p(\theta_1,\ldots,\theta_{j-1},\theta_j - \delta\theta_j,\theta_{j+1},\ldots,\theta_N)}{2\delta\theta_j} \tag{3.23}$$

where $\delta\theta_j$ is an infinitesimal perturbation. It is noteworthy that Equation (3.23) is guided by an active parameter strategy, which imposes simple bounds on the trust region represented by radius Δ [167]. In addition, λ is selected to ensure that the solution updates lie within the trust region. The two parameters λ and Δ are computed using a locally constrained hood step algorithm [34].

The optimization is completed and a set of parameter $\hat{\boldsymbol{\theta}}$ is returned when the following criteria are satisfied:

$$C_1 = f\ \ \boldsymbol{\theta}_k\ \ \leq 0.01 \quad \text{and} \quad C_2 = \left\| \widehat{\mathbf{J}}_k^{1:SL,j} \right\| \leq 1 \times 10^{-8} \qquad j = 1, 2, \ldots, N \qquad (3.24)$$

where $\left\| \bullet \right\|$ denotes the L_2 norm of a vector and 1:*SL* denotes the first *SL* rows in a matrix.

3.3 Calibration and prediction of DEM model

In this study, we test the proposed multilevel calibration procedure with the Nevada sand dataset from published literature. We choose the Nevada sand as the test bed due to the large amount of existing data generated in the past decades. For this purpose, laboratory tests performed on this sand by Earth Technology Corporation in the course of the Verification of Liquefaction Analysis by Centrifuge Studies (VELACS) project [169] were used. The objective is to use well-calibrated DEM assemblies as virtual specimens and conduct high-fidelity micro-scale (DEM) simulations on those DEM assemblies to generate the necessary constraints to calibrate the DaMa model when experimental data alone is insufficient. The generalized procedure of the calibration process can be described as follows: (i) construct DEM assemblies with the goal of approximating the behavior of Nevada sand, (ii) calibrate the DEM model parameters based on the lab experimental data, (iii) carry out DEM simulations subjected to loading paths that are not considered in the lab tests, (iv) expand the database by adding the DEM simulated responses to the experimental database and form the EDD, and (v) calibrate the constitutive model parameters based on the EDD.

In this section, the DEM assemblies are created and calibrated to approximate the behavior of Nevada sand at different relative densities and confining pressures against the experimental data from lab test reports [169, 170]. The DEM simulations were conducted using the open source DEM code *OVAL* [90].

3.3.1 RVE generation

The macroscopic mechanical behavior of granular materials depends on both the material properties of particles and the topological features of the grain assemblies. The discrete element method provides a convenient tool to explicitly model this particulate nature but is also more computationally expensive than continuum model. As result, the DEM is chosen as the high-fidelity model to expand the material database. In this study, we assume that the material database contains only macroscopic constitutive responses obtained from conventional shear, plane strain and triaxial loading experiments. Microscopic data that require unconventional experimental techniques to obtain (e.g. position vectors of individual particles, topology of void space, and the scale of fluctuation of material parameters within specimen) are not considered [32, 33, 98, 171]. Such a consideration is reasonable for engineering practice in which microscopic data are rarely extracted or used due to the associated cost.

Since we do not employ any microscopic data that explicitly captures the geometry of individual grains, we will not attempt to use the corresponding DEM models, such as the level-set based potential element method [172] and NURBS-based Granular element Method [173], to generate granular assemblies that are compatible to the experimental counterpart on a grain-by-grain basis. Instead, our goal is to generate RVE that has the compatible initial relative density, grain size distribution, and constitutive responses to those of the experimental counterpart. In this study, we adopt the particle assemblies from Kuhn *et al.* [156], which are composed of bumpy particles formed by lumping overlapped spheres together. As shown in [174], those assemblies composed of bumpy particles may yield more realistic friction angles and macroscopic shear strength than those composed of spherical particles. Since the angularity and non-symmetry of particle shape can be properly replicated bumpy particles, this leads to improvement in capturing the interlocking among particles and the greater resistance of particle rotation. As a result, the increase in the deviatoric stress to the peak value and in the volumetric strain with the angularity commonly observed in experiments can be replicated with bumpy particles.

In this study, a bumpy, compound cluster shape with a large central sphere with six embedded satellite spheres in an octahedral arrangement was chosen, which was studied and presented by Kuhn *et al.* [156]. This shape has proven to be sufficiently non-round to produce a target range of initial densities and realistic strength. A total number of 6400 bumpy elements from an assembly that represents a unit cell at the material point, which are found to be large enough to capture the overall stress-strain response of material but sufficiently small to prevent mesoscale localization and BC-induced nonuniformities (e.g., shear bands, footings, excavations) [156].

The particles in the grain assembly are scaled such that the grain size distribution of the DEM assembly is close to those of the real Nevada sand. The resultant virtual specimen has a grain size distribution with median particle size $D_{50} = 0.165\,\mathrm{mm}$ and a coefficient of uniformity $C_u = 2.0$, comparing with the lad tests data $D_{50} = 0.165\,\mathrm{mm}$ and $C_u = 2.2$ [169] (see Table 3.1). A comparison of the physical properties between lab test samples for Nevada sand and the DEM assembly of virtual particles are shown in Table 3.1.

Table 3.1 Physical properties of Nevada sand and DEM assemblies used in this study

Sample	Mean grain size D_{50} mm	Uniformity coefficient $C_u = D_{60}/D_{10}$	Max void ratio $e_{\min}$	Min void ratio $e_{\max}$	Void ratio at different D_r		
					$e_{D_r=40\%}$	$e_{D_r=60\%}$	$e_{D_r=89\%}$
Nevada Sand [169]	0.165	2.2	0.511	0.887	0.736	0.661	0.552
DEM assembly	0.165	2.0	0.525	0.850	0.720	0.655	0.560

The 6400 bumpy particles were initially sparsely distributed in a space cell surrounded by period boundaries. By repeatedly assigning random velocities to particles and reducing the assembly height, fifteen assemblies with initial void ratios in the range of $0.850 - 0.525$ were created. Each assembly was then isotropically consolidated to a target mean effective stress from 10kPa to 400kPa for subsequent computations involving micro-parameter calibration and digital database enrichment. It is noted that tests under even higher consolidation stresses may lead to particle breakage and grain crushing [175-177] when the stress applied on the soil particle exceed its strength, which is beyond the scope of this study.

Due to the disparity in shapes between natural sand and DEM particles, the real and numerical specimens may have different ranges of attainable porosity. As a result, minimizing the discrepancy of the numerical and experimental void ratios may not lead to comparable state condition in granular materials. As a result, we conduct a numerical relative density test to obtain the maximum and minimum void ratio of the granular assemblies, and the notion of relative density was chosen as a measure of equivalence to match experimental and numerical results [174]

$$D_r = \frac{e_{\max} - e}{e_{\max} - e_{\min}} \tag{3.25}$$

where void ratio e can be obtained from relative density D_r through the maximum void ratio $e_{\max}$ and minimum void ratio $e_{\min}$ that a sand sample could achieve with standard ASTM procedures [178, 179]. The corresponding void ratios at three different relative densities used in the following simulations are shown in Table 3.1. To compare the results quantitatively, the simulations were accomplished on samples with identical or nearly identical relative densities compared with those in target experimental tests.

3.3.2 Calibration of the micromechanical properties of DEM assemblies

The micromechanical properties of the aforementioned DEM assemblies have been calibrated by Kuhn et al. [156] to capture cyclic liquefaction behavior of Nevada sand. The calibration efforts attempt to produce a relationship between small-strain bulk shear modulus $G_{\max}$ and the mean effective stress p' (i.e. $G_{\max} = p'^{\,0.5}$), and to achieve $G_{\max}$ with a target value of 90MPa at a mean effective stress of 80kPa [180, 181]. The same set of model parameters obtained by Kuhn et al. [156] were used throughout all the DEM simulations in this study, as shown in Table *3.2*. For detailed processes on particle assembly preparation and guidance on model parameter calibration, interested readers are referred to [156, 174, 182].

A series of undrain and drained triaxial compression and extension simulations were carried out on the samples studied above. The shear stress-strain (octahedral) responses recorded during the computations were compared to experimental data [169] in Figure 3.3 through Figure 3.10.

Table 3.2 Micromechanical parameters for DEM computations

29.0	Shear modulus G (GPa)
0.15	Poisson ratio
0.60	Coefficient of friction at particle-particle and particle-wall contacts
0.20	Viscosity coefficient for translational body damping
0.30	Viscosity coefficient for rotational body damping
0.00	Viscosity coefficient for contact damping
5.3	Jäger contact model parameter A_1
1.3	Jäger contact model parameter α

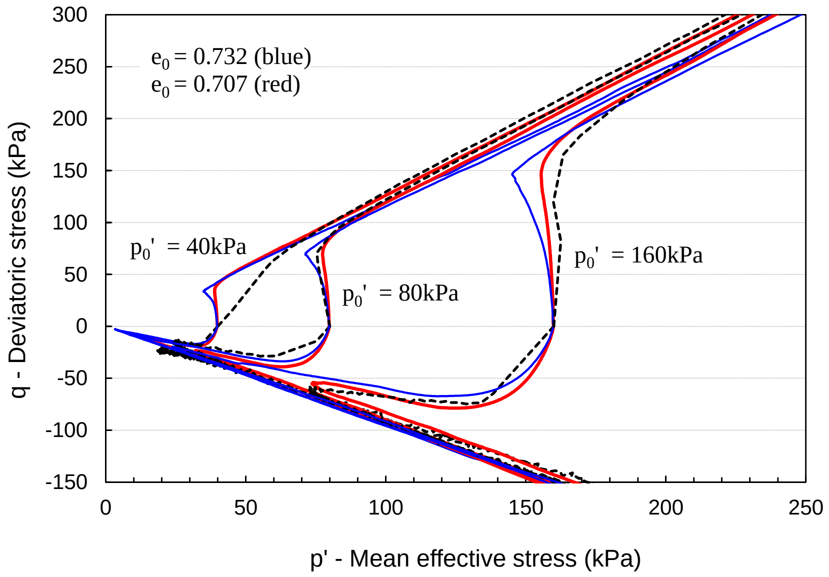

Figure 3.3 Undrained triaxial compression and extension of DEM simulations at three densities, comparing with Nevada sand tests at relative density of 40% with initial confining pressure of 40kPa, 80kPa and 160kPa (stress paths)

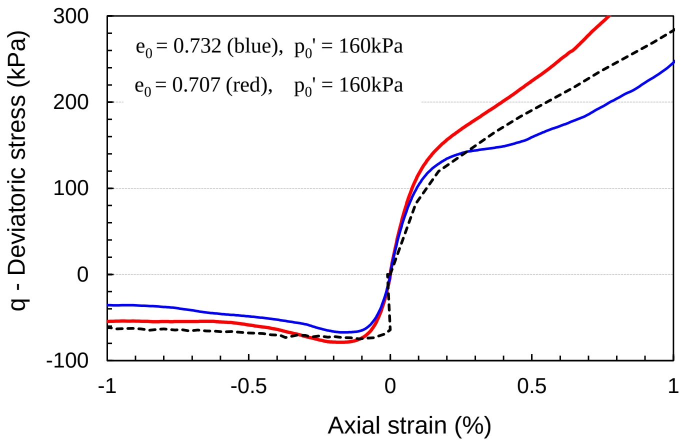

Figure 3.4 Undrained triaxial compression and extension of DEM simulations at three densities, comparing with Nevada sand tests at relative density of 40% with initial confining pressure of 160kPa (stress-strain curves)

To match the monotonic undrained triaxial compression and extension tests for Nevada sand at 40% D_r, two assemblies with initial void ratios (0.732 and 0.707) that straddle the target void ratio $e_0 = 0.720$ (see Table 3.1) were considered. Before triaxial loading, the assemblies were isotropically consolidated to the mean effective stress p_0' corresponding to the experiments' confining stresses, e.g. 40kPa, 80kPa and 160kPa, respectively. The mean effective stress p' was computed from initial confining pressure and pore-water pressure $p' = p - u$. Loading was applied in the z direction with a small strain increment $\Delta\varepsilon_{zz} = \pm 5.0 \times 10^{-7}$ to maintain nearly quasi-static conditions. For undrained tests, zero volume-change conditions were applied by constantly adapting assembly deformations in x and y directions so that $1+\varepsilon_{xx} \quad 1+\varepsilon_{yy} \quad 1+\varepsilon_{zz} = 1$. Figure 3.3 and Figure 3.4 show the undrained behavior for these two DEM assemblies in triaxial tests, respectively. The undrained stress paths of the two DEM assemblies shown in Figure 3.3 depict the constitutive responses of Nevada sand observed in the laboratory tests, i.e. the stress paths converge to substantially the same critical state lines (CSL) in both extension and compression tests at larger strains. During extension tests, strain softening behaviors are observed at small strains, followed by a pickup of strength at phase transformation (PT) points. It can be seen that a good match occurred in the triaxial compression tests at confining pressure $p' = 80\mathrm{kPa}$ and $p' = 160\mathrm{kPa}$. However, the small strain portion in $p' = 40\mathrm{kPa}$ compression tests differed from the experiment curve. Better overall agreement is achieved at assembly with $e_0 = 0.707$. The q -axial strain curves predicted by DEM simulations in Figure 3.4 exhibit the correct trend with the experiment data in small strain regime.

Figure 3.5 and Figure 3.6 show the DEM simulations along with the experimental results of drained monotonic compression constant- p' tests with initial relative density of about 40%. Reasonably well agreement in the $q - p'$ plots (Figure 3.5(a)) with experimental results was achieved for both densities $e_0 = 0.732$ and $e_0 = 0.707$ at various confining pressures. The volumetric curves in Figure 3.5(b) and Figure 3.6(b) show that the calibrated DEM model can predict the volumetric strain reasonably well in the small strain region, particularly within 4%. Nevertheless, the discrepancy in volumetric responses gradually grows beyond this strain level, and the over-prediction of volumetric strain in DEM becomes apparent, even though the deviatoric stress of the simulated and experimental simulations remain roughly compatible. This discrepancy in volumetric responses may be attributed to the discrepancy in particle shapes and arrangements, the over-simplification of contact laws, and the effect of boundary conditions. Presumably, incorporating microscopic experimental data via particle tracking techniques as well as more advanced DEM models to replicate the real particle shapes can reduce these discrepancies. These possible research directions will be explored in subsequent studies, but is out of the scope of this work.

The DEM predictions for 60% D_r triaxial tests under undrained and drained conditions are shown in Figure 3.7 through Figure 3.10. Two assemblies were considered for comparison with initial void ratios $e_0 = 0.674$ and $e_0 = 0.640$. Similar trends are observed in the 60% D_r drained and undrained tests.

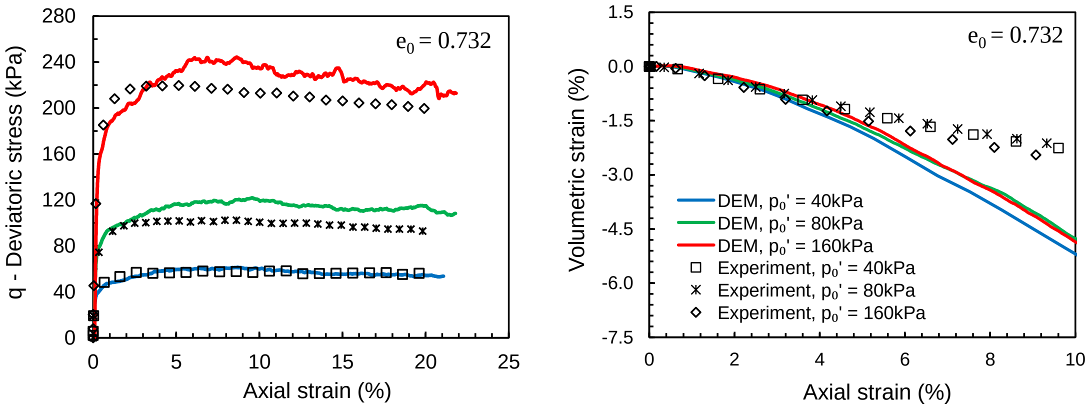

(a) (b)

Figure 3.5 Drained triaxial compression (constant p') of DEM simulations at $e = 0.732$, comparing with Nevada sand tests at relative density of 40% with initial confining pressure of 40kPa, 80kPa and 160kPa: (a) stress paths and (b)volumetric curves

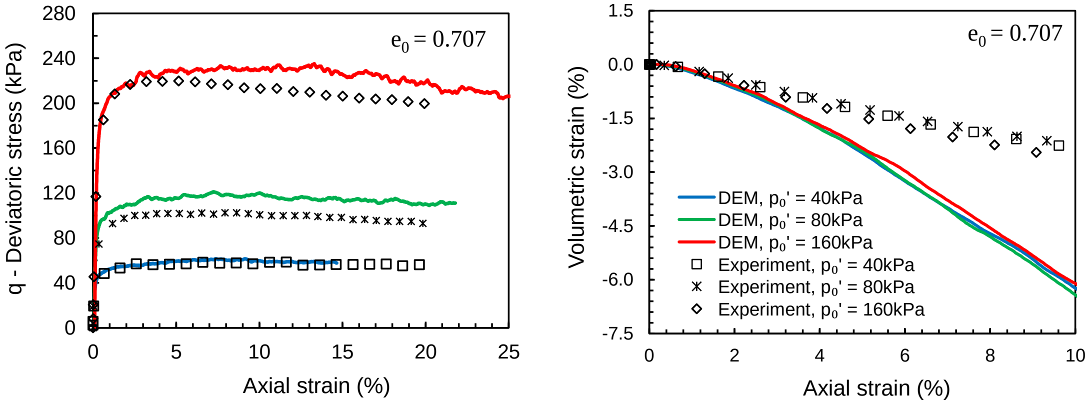

(a) (b)

Figure 3.6 Drained triaxial compression (constant p') of DEM simulations at $e = 0.707$, comparing with Nevada sand tests at relative density of 40% with initial confining pressure of 40kPa, 80kPa and 160kPa: (a) stress paths and (b)volumetric curves

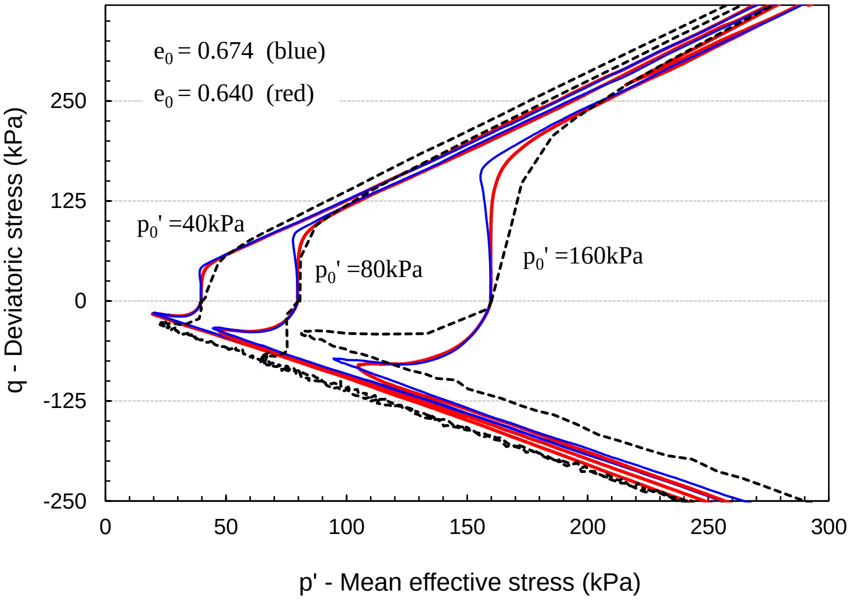

Figure 3.7 Undrained triaxial compression and extension of DEM simulations at three densities, comparing with Nevada sand tests at relative density of 60% with initial confining pressure of 40kPa, 80kPa and 160kPa (stress paths)

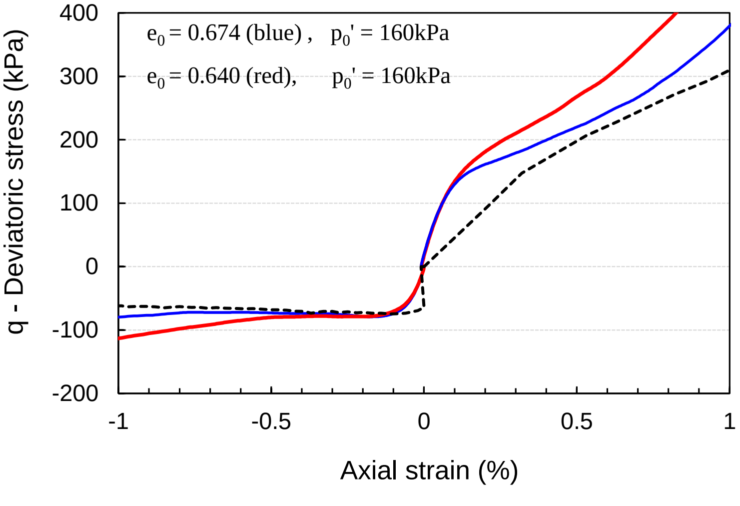

Figure 3.8 Undrained triaxial compression and extension of DEM simulations at three densities, comparing with Nevada sand tests at relative density of 60% with initial confining pressure of 160kPa (stress-strain curves)

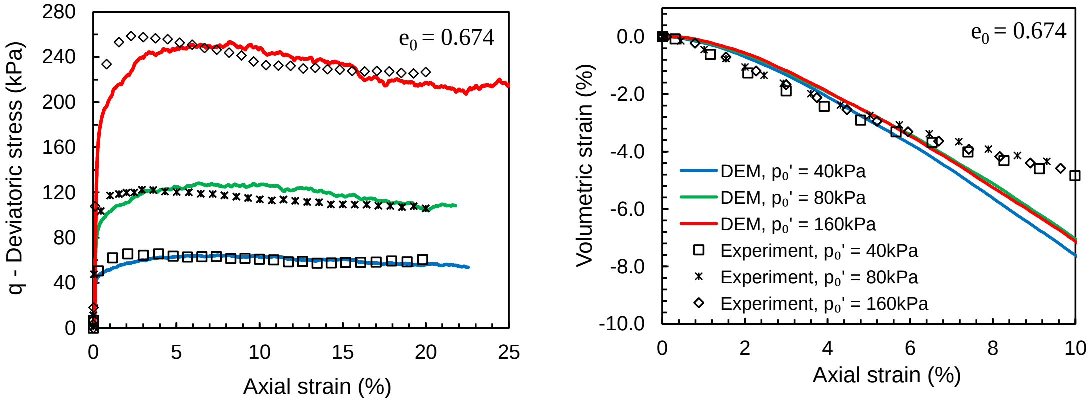

(a) (b)

Figure 3.9 Drained triaxial compression (constant p') of DEM simulation at $e_0 = 0.674$, comparing with Nevada sand tests at relative density of 60% with initial confining pressure of 40kPa, 80kPa and 160kPa: (a) stress paths and (b)volumetric curves

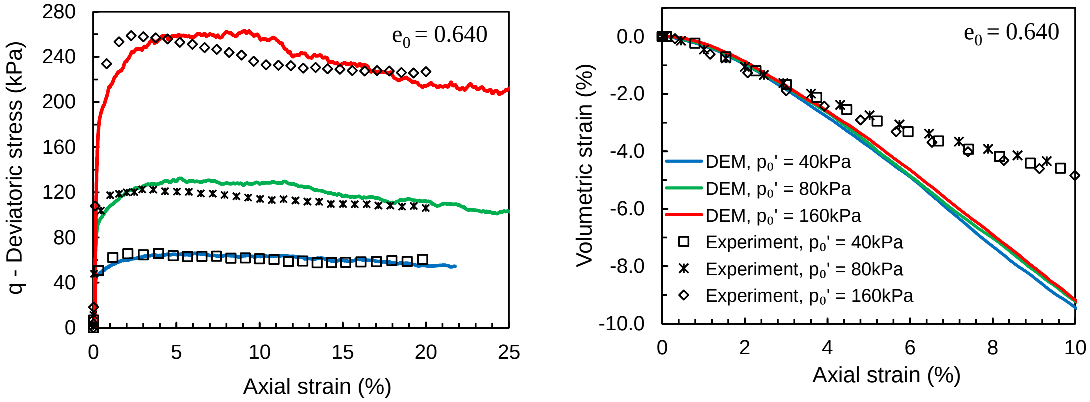

(a) (b)

Figure 3.10 Drained triaxial compression (constant p’) of DEM simulations at $e_0 = 0.640$, comparing with Nevada sand tests at relative density of 60% with initial confining pressure of 40kPa, 80kPa and 160kPa: (a) stress paths and (b)volumetric curves

The above figures showcase how well the high-fidelity DEM model replicate the pressure-sensitive responses of Nevada sand. We observe that the particle assemblies composed of bumpy particles are able to reproduce the shear responses and friction angles observed in triaxial experiments conducted at different confining pressure levels. Nevertheless, a sizable discrepancy in volumetric responses at finite deformation range is also noticed. These results imply that the DEM model currently employed in this study is a reasonable high-fidelity model when the strain-level is small. Nevertheless, caution must be exercised when interpreting the volumetric responses from the extended database. It is also worthy to mention that results from Kuhn et al. [156] illustrated that the shear responses may be artificially stiffen if the load increment is too large. To avoid this issue, the same load increment $\Delta\varepsilon_{zz} = \pm 5.0 \times 10^{-7}$ was used for all of the DEM simulations in this chapter.

3.3.3 Database expansion with virtual tests

The experimental database was supplemented by simulated constitutive responses obtained form DEM simulations. These DEM simulations are conducted with particle assemblies of compatible relative densities and with grain-scale contact law parameters calibrated from experimental data. In the numerical examples, we limit our scopes on predicting the stress paths that were initially isotropic. Hence, the virtual database will only contain stress path of particle assemblies that were initially isotropically consolidated. The stress paths used for database expansion include 1) monotonic undrained triaxial compression (TC), triaxial extension (TE) and simple shear (SS) tests; 2) monotonic drained conventional triaxial compression (CTC) tests; 3) monotonic true triaxial tests with constant mean effective stresses and various loading paths quantified by the intermediate principal stress ratio $b = \sigma_2' - \sigma_3' \Big/ \sigma_1' - \sigma_3'$ (as shown in Figure 3.11) [183]; 4) cyclic undrained unidirectional simple shear (CySS) and triaxial compression tests (CyTC). In this study, 15 DEM assemblies were considered with initial void ratios $e =$0.898, 0.789, 0.785, 0.783, 0.767, 0.746, 0.734, 0.707, 0.674, 0.640, 0.609, 0.577, 0.550, 0.529, 0.512 which were pre-consolidated to different confining pressures

$p_0 = 40, 80, 100, 160, 300\mathrm{kPa}$. These initial assemblies were then subjected to different loading paths to expand the experimental database.

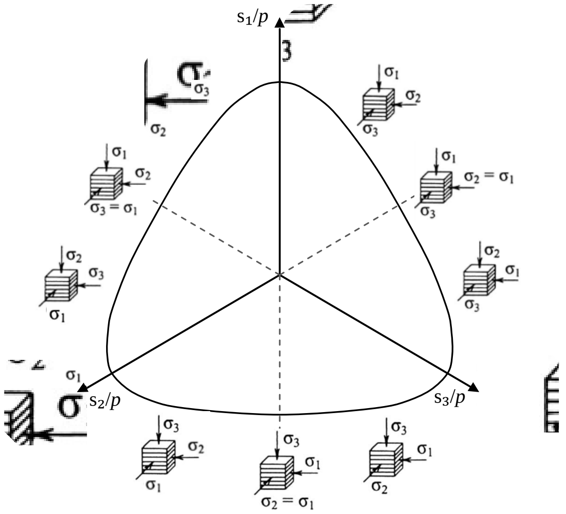

Figure 3.11 Application of major, intermediate and minor principal stresses, σ_1, σ_2 and σ_3, to DEM assemblies in true triaxial tests to achieve all directions in the stress ratio π-plane [183] (s_1, s_2 and s_3 are deviatoric principal stresses)

3.4 Identification of Dafalias-Manzari model parameters

In this section, we present the procedure to identify material parameters using EDD concept. We herein use one of the most commonly used critical state plasticity model, Dafalias-Manzari (DaMa) model [15], as an example to illustrate how EDD is built, calibrated and utilized for material characterization. We want to emphasize that the proposed EDD procedure is applicable to other path-dependent materials.

3.4.1 Identification of DaMa model parameters

In order to predict the response of soils via a macroscopic constitutive model, it is necessary to determine the initial material state, drainage condition, and the model parameters. The initial state of soil is described by parameters include the initial effective confining pressure, p_0, and initial void ratio, e_0. A set of 15 parameters is required to completely define the two-surface elastoplastic model in a fully three-dimensional space. These parameters can be grouped into three categories: i) elastic parameters, G_0, ν; ii) critical state parameters, $M, c, e_0^c, \lambda, \xi$; and iii) model parameters such as state parameter constants n^b, n^d, yield surface parameter m, hardening constants, h_0, c_h, dilatancy parameter A_0 and fabric-dilatancy constants $z_{\max}, c_z$.

In a conventional calibration procedure for determining DaMa model parameters, a two-step calibration process is needed. In step 1, the elastic and critical state parameters are first manually determined with a high accuracy directly from experimental test data. The parameter of elastic shear modulus G_0 and Poisson's ratio ν are path independent and can be obtained from lease square regression of the small strain monotonic shearing behavior at various confining pressures. We assume that the critical state constants $M, c, e_0^c, \lambda, \xi$ for a given soil are independent of initial state and loading condition. Therefore, the critical state and can be determined through curve fitting from a plot of triaxial test data that approach the critical state in $e - p/p_{at}$ space. While in Step 2, the model specific parameters can be obtained by trial-and-error or through a numerical optimization procedure. In many situations, an unbalanced combination of the model specific parameters may lead to numerical instability, especially when the mean effective stress approaches zero [144]. One possible way to address this issue is to employ a multistep characterization process by which only a subset of parameters is characterized at a time against experiments that mostly affect these parameters with carefully selected upper and lower bounds [34].

3.4.2 Parameter identification for Nevada sand

In this section, a comparison of DaMa model simulations and DEM trained data corresponding to monotonic triaxial tests is presented. To study the sensitivity of model parameters on different types of tests, material parameters are calibrated against tests under combinations of different initial material states, drainage conditions and loading conditions for Nevada sand. The calibrated material parameters are listed in Table 3.3.

Table 3.3 Model parameters of the DaMa model calibrated for Nevada sand

Parameter function	Parameter index	Andrade et al. [166]	Shahir et al. [143]	Case _12a_	Case _1b_	Case _2b_	Case _12b_	Case _2a*#_
Elasticity	G_0	125	150	150	150	150	150	150
	v	0.05	0.05	0.05	0.05	0.05	0.05	0.05
Critical state	M	1.45	1.14	1.14	1.34	1.34	1.34	1.08
	c	0.78	0.78	0.78	0.78	0.78	0.78	0.78
	λ_c	0.09	0.027	0.098	1.13	1.13	1.13	0.8
	e_0^c	0.737	0.83	0.833	0.833	0.833	0.912	0.73
	ξ	1.0	0.45	0.12	0.12	0.12	0.12	1.0
Yield surface	m	0.01	0.02	0.02	0.02	0.02	0.02	0.02
Plastic modulus	h_0	4.5	9.7	9.7	9.416	9.416	9.402	9.25
	c_h	1.05	1.02	1.02	1.2	1.28	1.21	1.03
	n^b	1.1	2.56	2.56	2.038	2.038	1.307	1.49
Dilatancy	A_0	0.804	0.81	0.81	0.81	0.796	0.85	0.81
	n^d	5.5	1.05	1.05	5.78	1.014	1.78	4.98
Fabric-dilatancy	$z_{\max}$	10	5	5	5	5	5	10
	c_z	500	800	800	800	800	800	500

Note that the italic symbols appeared after cases have the meaning as follows: *1* denotes loose–medium dense samples, *2* denotes medium dense-dense sample, *a* denotes monotonic undrained triaxial tests, *b* denotes monotonic drained triaxial tests, * denotes tests with variable loading paths, and # denotes laoding-unloading tests.

3.4.2.1 Critical state

The critical state surface is introduced in the DaMa model to incorporate the critical state soil mechanics concept into the bounding surface plasticity model. When the critical state is reached, both the bounding surface and dilatancy surface converge to the critical state surface in the stress space. On the other hand, both the hardening rule and the amount of plastic dilatation is dictated by the distance between both bounding surfaces to the critical state surface, and the dilatancy surface to the critical state surface respectively. Therefore, determining the location of the critical state surface via calibrating the critical state parameters is crucial to the forward prediction capacity of the calibrated DaMa model. The DEM assemblies were deformed through the critical state so as to simulate the critical state responses of Nevada sand. The critical state parameters that locate the critical state lines in the effective stress and state paths are identified. In the calibration process, a constrained optimization procedure is first run to determining the set of the critical state parameters $M, c, e_0^c, \lambda, \xi$ that minimize the errors measured by the objective function. Figure 3.12 plots the critical state surface in the stress ratio π -plane corresponding to the calibrated parameters set *Case 12b* in Table 3.3. The loading paths for drained true triaxial tests predicted by DEM simulations and the loading paths for the lab experiments are also shown in Figure 3.12. As seen from Figure 3.12, conventional lab experiments are conducted in limited loading paths, i.e. triaxial compression ($b = 0$) and triaxial extension ($b = 1$). While using DEM, under constant p' constraint, σ_1' , σ_2' and σ_3' were controlled based on Figure 3.11 to achieve constant b conditions, with b values representing different loading directions. The monotonic triaxial tests considered in the calibration help improve the DaMa model prediction of deviatoric plastic strain under radial monotonic loading.

3.4.2.2 Monotonic triaxial tests

Figure 3.13 to Figure 3.16 show the constitutive responses simulated by the DaMa model in monotonic drained conventional triaxial compression (CTC) tests for samples of various relative densities and initial confining pressures. The parameters referred as Case *12b* in Table 3.3 were used in this set of simulations. The comparison between DEM trained data and DaMa model predicted results are presented in terms of q vs. axial strain, and e vs. p' plots. These results show the model can produce a reasonably well prediction of Nevada sand behavior for a broader range of densities and initial mean confining pressures using one set of parameters.

Figure 3.17 depicts DaMa model prediction results of $q - p'$ responses (Case *12a* in Table 3.3) for monotonic undrained triaxial compression tests. The overall trend of the sand behavior under undrained compression is well captured. It can be observed that in higher density and lower confining pressure samples, the sand is highly dilatant, while in lower density and higher confining pressure samples, the opposite effect is observed. Good agreement of the $q-p'$ responses is obtained for loose and medium dense samples (i.e. e_0 = 0.783 and 0.720). However, the DaMa model predicts larger slopes of the CSL at large strains for dense samples than what is expected in the trained data.

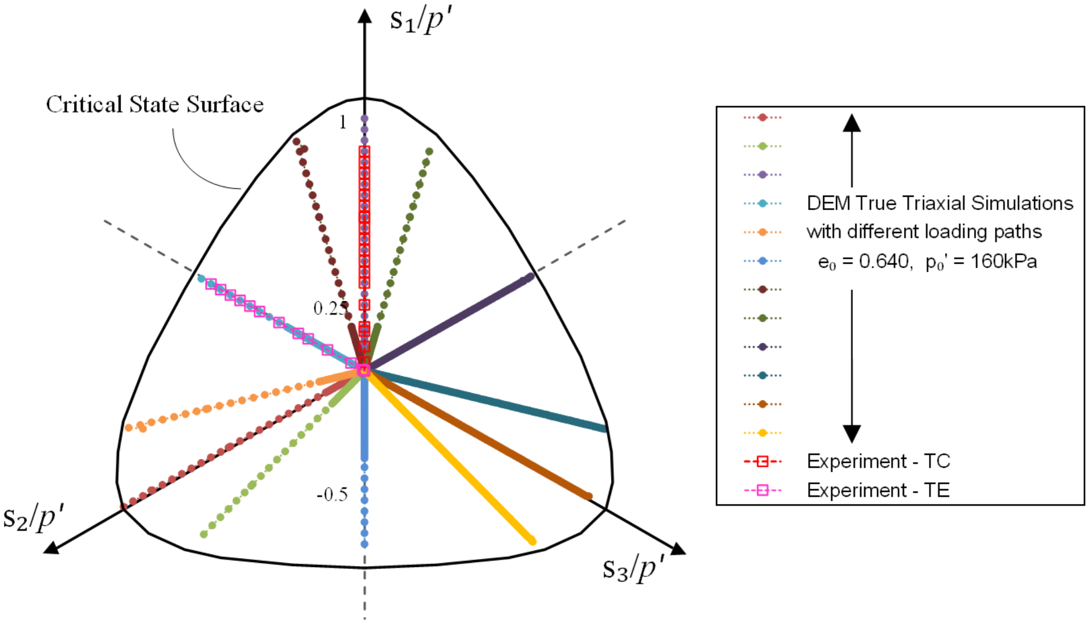

Figure 3.12 Calibrated critical state surface for DaMa model, and the loading paths of monotonic triaxial tests for DEM simulations and lab experiments in the stress ratio π - plane (s_1, s_2 and s_3 are deviatoric principal stresses)

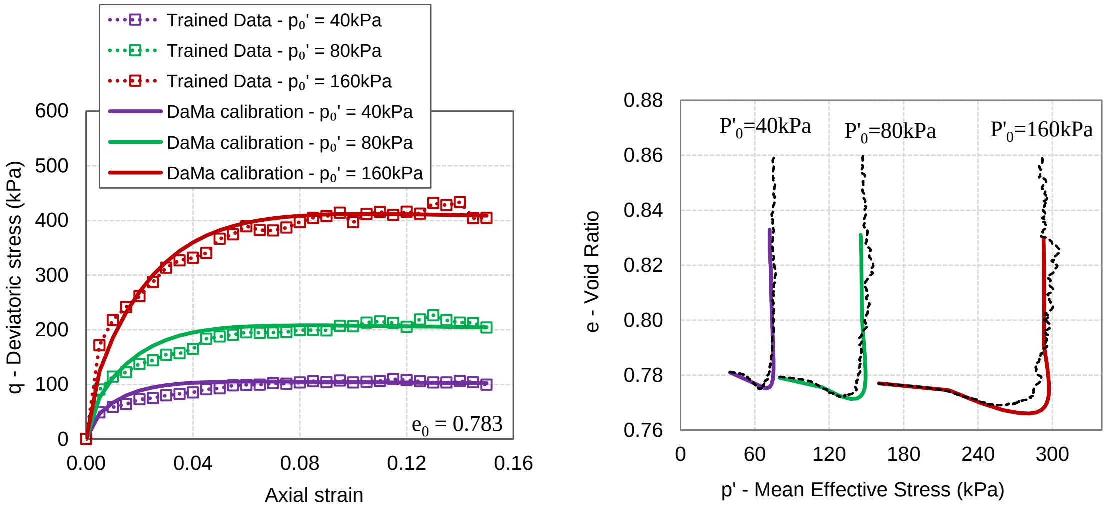

(a) q vs. axial strain (b) void ratio vs. mean effective stress

Figure 3.13 DaMa model prediction for CTC tests on samples with different initial confining pressures (e_0 = 0.783)

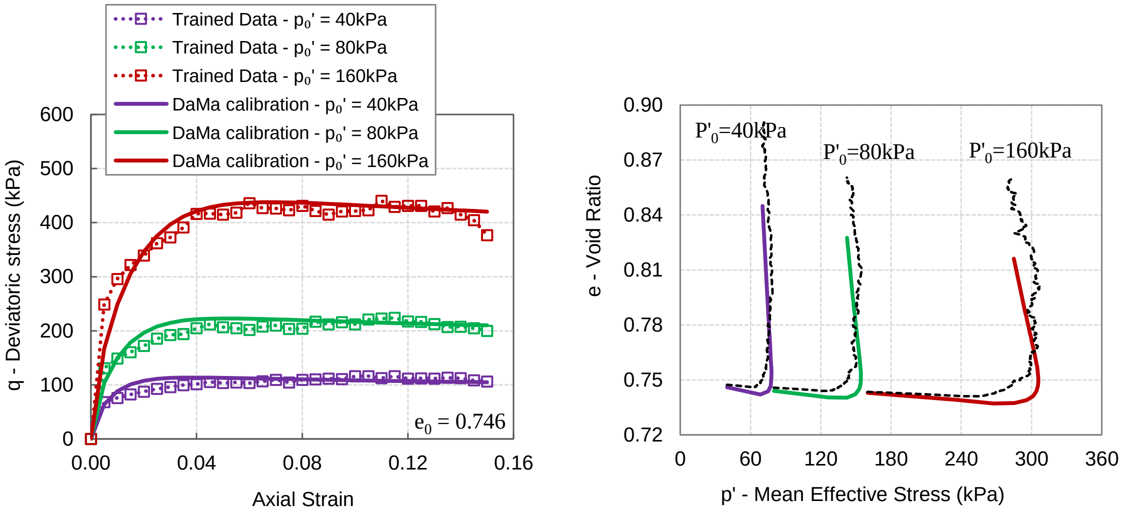

(a) q vs. axial strain (b) void ratio vs. mean effective stress

Figure 3.14 DaMa model prediction for CTC tests on samples with different initial confining pressures (e_0 = 0.746)

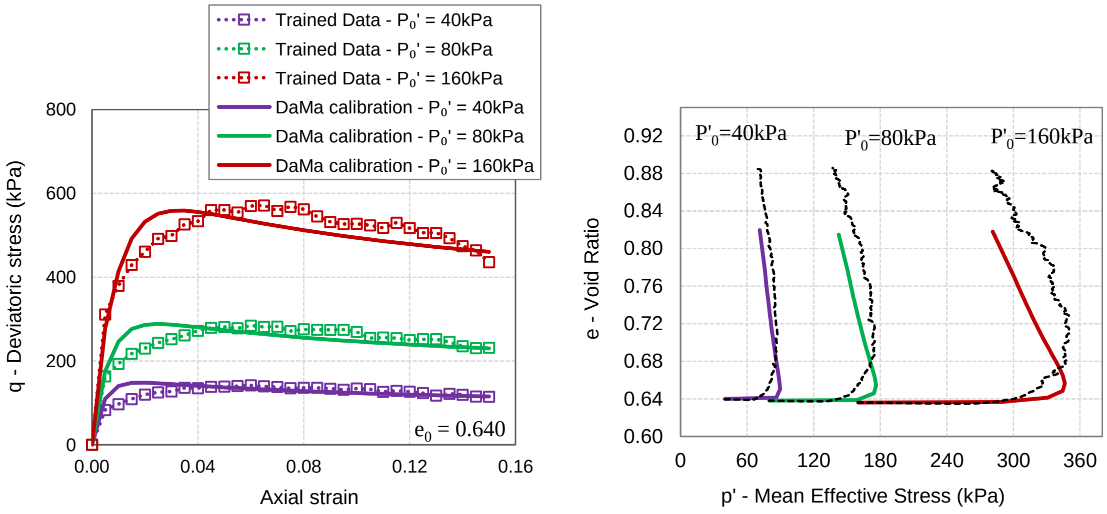

(a) q vs. axial strain (b) void ratio vs. mean effective stress

Figure 3.15 DaMa model prediction for CTC tests on samples with different initial confining pressures (e_0 = 0.640)

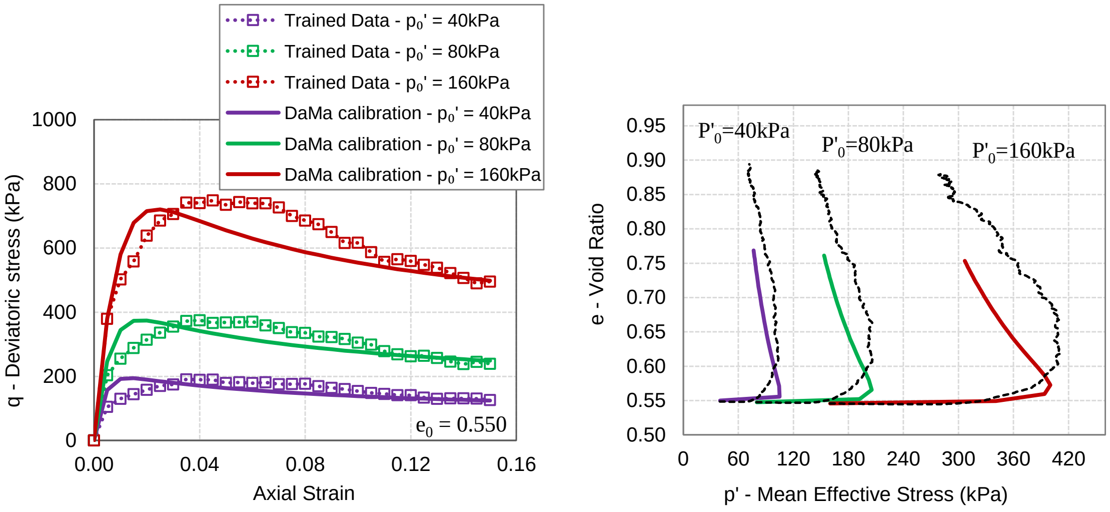

(a) q vs. axial strain (b) void ratio vs. mean effective stress

Figure 3.16 DaMa model calibration for CTC tests on samples with different initial confining pressures (e_0 = 0.550)

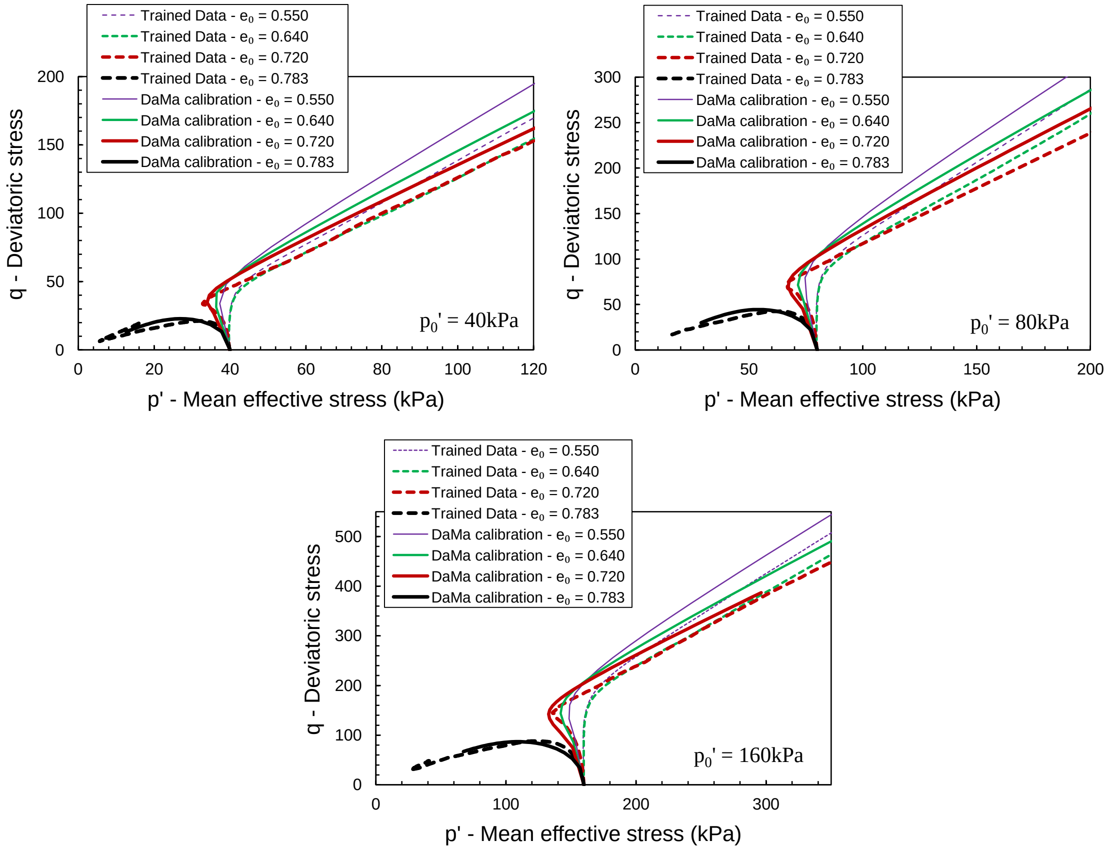

Figure 3.17 DaMa model calibration of $q - p'$ responses for monotonic undrained triaxial compression tests on samples with different initial confining pressures and densities

3.5 Assessment of forward predictions with calibrated Dafalias-Manzari model

In this study, a subset of the data in the EDD, which is called the verification/test set, is purposely excluded from being used for material identifications of both the high- and low- fidelity models (see Figure 3.1). Instead, these unused data are employed to assess the accuracy and robustness of forward predictions. The verification set consists of experiments from both the laborotary tests and the virtual simulations. In this assessment study, we conduct the predicted simulations using the calibrated DaMa model and compare the predicted results with this subset of experimental data that have purpusely not used for calibration, Figure 3.18 shows comparisons between predictions from DaMa model and verification data for monotinic triaxial compression tests. The verification tests consist of both drained and undrained triaxial compression loading paths of an isotropically consolidated Nevada sand, in which the DEM virtual simualtions are conducted with densities e_0 = 0.529 and 0.707 under initial mean effective pressure p_0' = 100, 200 and 300kPa, respectively. The experimental data from Kutter et al. [184] for Nevada sand with $D_r = 65\%$ and initial mean effective pressure p_0' = 100, 250 and 400kPa are also compared with DaMa model prediction (see Figure 3.18(c)). The stresss-strain relation shown in Figure 3.18 indicates that the calibrated DaMa model can also produce a reasonably good prediction of Nevada sand behavior for the tests in the verification set of EDD. Comparisons of results from Figure 3.18(a) and (b) suggest that the calibrated DaMa model replicates the strain-strain curves more accurately at the drained limit than those at the undrained limit. Nevertheless, both the drained and undrained simulation results are able to predict the friction angle at steady state quite well. These well-matched responses are encouraging given the fact that there is no microstructural information available to calibrate the high-fidelity DEM model and there is no attempt to explicitly model the particle shape variation in this study.

Another assessment test we conducted is a comparison between the simulated undrained cyclic simple shear loading responses predicted by the calibrated DaMa model and the experimental data reported in Arulmoli et al. [169] for Nevada sand with $D_r = 40\%$ and $p_0' = 80\mathrm{kPa}$. The purpose of this test is to assess how well the calibrated low-fidelity model predicts loading paths not included in the EDD database. Such a test is important, as the loading histories of soils are often significantly different and more complicated than the idealized cases studied in the laboratory. The cyclic test was numerically simulated using the DaMa model with parameters of Case *2a*#* as reported in Table 3.3. In this test, cyclic shearing was applied in the horizontal direction in a load-controlled manner with a cyclic stress amplitude of $\pm 7.4\mathrm{kPa}$. Figure 3.19 compares curves of the shear stress vs. mean effective stress, shear stress vs. shear strain and pore-water pressure (PWP) change vs. shear train, obtained from both lab experiment and DaMa model prediction. The comparison shows that the DaMa model predictions are qualitatively consistent with the experimental responses. Similar to what was observed in the monotonic tests, the discrepancy become evident in the large strain region as shown in the shear stress vs. shear strain curve. The inaccurate prediction for the cyclic test by DaMa model may be attributed to the fact that most of the experiments used to construct the database are monotonic and the DEM model does not reflect the real geometrical features of grains, therefore, the parameters calibrated based on such database cannot accurately capture the cyclic responses in which the material may undergo very complex behaviors, such as multiple phase transformation. In addition, the DaMa model used in this study is a small strain plasticity model and does not incorporate the geometrical nonlinearity. We found that the accuracy and robustness of the low-fidelity surrogate model reduce when the simulated loading paths are different from those available from the experimental data (e.g., drained vs. undrained, monotonic vs. cyclic). This observation is consistent of the previous studies [65, 144]. Presumably, those issues can be resolved by incorporating more advanced high-fidelity method, such as granular element method [185] to extend the material database more accurately, and/or more comprehensive low-fidelity constitutive models that incorporate more detailed mechanisms, such as fabric changes, cyclic mobility and geometrical nonlinearity. Those studies will be considered in the future study but is out of the scope of this work.

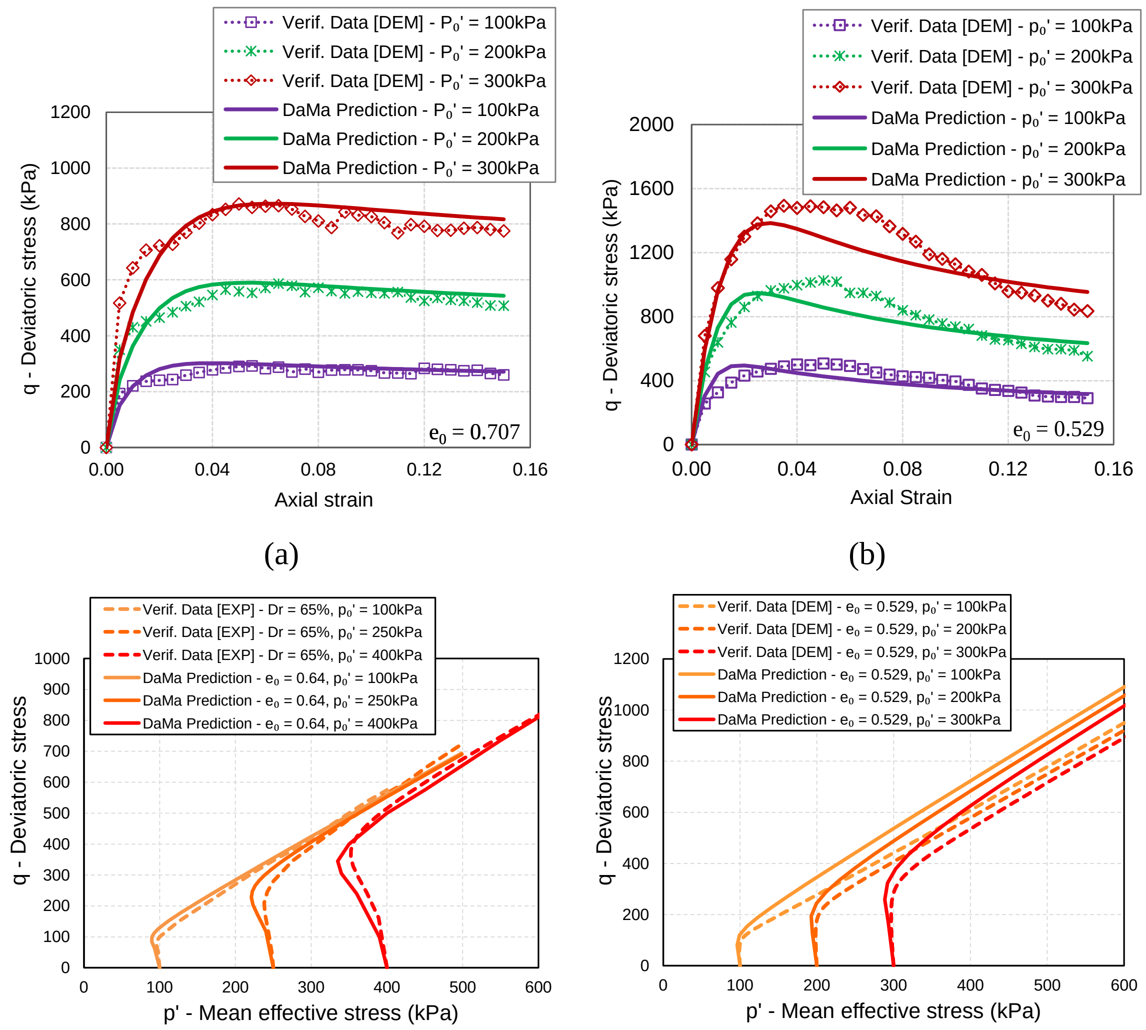

(a) (b)

(c) (d)

Figure 3.18 Comparison between DEM verification data and DaMa model prediction for: (a) and (b) drained monotonic conventional triaxial compression (CTC) tests, and (c) undrained triaxial compression tests (experimental data in (c) are from Kutter et al. [184])

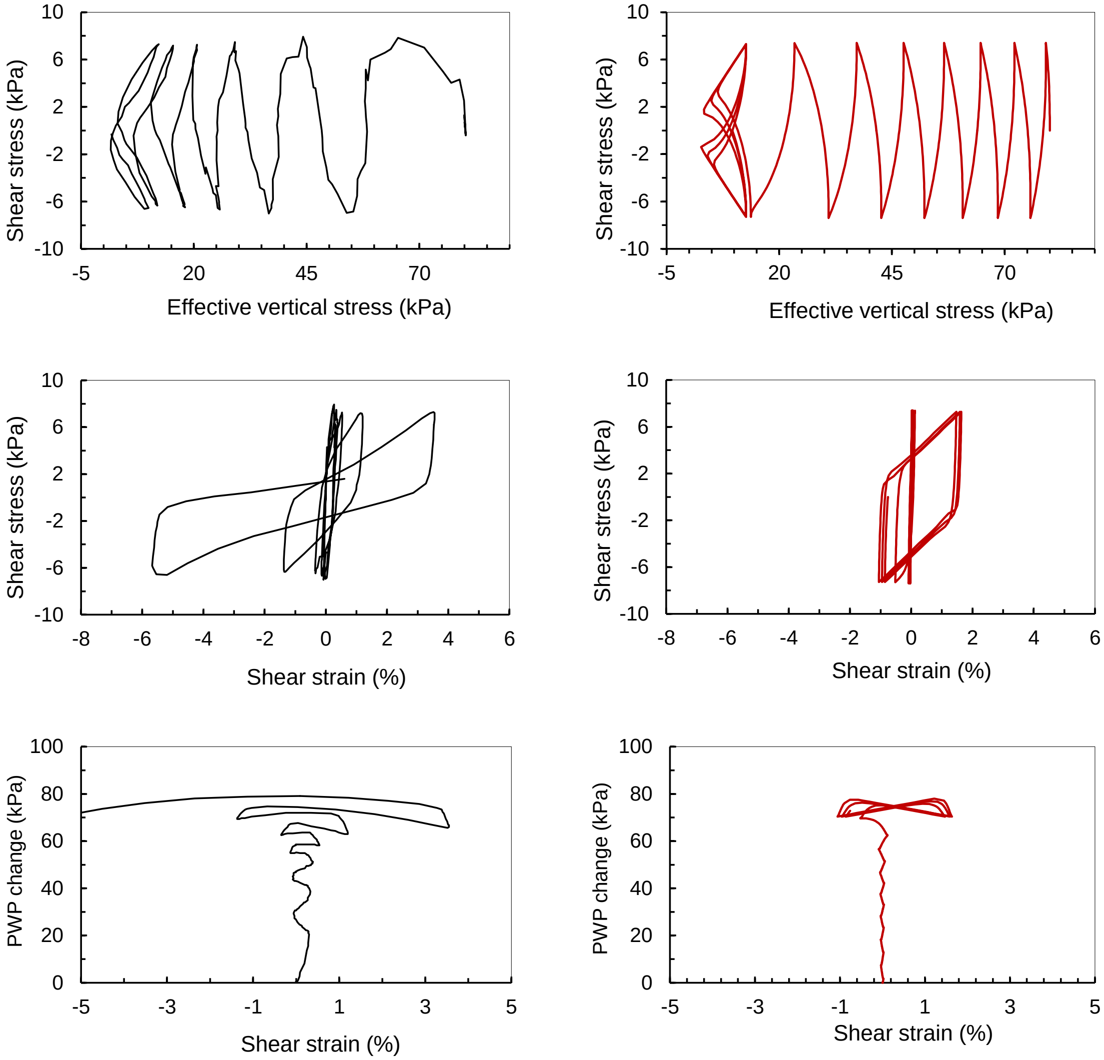

(a)

(b)

Figure 3.19 Undrained cyclic simple shear test for Nevada sand: $\mathrm{Dr} = 40\%$ and $p'_0 = 80\mathrm{kPa}$: (a) experimental data from Arulmoli et al. [169]; (b) Dafalias-Manzari model prediction.

3.6 Conclusions

In this chapter, we present a new simulation-based database extension technique aimed at calibrating comprehensive critical state plasticity models with limited available experimental data. By utilizing a high-fidelity model (DEM) that has been calibrated against experiments, additional high-fidelity simulations are used to supplement experimental data by the so-called extended digital database (EDD). The EDD essentially provide additional constraints essential for identifying the optimized parameter set for the low-fidelity phenomenological constitutive models. When experimental data is expensive to generate or inaccessible, this approach provides a much-needed alternative. Numerical experiments conducted herein show that the proposed multilevel calibration approach is capable of obtaining material parameters for capturing the behavior of cohesion-less sand under various drainage and monotonic loading conditions, void ratios and confining pressures at the small deformation range, but the results are less satisfactory for cyclic and large deformation problems.

Chapter 4

A Regularized Phenomenological Multiscale Damage Model

In this chapter, a regularized phenomenological multiscale model is investigated, in which elastic properties are computed using direct homogenization and subsequently evolved using a simple three-parameter orthotropic continuum damage model. This chapter is reproduced from the paper co-authored with Vasilina Filonova, Nan Hu, Zifeng Yuan, Jacob Fish, Zheng Yuan and Ted Belytschko, which was published in the International Journal for Numerical Methods in Engineering [74].

4.1 Introduction

While importance of multiscale methods has been recognized for several decades, the overwhelming computational complexity of these methods precluded their successful utilization in practice except for linear problems. It was the outstanding paper of Guedes and Kikuchi [35] that provided an eloquent approach to link microstructural data with effective linear material properties using asymptotic homogenization theory in combination with a finite element method. While mathematical theory of homogenization was established more than a decade earlier [186, 187], the paper of Guedes and Kikuchi spurred tremendous interest in computational mechanics community. From computational point of view, the O(1) homogenization theory for a periodic linear elastic heterogeneous medium requires linear solution of the unit cell model subjected to six right hand side vectors. On the other hand for nonlinear problems, computational cost is several orders of magnitude higher since nonlinear unit cell problem has to be solved at each macro-element quadrature point, at each load increment and at each Newton iteration of the macroscale problem. This is formidable computational cost for large scale structural systems. This tyranny of scales can be effectively addressed by combination of parallel methods and by introducing an approximate solution of the unit cell problem. An approximation of the microscale solution has considerable merit since the macroscale quantities of interest are often show little sensitivity to the accuracy of the unit cell solution. In general, an error in the unit cell solution arises due to an approximation of the mathematical model and/or discretization of the unit cell model. For instance, the Aboudi method of cells [188, 189] that found its way into commercial grade multiscale software [128] belongs to the latter category. Other noteworthy contributions belonging to the latter category are Voronoi cell method [190, 191] and the spectral method [192]. There are two approaches belonging to the category of approximate mathematical models, namely, (i) the reduced order models and (ii) the phenomenological models, both schematically depicted in Figure 4.1.

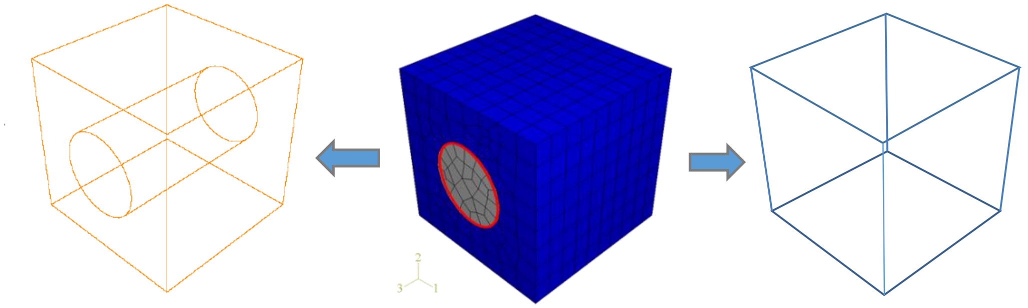

Reduced order model

Micromechanical model

Phenomenological model

Figure 4.1 Idealizations of the micromechanical model (center): reduced order model (left) and phenomenological model (right)

Development of reduced order models for heterogeneous continua has been an active research area in the past decade. Perhaps, one of the oldest reduced order approaches is based on purely kinematical Taylor's hypothesis which assumes uniform deformation at the fine scale; it satisfies compatibility but fails to account for equilibrium across microconstituents boundaries. A major progress in reduced order modeling (at the expense of computational cost) has been made by utilizing meshfree reproducing kernel particle method (RKPM) [193, 194], methods based on control theory including balanced truncation [195, 196], the optimal Hankel norm approximation [197], and proper orthogonal decomposition [198], the Transformation Field Analysis (TFA) [199, 200] and the reduced order homogenization methods [39, 201-206].

In this chapter we focus on the second and the oldest category of approximate mathematical models, namely the phenomenological models. We limit our discussion to brittle materials governed by continuum damage mechanics. There is a considerable literature on phenomenological multiscale models in particular for composites (see [207-215] and references therein). The primary goal of this chapter is to develop a simple phenomenological model that possesses the following characteristics:

(i) Accurate resolution of microscopic fields for linear heterogeneous materials. Since the cost of direct homogenization for linear problems is a small fraction of the overall computational cost, no approximation (except for periodicity assumption) should be introduced for linear problems.

(ii) The lowest number of state variables. The goal is to be able to analyze complex microstructures (woven and fabric composites) with minimal number of state variables. While in general, damage evolution in complex materials may require second, fourth or even eighth order damage tensors, we show that reasonably accurate results can be obtained with just three damage variables defined in principle directions of the *effective strain* tensor (defined in Section 4.3).

(iii) A unified regularization scheme. We present a unified regularization framework to analyze material response in post failure regime. We define an *effective softening* strain and introduce a unified regularization scheme for both constitutive law rescaling models [216] and nonlocal models [73].

(iv) Regularized element erosion (deletion) scheme. Despite its simplicity crack propagation by element erosion has been a subject of considerable criticism due to its inconsistency with fracture mechanics, lack of characteristic length and pathological mesh sensitivity. We show that the element erosion technique when exercised with one of the two regularization schemes does not suffer of the above shortcoming and can reproduce experimental data.

4.2 Linking micromechanical and phenomenological continuum damage models

Consider a periodic unit cell where elastic microstructural phases, such as inclusion and matrix phases, possess microcracks. Assume that each microphase can be adequately modeled using continuum damage mechanics (CDM). An overall response of the composite can be obtained using nonlinear homogenization (see for instance [34, 35]). In the two-scale asymptotic mathematical homogenization theory, various fields are assumed to depend on two coordinates: $\boldsymbol{x}$ - as the coarse-scale (macro) position vector in the coarse-scale domain Ω and $\boldsymbol{y}$ - as the fine-scale (micro) position vector in the unit cell domain Θ. These two coordinates are related by $\boldsymbol{y} = \boldsymbol{x}/\zeta$ with $0 < \zeta << 1$. The unit cell domain Θ is typically chosen to be an open rectangular parallelepiped

$$\Theta = \left]0, l_1\right[\times \left]0, l_2\right[\times \left]0, l_3\right[\tag{4.1}$$

The fine-scale structure of the unit cell can be either periodic or random, but the solution is assumed to be locally periodic [186, 187]. The volume of the unit cell is denoted by $\left|\Theta\right|$.

Various fine-scale response fields, such as the stress $\sigma_{ij}^f(\boldsymbol{x},\boldsymbol{y})$ in the unit cell domain, are assumed to be locally periodic in Θ

$$\sigma_{ij}^f(\boldsymbol{x},\boldsymbol{y}) = \sigma_{ij}^f(\boldsymbol{x},\boldsymbol{y}+\boldsymbol{kl}) \tag{4.2}$$

Since each microconstituent remains elastic, the fine-scale stress field $\sigma^f(\boldsymbol{x},\boldsymbol{y})$ in the unit cell can be described in terms of the coarse-scale stress $\sigma(\boldsymbol{x})$ and the instantaneous stress influence functions $\boldsymbol{M}(\boldsymbol{x},\boldsymbol{y})$, which depend on the current state of damage (or microcracking)

$$\sigma_{ij}^{f}(\boldsymbol{x},\boldsymbol{y}) = M_{ijkl}(\boldsymbol{x},\boldsymbol{y})\sigma_{kl}(\boldsymbol{x}) \tag{4.3}$$

where $M_{ijkl}(\boldsymbol{x},\boldsymbol{y})$ can be computed by solving linear elastic boundary value problem of a unit cell subjected to various unit overall stresses. From Equation (4.3) the average stress within a micro-phase β is given by

$$\begin{aligned} \sigma_{ij}^{\beta} &= \frac{1}{\left|\Theta^{\beta}\right|}\int_{\Theta^{\beta}} \sigma_{ij}^{f}(\boldsymbol{x},\boldsymbol{y})d\Theta = M_{ijkl}^{\beta}(\boldsymbol{x})\sigma_{kl}(\boldsymbol{x}) \\ M_{ijkl}^{\beta}(\boldsymbol{x}) &= \frac{1}{\left|\Theta^{\beta}\right|}\int_{\Theta^{\beta}} M_{ijkl}(\boldsymbol{x},\boldsymbol{y})d\Theta \end{aligned} \tag{4.4}$$

where $\left|\Theta^{\beta}\right|$ denotes the volume of the micro-phase β and $M_{ijkl}^{\beta}(\boldsymbol{x})$ is the instantaneous phase stress influence function.

For nonlinear problem with evolving crack/voids, $M_{ijkl}^{\beta}(\boldsymbol{x})$ has to be repeatedly recomputed, which presents the computational bottleneck. Thus an approximation in the form of phenomenological modeling will be subsequently pursued.

To establish the link between the micromechanical (direct homogenization) and phenomenological approaches, the stress phase influence function $M_{ijkl}^{\beta}(\boldsymbol{x})$ is approximated using multiplicative decomposition as

$$M_{ijkl}^{\beta}(\boldsymbol{x}) = M_{ijst}^{el\ \beta}(\boldsymbol{x})M_{stkl}^{in\ \beta}(\boldsymbol{x}) \tag{4.5}$$

where $M_{ijst}^{el\ \beta}(\boldsymbol{x})$ is damage-free (i.e., free of cracks or voids) stress influence function in phase β and $M_{ijst}^{in\ \beta}(\boldsymbol{x})$ is a damaged-induced correction. The latter is closely related to the reduced order homogenization [39, 201-206] where $M_{ijst}^{in\ \beta}(\boldsymbol{x})$ is related to the eigenstrain influence functions. Further approximation is introduced by smearing the inelastic influence functions as follows

$$M_{stkl}^{in\ \beta}(\boldsymbol{x}) \equiv M_{stkl}^{in}(\boldsymbol{x}) \tag{4.6}$$

Substituting Equation (4.6) into Equations (4.4) and (4.5) yields

$$\sigma_{ij}^{\beta} = M_{ijst}^{el\ \beta}(\boldsymbol{x}) M_{stkl}^{in}(\boldsymbol{x}) \sigma_{kl}(\boldsymbol{x}) \tag{4.7}$$

Summing Equation (4.7) over all microphases yields

$$\bar{\sigma}_{ij}(\boldsymbol{x}) = M_{stkl}^{in}(\boldsymbol{x}) \sigma_{kl}(\boldsymbol{x}) \tag{4.8}$$

where we took advantage of the well-known property of elastic influence functions $\sum_{\beta} M_{stkl}^{el\ \beta}(\boldsymbol{x}) = I_{stkl}$. In Equation (4.8), $\bar{\sigma}_{ij}$ is so-called effective stress in the homogenized (anisotropic) elastic unit cell having discrete defects. It is instructive to point out that

$$\bar{\sigma}_{ij} = \frac{1}{|\Theta|} \int_{\Theta} \sigma_{ij}^{f}(\boldsymbol{x}, \boldsymbol{y}) d\Theta \neq \sigma_{ij} \tag{4.9}$$

Hereafter, for simplicity of nomenclature we will omit dependence on ***x***.

4.2.1 A simple orthotropic damage model

We consider three Cartesian coordinate systems: the global coordinate system (GCS), denoted by ***x***, the fixed material coordinate system (MCS) where the damage-free orthotropic constitutive equations are defined, denoted by $\boldsymbol{x}'$, and the instantaneous damage coordinate system (DCS) where damage evolution laws are defined, denoted by $\tilde{\boldsymbol{x}}$. Various tensor quantities, such as stress $\boldsymbol{\sigma}$ and damage-free elastic constitutive tensor $\boldsymbol{L}$ can be defined in various coordinate systems

$$\begin{aligned} \boldsymbol{\sigma} &= \sigma_{ij} \boldsymbol{e}_i \otimes \boldsymbol{e}_j = \sigma'_{ij} \boldsymbol{e}'_i \otimes \boldsymbol{e}'_j = \tilde{\sigma}_{ij} \tilde{\boldsymbol{e}}_i \otimes \tilde{\boldsymbol{e}}_j \\ \boldsymbol{L} &= L_{ijkl} \boldsymbol{e}_i \otimes \boldsymbol{e}_j \otimes \boldsymbol{e}_k \otimes \boldsymbol{e}_l = L'_{ijkl} \boldsymbol{e}'_i \otimes \boldsymbol{e}'_j \otimes \boldsymbol{e}'_k \otimes \boldsymbol{e}'_l = \tilde{L}_{ijkl} \tilde{\boldsymbol{e}}_i \otimes \tilde{\boldsymbol{e}}_j \otimes \tilde{\boldsymbol{e}}_k \otimes \tilde{\boldsymbol{e}}_l \end{aligned} \tag{4.10}$$

where the unit vectors and tensor components transform as

$$\begin{aligned}
&\boldsymbol{e}_i' = \cos\; x_j, x_i' \;\; \boldsymbol{e}_j = Q_{ji}' \boldsymbol{e}_j, \quad \tilde{\boldsymbol{e}}_i = \cos\; x_j', \hat{x}_i \;\; \boldsymbol{e}_j' = \tilde{Q}_{ji}' \boldsymbol{e}_j' \\
&\sigma_{pq}' = Q_{ip}' Q_{jq}' \sigma_{ij}, \quad \tilde{\sigma}_{pq} = \tilde{Q}_{ip}' \tilde{Q}_{jq}' \sigma_{ij}' \\
&L_{pqst}' = Q_{ip}' Q_{jq}' Q_{ks}' Q_{lt}' L_{ijkl}, \quad \hat{L}_{pqst} = \tilde{Q}_{ip}' \tilde{Q}_{jq}' \tilde{Q}_{ks}' \tilde{Q}_{lt}' L_{ijkl}'
\end{aligned} \tag{4.11}$$

Following continuum damage formulation originally proposed by Chow and Wang [217], the stress $\tilde{\sigma}_{ij}$ is related to the effective stress $\tilde{\tilde{\sigma}}$ in the DCS by

$$\tilde{\sigma}_{ij} = \tilde{W}_{ijkl} \;\; w_I, w_{II}, w_{III} \;\; \tilde{\tilde{\sigma}}_{kl} \tag{4.12}$$

where w_I, w_{II}, w_{III} are three damage parameters defined in the DCS; $\tilde{W}_{ijkl}$ is a fourth order damage tensor possessing major and minor symmetries. $\tilde{W}_{ijkl}$ in the matrix form is denoted by $\left[\tilde{\mathbf{W}}\right]$ and is defined as

$$\tilde{\mathbf{W}} = \begin{bmatrix}
\sqrt{1 - w_I} & 0 & 0 & 0 & 0 & 0 \\
 & \sqrt{1 - w_{II}} & 0 & 0 & 0 & 0 \\
 & & \sqrt{1 - w_{III}} & 0 & 0 & 0 \\
 & & & \sqrt[4]{\;1 - w_{II} \quad 1 - w_{III}\;} & 0 & 0 \\
 & sym. & & & \sqrt[4]{\;1 - w_I \quad 1 - w_{III}\;} & 0 \\
 & & & & & \sqrt[4]{\;1 - w_I \quad 1 - w_{II}\;}
\end{bmatrix} \tag{4.13}$$

The damage tensor $\tilde{W}_{ijkl}$ is related to $\tilde{M}_{ijkl}^{in}$ (see Equation (4.8)) in the damage coordinate system by

$$\tilde{W}_{ijkl} = \;\; \tilde{M}_{ijkl}^{in} \;\; ^{-1} \tag{4.14}$$

To obtain the symmetric form of the instantaneous damage-dependent material properties in the DCS, denoted by $\tilde{\boldsymbol{\mathcal{L}}}_{ijkl}$, we employ the postulate of complementary elastic energy equivalence [218] between the $\tilde{\tilde{\sigma}}$ and $\tilde{\sigma}$

$$\tilde{\tilde{\sigma}}_{ij} \;\; \hat{L}_{ijkl} \;\; ^{-1} \tilde{\tilde{\sigma}}_{kl} = \tilde{\sigma}_{ij} \;\; \tilde{\boldsymbol{\mathcal{L}}}_{ijkl} \;\; ^{-1} \tilde{\sigma}_{kl} \tag{4.15}$$

which yields

$$
\begin{aligned}
\tilde{\sigma}_{ij} &= \tilde{\boldsymbol{\mathcal{L}}}_{ijmn}\tilde{\varepsilon}_{mn} \\
\tilde{\boldsymbol{\mathcal{L}}}_{ijmn} &= W_{ijkl}W_{mnpq}\tilde{L}_{klpq}
\end{aligned}
\tag{4.16}
$$

where $\tilde{L}_{klpq}$ denotes orthotropic elastic material properties of the crack-free material. The instantaneous damage-dependent constitutive tensor in any other coordinate system can be obtained by appropriate transformation defined in Equation (4.11).

<u>Remark 1</u>: The definition of the damage tensor Equation (4.13) reduces to $I_{ijkl}\sqrt{1-w}$ for an isotropic damage model, $w \equiv w_I = w_{II} = w_{III}$. This yields an isotropic fourth order constitutive tensor $\tilde{\boldsymbol{\mathcal{L}}}_{ijmn} = \ 1-\omega \ \tilde{L}_{ijmn}$.

To define the damage coordinate system (DCS) we first introduce the effective strain tensor $\boldsymbol{\kappa} = \kappa'_{ij}\boldsymbol{e}'_i \otimes \boldsymbol{e}'_j$. The components of the effective strain κ'_{ij} in the MCS are defined as

$$
\left[\boldsymbol{\kappa}'\right] = \begin{bmatrix}
D'_{11} & 0 & 0 & 0 & 0 & 0 \\
0 & D'_{22} & 0 & 0 & 0 & 0 \\
0 & 0 & D'_{33} & 0 & 0 & 0 \\
0 & 0 & 0 & D'_{23} & 0 & 0 \\
0 & 0 & 0 & 0 & D'_{13} & 0 \\
0 & 0 & 0 & 0 & 0 & D'_{12}
\end{bmatrix} \left[\boldsymbol{\varepsilon}'\right]
\tag{4.17}
$$

where D'_{ij} are material constants quantifying the sensitivity of various strain components to damage accumulation. For instance, if fibers are aligned in ‘11’ direction in the MCS, then $D'_{11} > 1$ represents reduced strength due to fiber buckling. On the hand, if the material is little sensitive to compression damage in the transverse direction 2, then $0 < D'_{22} << 1$ for $\varepsilon'_{22} < 0$ and $D'_{22} = 1$ for $\varepsilon'_{22} > 0$. The value of D'_{ij} for $i \neq j$ represent sensitivity the shear damage.

The unit vectors $\tilde{\boldsymbol{e}}_i$ corresponding to the damage coordinate system (DCS) are defined as follows

$$\tilde{\boldsymbol{e}}_i = \tilde{Q}'_{ji} \boldsymbol{e}'_j \tag{4.18}$$

where $\hat{Q}'_{ji}$ are principal directions of the effective strain κ'_{ij} in the MCS, and $\tilde{\kappa}_I, \tilde{\kappa}_{II}, \tilde{\kappa}_{III}$ are the principal values.

The damage evolution is defined in the DCS based on the value of each principal effective strain component, $\tilde{\kappa}_{\#}$, where $\# = I, II, III$:

For $\tilde{\kappa}_{\#} \geq 0$

$$w_{\#} = \begin{cases} 0 & ; \quad \tilde{\kappa}_{\#} \leq {}^0\tilde{\kappa}_{\#} \\ G \;\; \tilde{\kappa}_{\#} & ; \quad {}^0\tilde{\kappa}_{\#} < \tilde{\kappa}_{\#} \leq {}^1\tilde{\kappa}_{\#} \\ 1 & ; \quad \tilde{\kappa}_{\#} > {}^1\hat{\kappa}_{\#} \end{cases} \tag{4.19}$$

For $\tilde{\kappa}_{\#} < 0$

$$w_{\#} = \begin{cases} 0 & ; \quad \tilde{\kappa}_{\#} \geq -{}^0\tilde{\kappa}_{\#} \\ G \;\; \tilde{\kappa}_{\#} & ; \quad -{}^0\tilde{\kappa}_{\#} > \tilde{\kappa}_{\#} \geq -{}^1\tilde{\kappa}_{\#} \\ 1 & ; \quad \tilde{\kappa}_{\#} < -{}^1\tilde{\kappa}_{\#} \end{cases} \tag{4.20}$$

For bilinear stress-strain relation, the damage evolution equations is given as

$$G \;\; \tilde{\kappa}_{\#} \;\; = \frac{a}{\left|\tilde{\kappa}_{\#}\right|} + b \tag{4.21}$$

and

$$a = \frac{1}{\dfrac{1}{{}^1\tilde{\kappa}_{\#}} - \dfrac{1}{{}^0\tilde{\kappa}_{\#}}}; \quad b = \frac{-a}{{}^0\tilde{\kappa}_{\#}} \tag{4.22}$$

where the onset of effective strain ${}^0\tilde{\kappa}_{\#}$ and the failure strain ${}^1\tilde{\kappa}_{\#}$ in principal directions of the effective strain are obtained from the effective strain failure surface depicted in Figure 4.2.

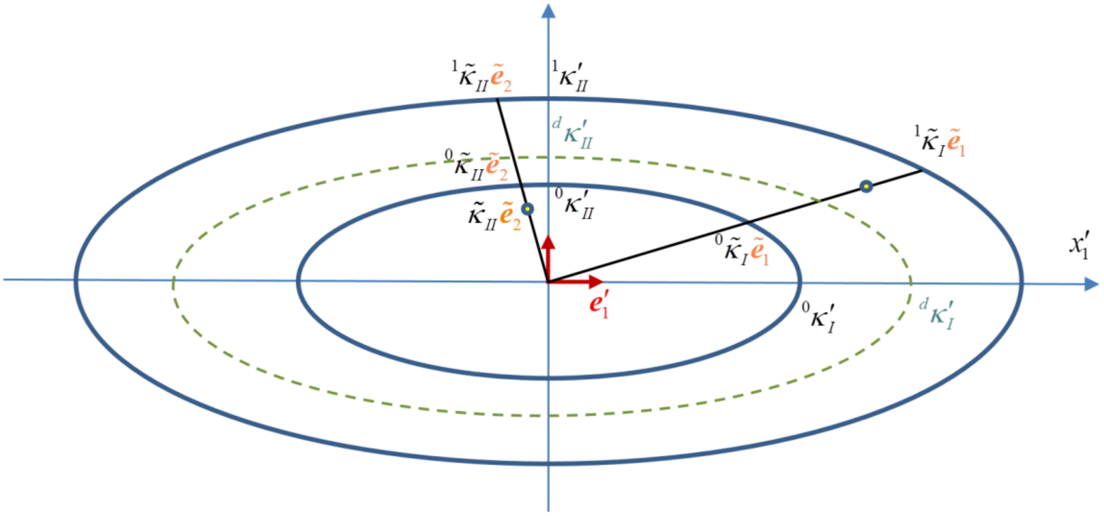

Figure 4.2 Effective strain surface in two dimensions. ${}^0\kappa'_\#$, ${}^1\kappa'_\#$ are material constant defined in the material coordinate system (MCS). $\boldsymbol{e}'_i$, $\tilde{\boldsymbol{e}}_i$ are the unit vectors in the material coordinate system and in the principal damage coordinate system. $\tilde{\kappa}_\#$ are the principal values of the effective strain. The dashed line denotes the current (trial) effective strain surface.

Given the onset of the effective strain ${}^0\kappa'_\#$ in the material coordinate system, the damage initiation surface in the DCS is defined as

$$\frac{{}^0x_1'^2}{{}^0\kappa_I'^2} + \frac{{}^0x_2'^2}{{}^0\kappa_{II}'^2} + \frac{{}^0x_3'^2}{{}^0\kappa_{III}'^2} = 1 \tag{4.23}$$

Likewise, given the failure strain ${}^1\kappa'_\#$ in the MCS, the damage failure surface is defined as

$$\frac{{}^1x_1'^2}{{}^1\kappa_I'^2} + \frac{{}^1x_2'^2}{{}^1\kappa_{II}'^2} + \frac{{}^1x_3'^2}{{}^1\kappa_{III}'^2} = 1 \tag{4.24}$$

Finally, given the principal damage coordinate system $\hat{\boldsymbol{e}}_i$, projecting the vectors of principal values ${}^0\tilde{\kappa}_{\#}\tilde{\boldsymbol{e}}_{\#}$, ${}^1\tilde{\kappa}_{\#}\tilde{\boldsymbol{e}}_{\#}$ onto the MCS yields

$$ {}^m x_i' = {}^m\tilde{\kappa}_{\#}\tilde{\boldsymbol{e}}_{\#} \cdot \boldsymbol{e}_i' = {}^m\tilde{\kappa}_{\#}\tilde{Q}_{i\#}' \qquad m = 0,1 \tag{4.25} $$

Inserting Equation (4.25) into Equations of damage initiation (4.23) and failure surface (4.24) yields

$$ {}^m\tilde{\kappa}_{\#} = \sqrt{\left(\frac{\tilde{Q}_{1\#}'^{\,2}}{{}^m\kappa_I'^2} + \frac{\tilde{Q}_{2\#}'^{\,2}}{{}^m\kappa_{II}'^2} + \frac{\tilde{Q}_{3\#}'^{\,2}}{{}^m\kappa_{III}'^2} \right)^{-1}} \qquad m = 0,1 \tag{4.26} $$

We assume that damage does not heal, i.e. the surface in the effective strain space may only expand. In the present chapter we assume that the damage surface maintains its ellipsoidal shape; the center of ellipsoidal surface remains fixed; the ellipsoid does not rotate, remains symmetric with respect to the material coordinate system, but may expand nonuniformly along its three material axes.

To satisfy the Kuhn-Tucker condition, the maximum damage surface must be defined and stored and compared with the value of the current damage surface. Let ${}^d\kappa_I', {}^d\kappa_{II}', {}^d\kappa_{III}'$ be the three radii of the current damage surface in the MCS as shown in Figure 4.2. Initially, the damage surface coincides with the initial damage surface, ${}^0\kappa_I', {}^0\kappa_{II}', {}^0\kappa_{III}'$.

At each increment, we compute the trial effective strain in the DCS, denoted by $\tilde{\kappa}_I^{tr}, \tilde{\kappa}_{II}^{tr}, \tilde{\kappa}_{III}^{tr}$ and the corresponding principal axes $\tilde{\boldsymbol{e}}_1, \tilde{\boldsymbol{e}}_2, \tilde{\boldsymbol{e}}_3$. If there is at least one effective strain vector, $\tilde{\kappa}_*^{tr}\tilde{\boldsymbol{e}}_*$, that falls outside the current damage surface (see Figure 4.2), i.e.

$$ \frac{{}^*x_1'^2}{{}^d\kappa_I'^2} + \frac{{}^*x_2'^2}{{}^d\kappa_{II}'^2} + \frac{{}^*x_3'^2}{{}^d\kappa_{III}'^2} > 1 \quad \exists * \tag{4.27} $$

where

$$\begin{aligned} {}^{*}x_i' &= \tilde{\kappa}_* \tilde{\boldsymbol{e}}_* \cdot \boldsymbol{e}_i' = \tilde{\kappa}_* \tilde{Q}_{i*}' \\ \tilde{\kappa}_*^{tr} &= \tilde{\kappa}_* \end{aligned} \tag{4.28}$$

then the process is inelastic and it is necessary to evolve the damage surface.

On the other hand, the process is considered to be elastic, if all the three trial effective strain vectors are inside the current damage surface, i.e.

$$\begin{aligned} &\frac{{}^{\#}x_1'^2}{{}^{d}\kappa_I'^2} + \frac{{}^{\#}x_2'^2}{{}^{d}\kappa_{II}'^2} + \frac{{}^{\#}x_3'^2}{{}^{d}\kappa_{III}'^2} < 1 \quad \forall \# = 1,2,3 \\ &{}^{\#}x_i' = \tilde{\kappa}_{\#}^{tr} \tilde{\boldsymbol{e}}_{\#} \cdot \boldsymbol{e}_i' = \tilde{\kappa}_{\#}^{tr} \tilde{Q}_{i\#}' \end{aligned} \tag{4.29}$$

In the case of elastic process, the damage surface remains unchanged.

There are a number of possibilities to evolve the damage surface. In principal, one would like to modify (expand) the current damage surface as little as possible provided that the damage surface is convex and that the trial effective strain that falls outside the existing damage surface (4.27) be returned to the new damage surface. This somewhat loose requirement may create complex surfaces that would necessitate numerous state variables to track its shape and position. One could impose a restriction that the yield surface remains ellipsoid that may expand, rotate and move in the strain space. One may further constrain the motion of the centroid and even restrain it from rotation limiting it to expansion only. This latter variant, which has been adopted in the present chapter, represents a reasonable compromise between the computational efficiency and model complexity. With this approach, the new radii of the current damage surface ${}^{d}\kappa_I', {}^{d}\kappa_{II}', {}^{d}\kappa_{III}'$ are rescaled by a factor of $s_* \geq 1$ for every $\tilde{\kappa}_* \tilde{\boldsymbol{e}}_*$ as follows

$$\begin{aligned} {}^{d}\kappa_{\#}' &:= \ 1 + s_* \left| \tilde{Q}_{\#*}' \right| \ {}^{d}\kappa_{\#}' \\ \tilde{Q}_{\#*}' &= \tilde{\boldsymbol{e}}_* \cdot \boldsymbol{e}_{\#}' \end{aligned} \tag{4.30}$$

where the scaling parameter is found from solving the nonlinear equation

$$f \ \ s \ = \frac{{}^{*}x_1'^2}{{}^{d}\kappa_I'^2} + \frac{{}^{*}x_2'^2}{{}^{d}\kappa_{II}'^2} + \frac{{}^{*}x_3'^2}{{}^{d}\kappa_{III}'^2} - 1 = 0 \rightarrow s_* \tag{4.31}$$

Note that when $\hat{\boldsymbol{e}}_*$ coincides with one of the material coordinate axes, say $\boldsymbol{e}'_i$, then only one axis ${}^{d}\kappa'_*$ of an ellipsoid is rescaled by $1 + s_*$. The Newton method is used to solve the nonlinear Equation (4.31) with an initial guess of $s_* = 0$. The above process is repeated for every $\hat{\kappa}_* \hat{\boldsymbol{e}}_*$ with the three ellipsoid radii obtained from the previous update.

Let ${}^{d}\kappa'_{I}, {}^{d}\kappa'_{II}, {}^{d}\kappa'_{III}$ be the final radii of the damage surface and $\tilde{\boldsymbol{e}}_1, \tilde{\boldsymbol{e}}_2, \tilde{\boldsymbol{e}}_3$ be the current principal directions of the effective strain. The corresponding principal effective strains $\tilde{\kappa}_I, \tilde{\kappa}_{II}, \tilde{\kappa}_{III}$ that lie on the current damage surface follow from

$$\tilde{\kappa}_{\#} = \sqrt{\left(\frac{\tilde{Q}'_{1\#}{}^{2}}{{}^{d}\kappa'^{2}_{I}} + \frac{\tilde{Q}'_{2\#}{}^{2}}{{}^{d}\kappa'^{2}_{II}} + \frac{\tilde{Q}'_{3\#}{}^{2}}{{}^{d}\kappa'^{2}_{III}} \right)^{-1}} \tag{4.32}$$

Given the principal effective strains $\tilde{\kappa}_I, \tilde{\kappa}_{II}, \tilde{\kappa}_{III}$ obtained from Equation (4.32), the damage state variables $w_{\#} = G\ \tilde{\kappa}_{\#}$ follow from Equations (4.19) and (4.20). Note that once the damage surface encompasses the failure surface fully, ${}^{d}\kappa'_{\#} \geq {}^{1}\kappa'_{\#},\ \forall \#$, the value of all damage parameters becomes $w_{\#} = 1$ and the damage tensor $W_{ijkl} = 0$. Consequently, $\tilde{\boldsymbol{\mathcal{L}}}_{ijmn} = 0$, and material loses its load bearing capacity at a corresponding macro-element quadrature point and there is no longer need to track the evolution of the damage surface. Remedies to dealing with softening phenomena and complete loss of load bearing capacity are discussed in Section 4.3.

Given elastic material properties L_{ijkl} and weights D'_{ij}, the current strain ε_{kl} in the GCS and the current damage surface ${}^{d}\kappa'_{I}, {}^{d}\kappa'_{II}, {}^{d}\kappa'_{III}$ defined in the MCS, the stress update algorithm is summarized in Box 4.1.

Box 4.1: Stress Update procedure for an orthotropic damage model

1. Transform the strain from GCS to MCS using $\varepsilon'_{ij} = Q'_{ki} Q'_{kj} \varepsilon_{kl}$
2. Compute the effective strain κ'_{ij} in the MCS using Equation (4.17)
3. Given κ'_{ij} solve the eigenvalue problem for the principal directions $\hat{\boldsymbol{e}}_i$ and the principal effective strains, referred to as trial effective strain $\tilde{\kappa}_I^{tr}, \tilde{\kappa}_{II}^{tr}, \tilde{\kappa}_{III}^{tr}$
4. Check if the process is elastic (4.29)
5. If the process is elastic the damage tensor W_{ijkl} remains unchanged. Go to 7 to update the stress
6. For inelastic process perform the following:
    - For each effective strain vector, $\tilde{\kappa}_*^{tr}\tilde{\boldsymbol{e}}_*$, that is outside the current damage surface compute the scaling factor $s_* \geq 1$ by solving Equation (4.31)
    - Update the radii of the damage surface ${}^d\kappa'_I, {}^d\kappa'_{II}, {}^d\kappa'_{III}$ using Equation (4.30)
    - Compute the principal effective strains using equation (4.32)
    - Calculate the damage state variables $w_\# = G\ \tilde{\kappa}_\#$ using Equations (4.19) and (4.20)
    - Update the damage tensor using Equation (4.13)

$\hat{\sigma}_{ij}$

<u>Remark 2</u>: If we force the damage surface to be a sphere at all times with a sphere radius equal to the maximum principal effective strain, ${}^d\kappa_I$, the damage model reduces to the classical isotropic damage model. For alternative definitions of the damage sphere radius see [214, 219].

4.3 The unified regularization scheme

One of the major shortcomings of continuum damage theories is their pathological sensitivity to the mesh size. This is because failure naturally tends to localize to a characteristic volume that is typically much smaller than the component (macro) scale. From the mathematical point of view, initially elliptic equations in the quasi-static loading conditions become hyperbolic. In dynamics, the initial hyperbolic equations become elliptic and the wave speed becomes imaginary. For rate independent strain softening materials, remedies range from nonlocal theories to rescaling of damage mechanics constitutive laws. An outstanding treatise of the two techniques can be found in chapters 8 and 13 of the Bazant and Planas textbook [216] and numerous references therein. In this section we show that essentially the two formulations give rise to similar results provided that they are driven by the same quantity – so called *effective softening strain* to be subsequently defined.

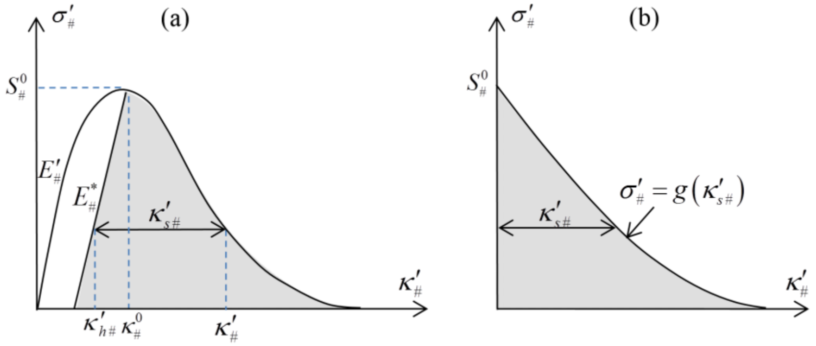

Figure 4.3 (a) Effective stress-strain relation with definition of unloading and softening branches. (b) Effective stress-softening strain curve corresponding to the effective stress-strain curve in (a). $E^*_{\#}$ is unloading modulus.

Consider a stress-strain relation in the MCS that exhibits softening behavior as shown in Figure 4.3(a).

$$\sigma'_{\#} = f \;\; \kappa'_{\#} \tag{4.33}$$

where the right subscript # = 1, 2, 3 denotes the three axes in the MCS.

The *effective softening strain*, denoted hereafter by $\kappa'_{s\#}$, is measured from the unloading branch emanating from the peak stress $S^0_{\#}$ to the softening branch as shown in Figure 4.3(b). $\kappa^0_{\#}$ is the effective strain corresponding to the maximum stress $S^0_{\#}$.

The shaded area under the $\sigma'_{\#} - \kappa'_{\#}$ curve in Figure 4.3(a), which is identical to the area under the $\sigma'_{\#} - \kappa'_{s\#}$ curve in Figure 4.3(b), is the portion of internal work required to fully damage a unit material volume from its initial (possibly) damaged state corresponding to peak stress.

It is convenient to decompose the effective strain in the MCS $\kappa'_{\#}$ into softening branch of the strain $\kappa'_{s\#}$ and the hardening branch of the strain denoted by $\kappa'_{h\#}$

$$\kappa'_{s\#} = \kappa'_{\#} - \kappa'_{h\#} \tag{4.34}$$

The hardening part of the effective strain is defined as:

$$\kappa'_{u\#} = \begin{cases} \kappa^0_{\#} - \dfrac{1}{E^*_{\#}} \; S^0_{\#} - f \;\; \kappa'_{\#} & \text{for} \quad \kappa'_{\#} > \kappa^0_{\#} \\ \kappa'_{\#} & \text{for} \quad \kappa'_{\#} \le \kappa^0_{\#} \end{cases} \tag{4.35}$$

Given $\kappa'_{\#} > \kappa^0_{\#}$, we can compute $f \;\; \kappa'_{\#}$ from Equation (4.33) and $\kappa'_{s\#}$ from Equation (4.34) which uniquely defines the softening branch of stress as a function of softening strain

$$\sigma'_{\#} = g \;\; \kappa'_{s\#} \tag{4.36}$$

In the local approach considered in the previous section, the damage parameters that drive the evolution of failure can be expressed in terms of effective strain in the MCS as

$$w'_{\#} = G \;\; \kappa'_{h\#} + \kappa'_{\mathrm{s}\#} \tag{4.37}$$

We would like to adopt the local approach as long as the equations remain elliptic, i.e. there is no softening response, i.e. $\kappa'_{\#} \le \kappa^0_{\#}$. At the onset softening response, we would like to introduce regularization only into softening strain branch using either *staggered nonlocal* approach (Section 4.3.1) or *constitutive law rescaling* approach (Section 4.3.2) as follows

$$\begin{array}{ll} \text{nonlocal staggered:} & w'_{\#} = G\ \ \kappa'_{h\#} + \left\langle \kappa'_{s\#} \right\rangle_R \\ \text{rescaling:} & w'_{\#} = G\ \ \kappa'_{h\#} + \left] \kappa'_{s\#} \right[_{R/h^e} \end{array} \tag{4.38}$$

where $\left\langle \bullet \right\rangle_R$ and $\left] \bullet \right[_{R/h^e}$ are staggered nonlocal and rescaling operators described in the next section; R denotes the interaction radius assumed to be an intrinsic material parameter in the nonlocal theories; h^e is a characteristic size of an element.

The two operators introduce regularization that allows to match a certain observed physical phenomenon irrespective of mesh density. The nonlocal operator is aimed at forcing the discrete (finite element) model to match the observed localization width. The rescaling operator, on the other hand, forces the discrete model to be consistent with the fracture mechanics approach.

4.3.1 Staggered nonlocal operator

In the nonlocal model, the nonlocal field $\mathcal{N}\ \ \phi(\boldsymbol{x})\ \ _R$ of a function $\phi(\boldsymbol{x})$ is computed as a weighted average in a spatial neighborhood V

$$\mathcal{N}\ \ \phi(\boldsymbol{x})\ \ _R = \int_V \alpha'(\boldsymbol{x}, \boldsymbol{\xi}) \phi(\boldsymbol{x}) d\boldsymbol{\xi} \tag{4.39}$$

where neglecting the boundary effects, the kernel function $\alpha'(\boldsymbol{x}, \boldsymbol{\xi})$ is defined as

$$\alpha'(\boldsymbol{x}, \boldsymbol{\xi}) = \frac{\alpha\ \ \left|\boldsymbol{x} - \boldsymbol{\xi}\right|}{\int_V \alpha\ \ \left|\boldsymbol{x} - \boldsymbol{\xi}\right|\ d\boldsymbol{\xi}} \tag{4.40}$$

In Equation (4.40), $\alpha\ \ r$ is a monotonically decreasing nonnegative function of the distance $r = \left|\boldsymbol{x} - \boldsymbol{\xi}\right|$, typically described by a Gauss or bell-shaped function. Here, the following bell-shaped weight function

$$\alpha(r) = \begin{cases} \left(1 - \dfrac{r^2}{R^2}\right)^2 & \text{if} \quad 0 \le r \le R \\ 0 & \text{if} \quad r \ge R \end{cases} \tag{4.41}$$

is employed due to its simplicity.

For computational convenience it is convenient to exploit the information at the element quadrature point and thus approximate Equations (4.39) and (4.40) by

$$\begin{aligned} \boldsymbol{\mathcal{N}}\ \ \phi(\boldsymbol{x}_I)\ _R &= \sum_{\boldsymbol{\xi}_J \in Q_I} \alpha * (\boldsymbol{x}_I, \boldsymbol{\xi}_J) \phi(\boldsymbol{\xi}_J) \\ \alpha * (\boldsymbol{x}_I, \boldsymbol{\xi}_J) &= \frac{\alpha(\boldsymbol{x}_I, \boldsymbol{\xi}_J)}{\sum_{\boldsymbol{\xi}_J \in Q_I} \alpha(\boldsymbol{x}_I, \boldsymbol{\xi}_J)} \end{aligned} \tag{4.42}$$

where $\boldsymbol{x}_I$ denotes the position of the quadrature point *I*; Q_I is a set of quadrature points $\boldsymbol{\xi}_J \in Q_I$ adjacent to point $\boldsymbol{x}_I$

$$Q_I \left| \left| \boldsymbol{x}_I - \boldsymbol{\xi}_J \right| \leq R, \forall \boldsymbol{\xi}_J \in Q_I \right. \tag{4.43}$$

where the Q_I adjacency information for each quadrature point is precomputed in the preprocessing stage. In the staggered nonlocal algorithm [73], the staggered nonlocal operator $\left\langle \phi(\boldsymbol{x}_I) \right\rangle$ is defined as

$$\begin{aligned} \left\langle \phi(\boldsymbol{x}_I) \right\rangle_R &= \sum_{\boldsymbol{\xi}_J \in Q_I} \alpha^*(\boldsymbol{x}_I, \boldsymbol{\xi}_J) \phi^*(\boldsymbol{\xi}_J) \\ \phi^*(\boldsymbol{\xi}_J) &= \begin{cases} {}^{i+1}_{n+1}\phi(\boldsymbol{\xi}_I) & \text{if } \boldsymbol{\xi}_J = \boldsymbol{x}_I \\ {}_{n}\phi(\boldsymbol{\xi}_J) & \text{if } \boldsymbol{\xi}_J \neq \boldsymbol{x}_I \end{cases} \end{aligned} \tag{4.44}$$

where the left subscript denotes the load increment and the left superscript denotes the iteration count. ${}_{n}\phi$ denotes converged local field taken from the previous increment, and ${}^{i+1}_{n+1}\phi$ is a local field at the current load increment n+1 and the current iteration i+1. The salient feature of the staggered nonlocal operator $\left\langle \phi(\boldsymbol{x}_I) \right\rangle_R$ is that the adjacent information is taken from the previous converged solution.

Given the effective softening strain $\kappa'_{\mathrm{s}\#}\ \ \boldsymbol{x}_I$ at various quadrature points and assuming that all quadrature points in Q_I ($\boldsymbol{\xi}_J \in Q_I$) have the same MCS, the nonlocal staggered effective softening strain is computed as

$$\begin{aligned}\left\langle \kappa'_{\mathrm{s}\#}(\boldsymbol{x}_I)\right\rangle_R &= \sum_{\boldsymbol{\xi}_J \in Q_I} \alpha^{*}(\boldsymbol{x}_I, \boldsymbol{\xi}_J)\kappa'^{*}_{s\#}(\boldsymbol{\xi}_J) \\ \kappa'^{*}_{s\#}(\boldsymbol{\xi}_J) &= \begin{cases} {}^{i+1}_{n+1}\kappa'_{\mathrm{s}\#}(\boldsymbol{\xi}_I) & \mathit{if}\ \boldsymbol{\xi}_J = \boldsymbol{x}_I \\ {}_{n}\kappa'_{\mathrm{s}\#}(\boldsymbol{\xi}_J) & \mathit{if}\ \boldsymbol{\xi}_J \neq \boldsymbol{x}_I \end{cases}\end{aligned} \tag{4.45}$$

4.3.2 Constitutive law rescaling operator

Consider a discrete finite element model, with a characteristic element volume denoted by Ω^e. We define the so-called post-peak fracture energy G_c, which is the amount of post-peak energy removed from the finite element mesh $\int_0^{\infty} g\ \ \kappa'^{e}_{s\#}\ \ d\kappa'^{e}_{s\#}\ \Omega^e$ divided by the new surface area A_e introduced

$$\left(\int_0^{\infty} g\ \ \kappa'^{e}_{s\#}\ \ d\kappa'^{e}_{s\#}\ \Omega^e\right)\Big/A^e = G_c \tag{4.46}$$

where $\kappa'^{e}_{s\#}$ is an effective softening strain in an element *e* and $g\ \ \kappa'^{e}_{s\#}$ has been defined in Equation (4.36).

In explicit finite element codes, when the material in all quadrature points of an element fails completely, i.e., stress reduces to zero due to softening, the element is removed from the mesh due to stability. On the other hand, in implicit finite element codes, the failed element is most often left to preserve element connectivity. Whether the element is removed or not is a matter of computational convenience, but de facto it effectively no longer exists, and its absence introduces a new free surface, A_e. While the exact free surface area A_e created by element erosion depends on the element geometry and fracture pattern, it is convenient to introduce an approximation, $\Omega_e\ /\ S_e \approx \sqrt[3]{\Omega_e} \equiv h_e$, and thus simplify Equation (4.46) as

$$\int_0^{\infty} g^e\ \ \kappa'^{e}_{s\#}\ \ d\kappa'^{e}_{s\#}\ h^e = G_c \tag{4.47}$$

Note that the condition in Equation (4.47) should be valid for any element size. This implies that the function $g^{e} \;\; \kappa'^{e}_{s\#}$ should be element size dependent.

The fracture energy (toughness) G_c is material constant that can be obtained from either an experiment or from simulation in a uniform finite element mesh where the mesh size is equal to the characteristic size of the material, h_c. The resulting fracture energy is

$$G_c = \int_0^{\infty} g \;\; \kappa'_{s\#} \;\; d\kappa'_{s\#} \; h_c \tag{4.48}$$

Equating Equations (4.47) and (4.48) yields

$$\int_0^{\infty} g^{e} \;\; \kappa'^{e}_{s\#} \; \left(\frac{h^{e}}{h_c}\right) d\kappa'^{e}_{s\#} = \int_0^{\infty} g \;\; \kappa'_{s\#} \;\; d\kappa'_{s\#} \tag{4.49}$$

A trivial solution that satisfies Equation (4.49) is

$$\kappa'^{e}_{s\#} = \frac{h_c}{h^{e}} \kappa'_{s\#} \tag{4.50}$$

which yields

$$g^{e} \;\; \kappa'^{e}_{s\#} \;\; = g\left(\frac{h_c}{h^{e}} \kappa'_{s\#}\right) \tag{4.51}$$

Note that in practice, however, the characteristic length h_c may be considerably smaller than a structural component size, and therefore a uniform finite element mesh with h_c as a mesh size might be computationally prohibitive. Instead, one may choose a coarser mesh size $h^{r} > h_c$ as a reference mesh and find (or calibrate) a $g \;\; \kappa'_{s\#}$ that will reproduce experimental data in terms of the crack length. Then the rescaling process will be similar to Equations (4.50) and (4.51)

$$\kappa'^{e}_{s\#} = \frac{h^{r}}{h^{e}} \kappa'_{s\#} \qquad g^{e} \;\; \kappa'^{e}_{s\#} \;\; = g\left(\frac{h^{r}}{h^{e}} \kappa'_{s\#}\right) \tag{4.52}$$

Equation (4.52) suggests that one can utilize the constitutive law ($g\ \ \kappa'_{s\#}$, $f\ \ \kappa'_{\#}$ and $G\ \ \kappa'_{\#}$), calibrated based on the reference mesh h^r to compute the constitutive law corresponding to arbitrary element size h^e by recalling the effective softening strain based on Equation (4.52). The resulting damage parameter can be computed as

$$\begin{aligned} w'_{\#} &= G\ \ \kappa'_{h\#} + \left]\kappa'_{s\#}\right[_{h^r/h^e} \\ \left]\kappa'_{s\#}\right[_{h^r/h^e} &= \frac{h^r}{h^e}\kappa'_{s\#} \end{aligned} \tag{4.53}$$

4.4 Numerical results

4.4.1 Edge-cracked plate under impulsive loading

The experiments of edge-cracked plate subjected to a high rate shear impact loading as shown in Figure 4.4 were conducted by Kalthoff and Winkler [220]. Two different failure modes were observed by modifying the projectile speed v_0. At high impact velocities ($v_0 = 70$ m/s), a shear band is observed to emanate from the notch at an angle of -10° with respect to the initial notch. At lower strain rate ($v_0 = 33$ m/s), brittle failure with a crack propagation angle of about 70° is observed, as shown in Figure 4.5. In this chapter, only the brittle fracture mode was studied.

Due to symmetry, only the upper half of the plate is modeled. The boundary conditions are applied at the bottom edge of the finite element model, $u_y = 0$ and $t_x = 0$. The lower part of the specimen is subjected to an impulse load along the horizontal direction, which is modeled as a prescribed velocity:

$$v(t) = \begin{cases} \dfrac{v_0 t}{t_{ramp}} & t_{ramp} \geq t \\ v_0 & \text{otherwise} \end{cases} \tag{4.54}$$

where $v_0 = 16.5\,\mathrm{m/s}$ and $t_{ramp} = 1 \times 10^{-7}\,\mathrm{m/s}$. The material is a steel 18Ni1900 and its material properties are: $\rho = 8000\,\mathrm{kg/m^3}$, $E = 190\,\mathrm{GPa}$ and $\upsilon = 0.30$.

The plate is modeled using orthotropic damage constitutive model described in Section 4.2, with material constants: $G_f = 2.213 \times 10^4$ N/m, $\varepsilon_0 = 4.44 \times 10^{-3}$ m and shear correction factor of 1. The effective strain was calculated based on in-plane principal strains. The model has been implemented in VUMAT of ABAQUS/Explicit. The characteristic length of the staggered nonlocal method is chosen to be 0.003m. Simulations were made with four structured meshes 25×25, 50×50, 100×100 and 200×200 and two unstructured meshes. Elements in the mesh were eroded once the effective strain reached 95% of the fully damaged state. The comparison results using rescaling and staggered nonlocal methods are shown in Figure 4.6.

It can be seen that the two methods show little dependency on mesh size and perform quite well in predicting the crack speed and crack path. The average angle of crack for the two methods was as follows: 69.8° for the rescaling method and 65.2° for staggered nonlocal method. In comparison, the average angle predicted by XFEM in [221] was 60.7°. The crack path obtained from the rescaling model is the closest to the experimental result even though the crack path is not smooth. In addition, the CPU time of the rescaling method is significantly lower than using the staggered nonlocal approach.

Figure 4.6(c) shows the crack propagation path for the rescaling method (two figures on the left) and the staggered nonlocal method (two figures on the right) for unstructured mesh with equivalent mesh densities corresponding to 100×100 and 200×200 meshes, respectively. It can be seen that both methods predicts the crack path quit well.

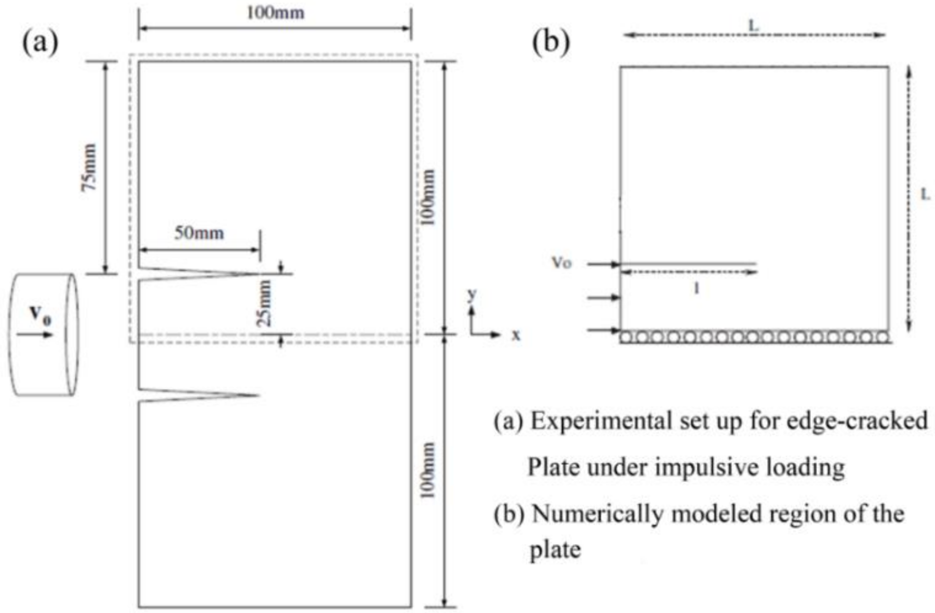

Figure 4.4 Experimental setup and numerically modeled region for the edge-cracked plate under impulsive loading

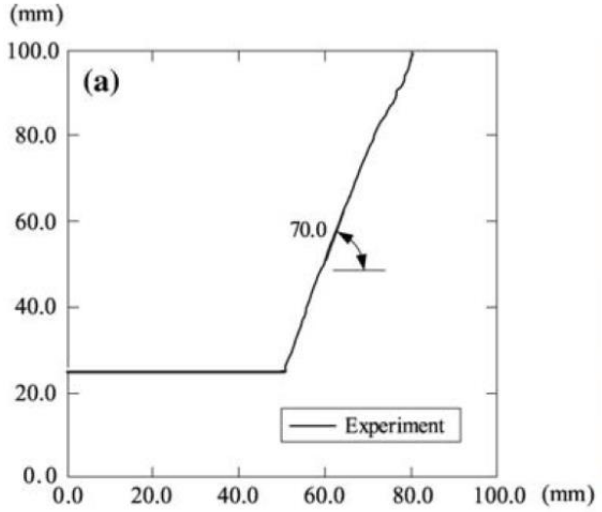

Figure 4.5 The experimental crack path reported by Kalthoff and Winkler [220]

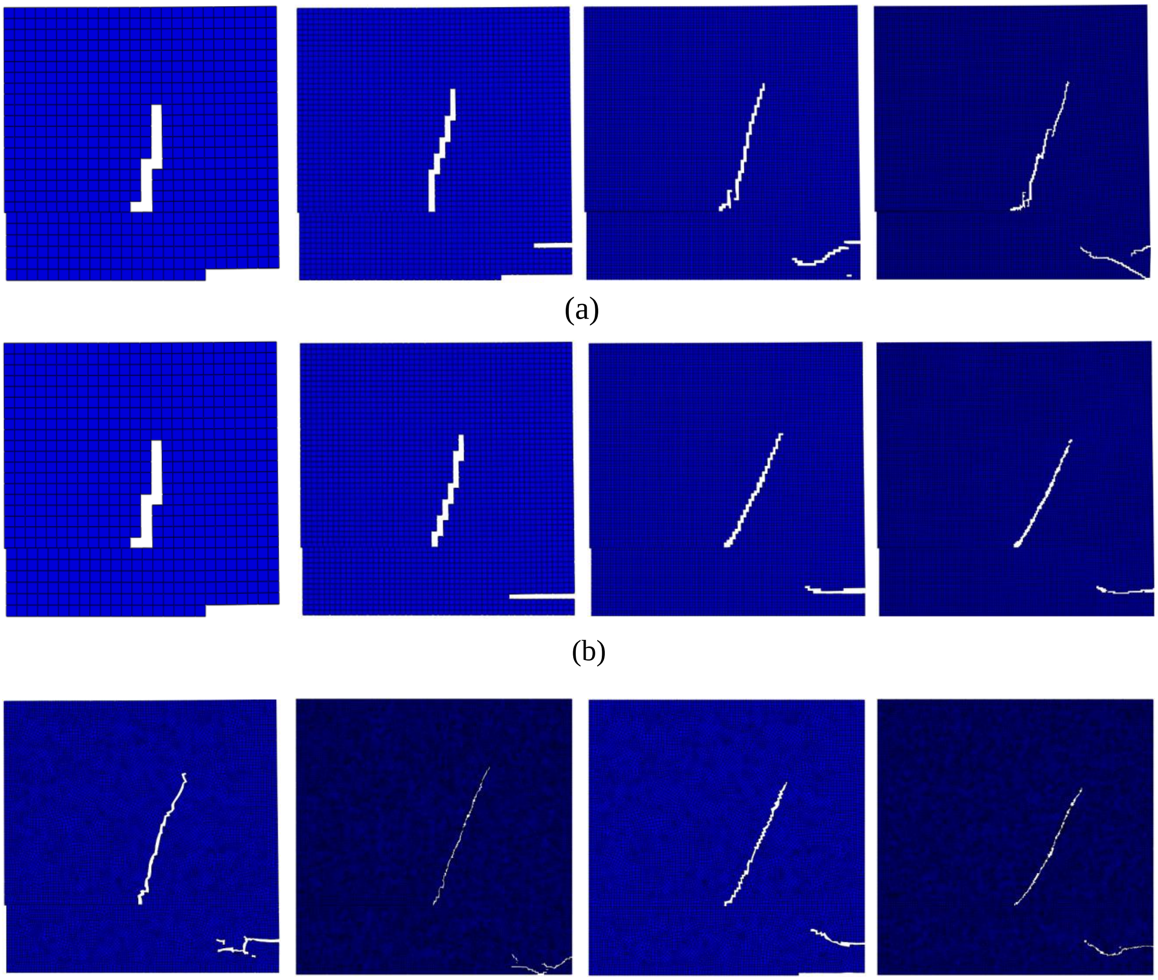
(a)

(b)

(c)

Figure 4.6 Comparison results for the edge-cracked plate problem for: (a) rescaling method, (b) staggered nonlocal method for structured meshes 25×25, 50×50, 100×100 and 200×200 and (c) unstructured meshes ($h^{e}_{avg} = 1.0 \text{ mm and } 2.0 \text{ mm}$) with characteristic length 3 mm

4.4.2 Four-point bending test

In the second example we study a four-point bending of a steel wire reinforced cement beam. The experiments were conducted by Jiang *et al*. [222]. Simulations with a considerably large characteristic length were conducted in [73]. The dimensions of the beam and loading configuration are illustrated in Figure 4.7. The schematics of the fiber distribution along the beam is shown is Figure 4.8.

Three finite element meshes of the beam considered in the present study are shown in Figure 4.9. The steel wire reinforced cement is treated as an orthotropic homogenized material. The material is modeled as an orthotropic elastic in linear regime. The damage model is assumed to be orthotropic as outlined in Section 4.2. The effective stress-strain relation as assumed to be piece-wise linear with three segments: ε_0, σ_0 are the stresses and strains at the onset of damage; ε_1, σ_1 represent the first linear segment; and $\varepsilon_2, \sigma_2 = 0$ at the fully dame state. The model parameters are summarized in Table 4.1 and Table 4.2. For the rescaling and staggered nonlocal models, the characteristic length was calibrated on the coarse mesh. It was found to be equal to 2.6 mm.

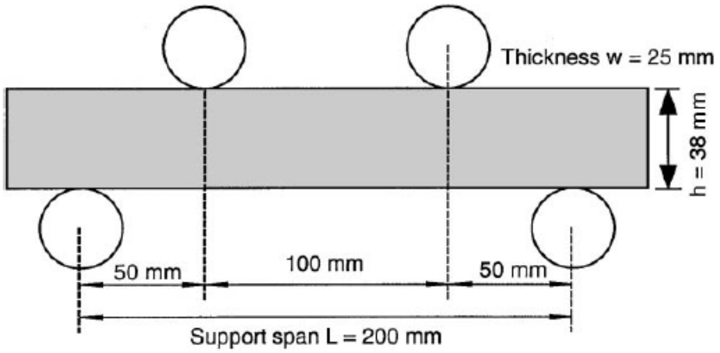

Figure 4.7 Schematics of the four-point bending test [222]

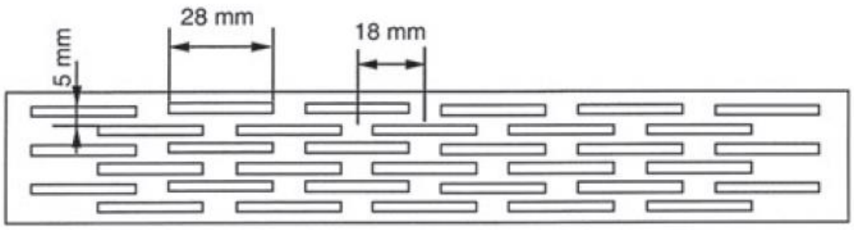

Figure 4.8 Schematics of the steel wire reinforced cement beam [222]

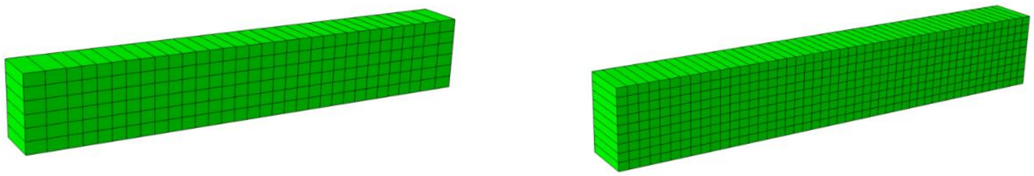

(a) mesh-1, 192 elements

(b) mesh-2, 432 elements

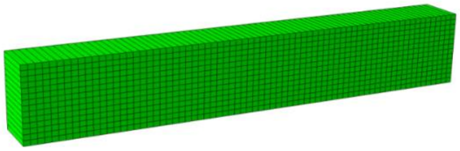

(c) mesh-3, 1008 elements

Figure 4.9 Three finite element meshes used in this study

Table 4.1 Effective linear mechanical properties

$E_{11}(GPa)$	$E_{11}(GPa)$	ν_{12}	$G_{11}(GPa)$
8.5	8.49	0.199	3.54

Table 4.2 Model parameters for the orthotropic damage model

$\sigma_0(MPa)$	$\sigma_1(MPa)$	ε_1	ε_2
6.5	2.15	0.0109	0.144

The load versus displacement curves for the four-point bending test simulations are illustrated Figure 4.10 for the rescaling and the staggered nonlocal models and compared with the experimental data. It can be seen that both the rescaling and nonlocal model are practically mesh size independent and show reasonable agreement with the test data.

Figure 4.11 and Figure 4.12 show that the failure pattern predicted by the rescaling and staggered nonlocal approaches, respectively, is in good agreement with experimental observations. It can be seen that there is little difference in the results obtained by the rescaling and staggered nonlocal approaches.

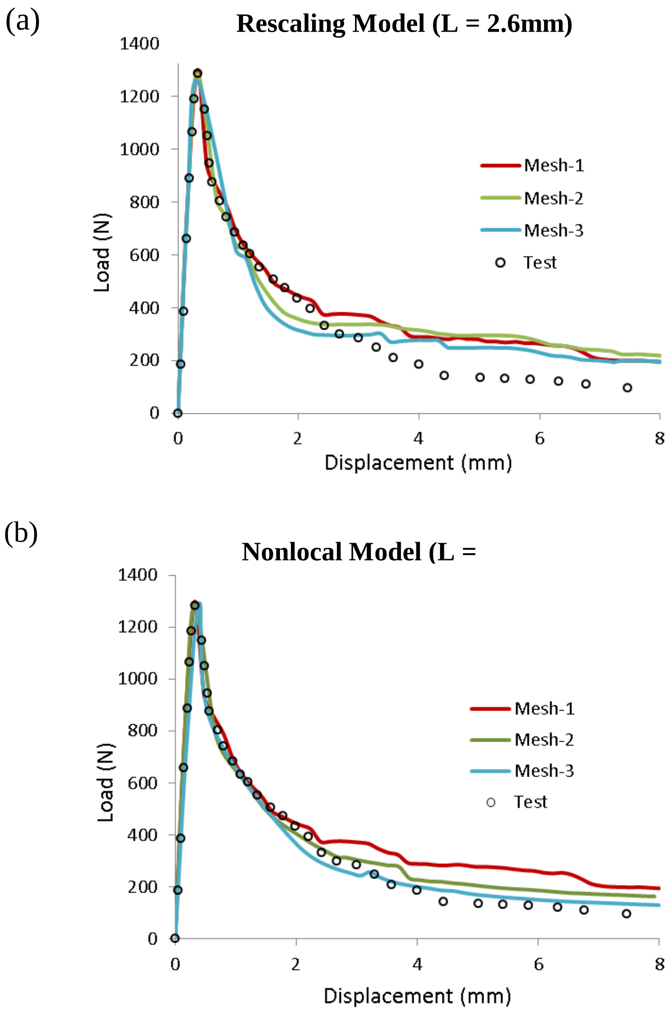

Figure 4.10 Numerical simulation results of load versus displacement for four-point bending test using rescaling and staggered nonlocal method with characteristic length of 2.6 mm.

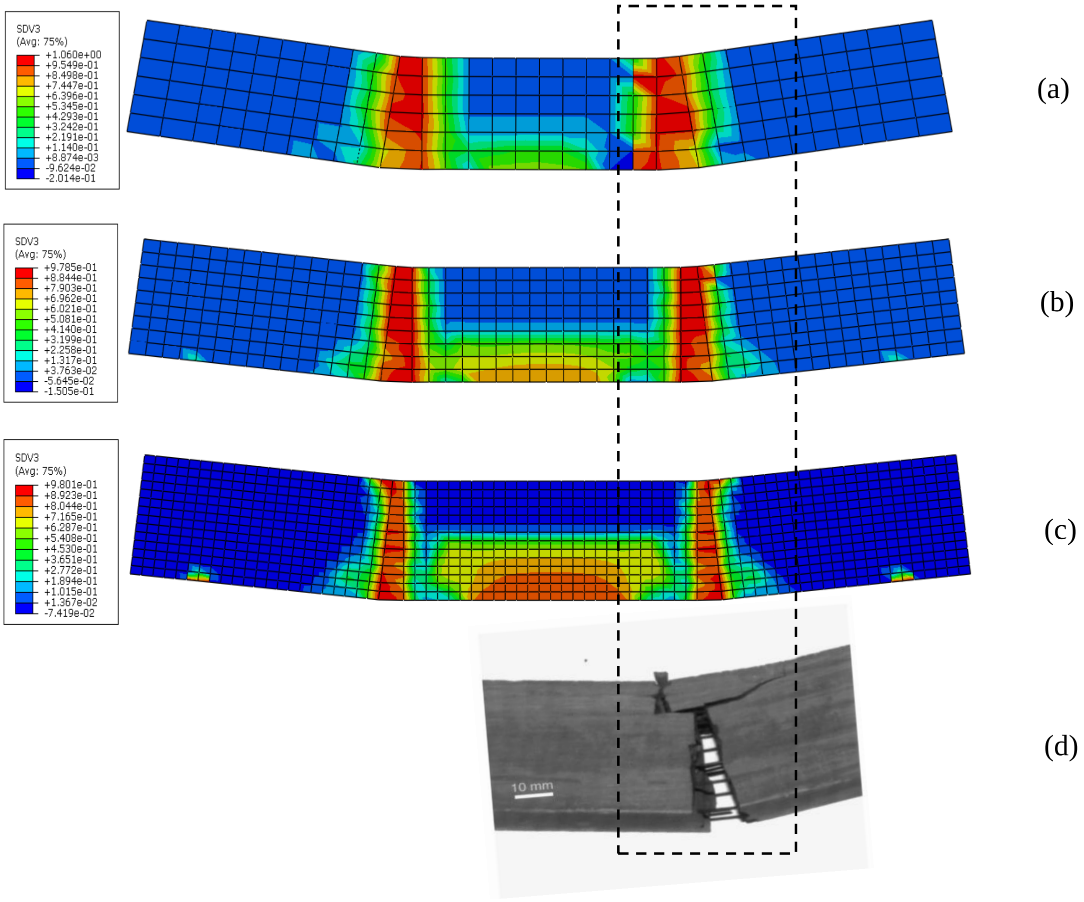

Figure 4.11 Numerical simulation results using rescaling method for (a) mesh 1; (b) mesh 2; (c) mesh 3; (c) Photographs of a broken CSS-steel-wire-reinforced cement specimen following the four-point bending test.

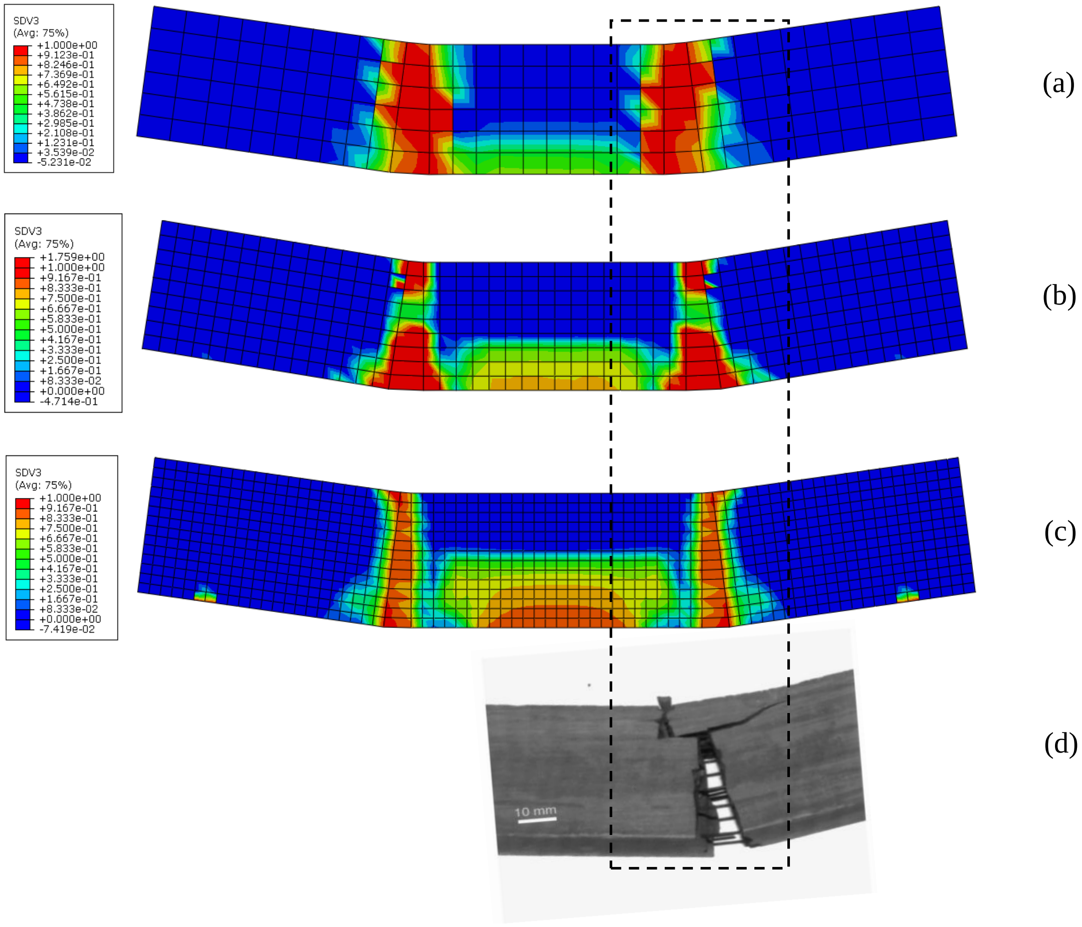

Figure 4.12 Numerical simulation results using nonlocal method for (a) mesh 1, (b) mesh 2 and (c) mesh 3; (c) Photographs of a broken CSS-steel-wire-reinforced cement specimen following the four-point bending test.

4.4.3 Single edge notch bend fracture test

For the third and final numerical example, we study mode I fracture of a two-dimensional triaxially braided carbon (2DTBC) fiber composites. The composite is modeled as orthotropic in both elastic and inelastic regimes. Figure 4.13 shows the composite architecture of a $0/\pm 45^\circ$ 2DTBC used in the present study. Eight braided composite consists of fiber mats (axial tows consisting of 80,000 fibers and biased tows consisting of 20,000 fibers) stacked together. A vinylester Ashland Hetron 922 resin is the matrix material [223]. The effective elastic mechanical properties are summarized in Table 4.3.

Mode I fracture tests are carried out by using a modified single edge notch bend (SENB) configuration. Figure 4.14 shows the configuration and dimensions of the specimen. The fracture tests are simulated by using ABAQUS through the user-defined subroutine UMAT. Figure 4.15 depicts the three finite element meshes considered in the simulation.

Figure 4.16 compares the simulation and experimental results. It can be seen that both methods predict the overall behavior quite accurately with different mesh densities. Figure 4.17 compares the failure pattern as obtained in simulations for mesh 1 and experiments.

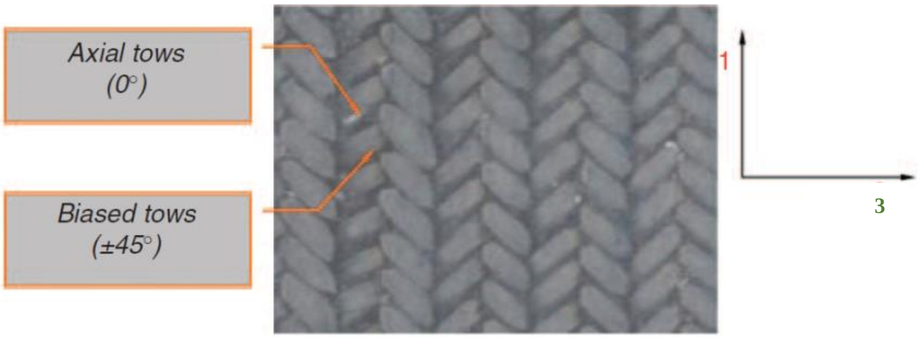

Figure 4.13 Architecture of braided composite panel [223]

Table 4.3 Effective mechanical properties

$E_{11}(GPa)$	$E_{11}(GPa)$	ν_{12}	$G_{11}(GPa)$
68.53	10.78	0.36	4.52

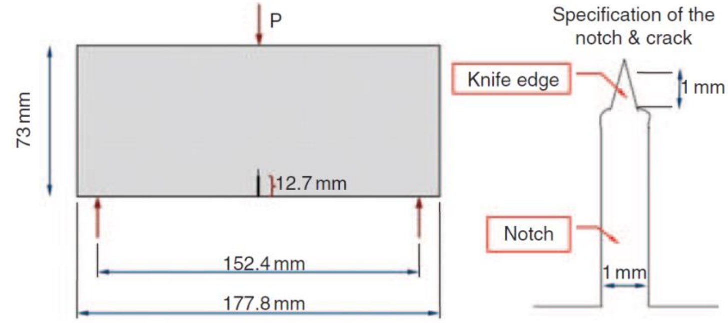

Figure 4.14 Single edge notch bend specimen (9mm) [223]

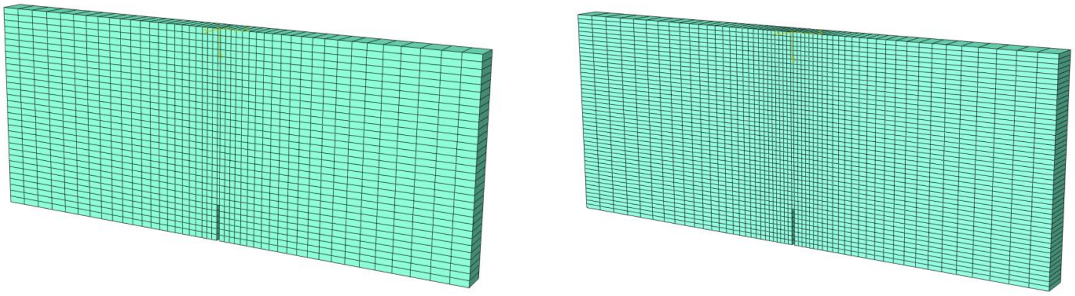

(a) mesh-1, 1434 elements

(b) mesh-2, 2632 elements

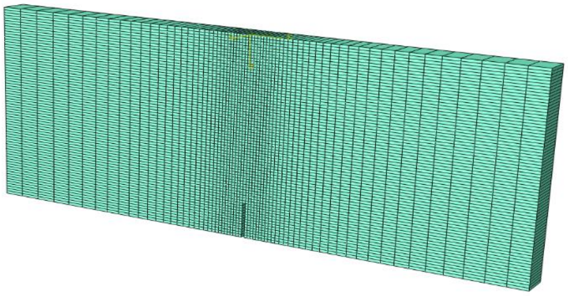

(c) mesh-3, 4732 elements

Figure 4.15 Three finite element meshes used in this study

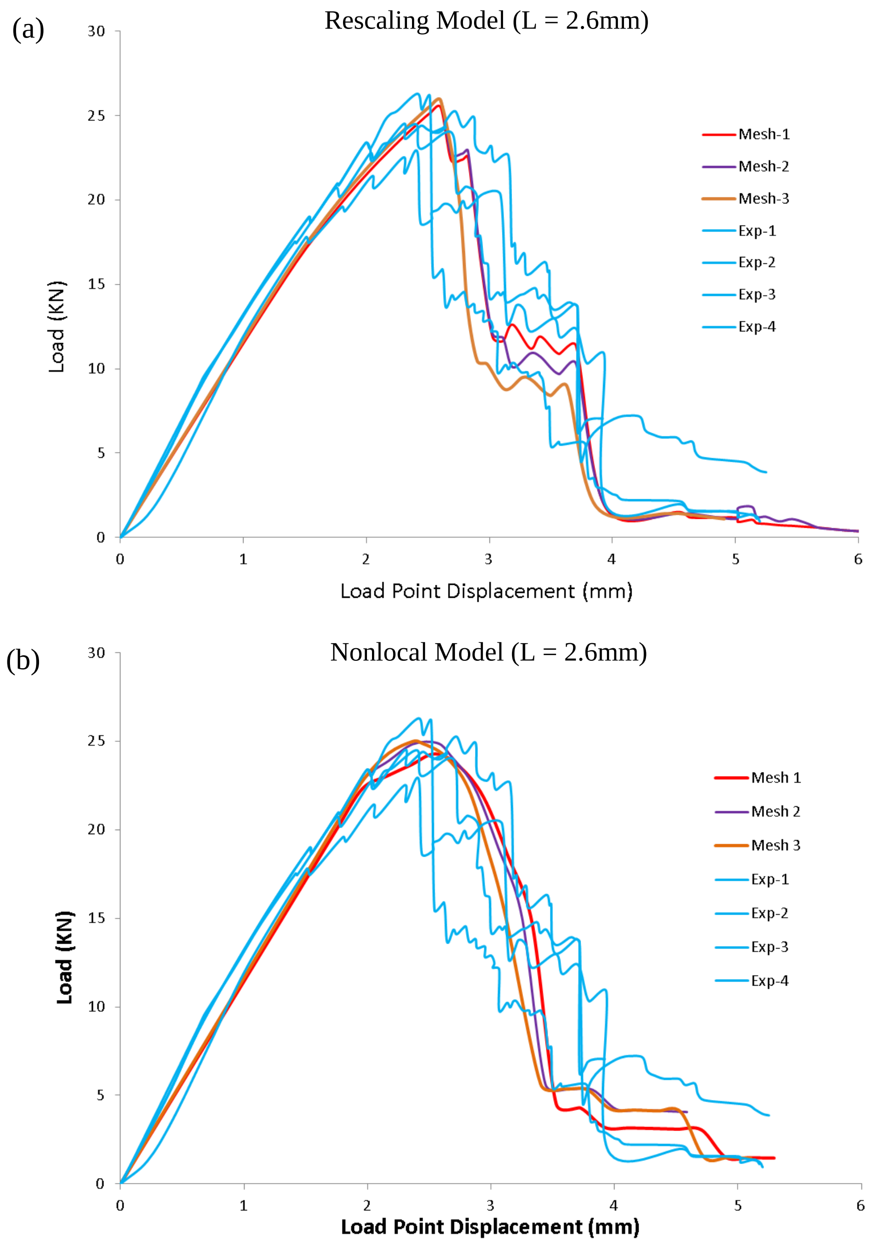

Figure 4.16 Comparison of test data and simulated results

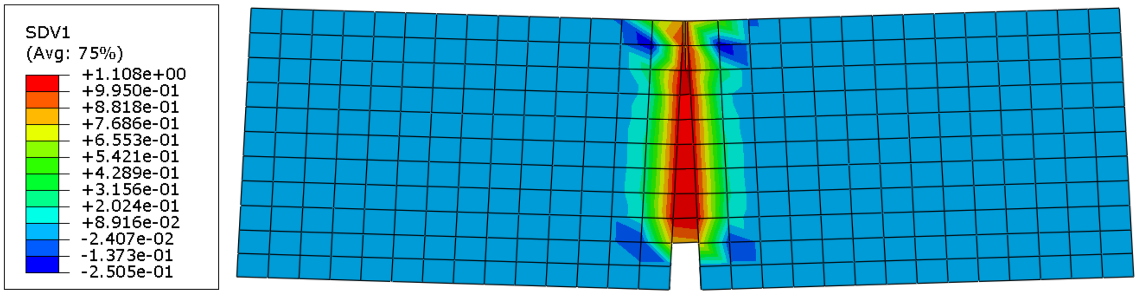

(a)

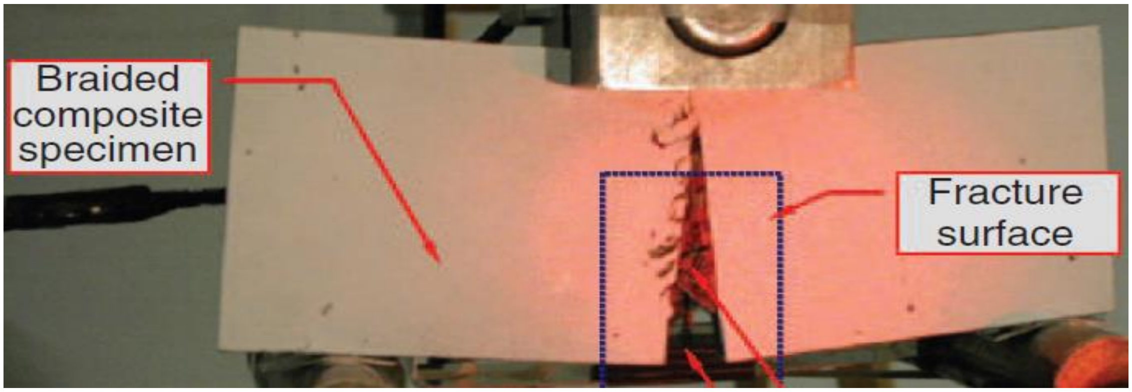

(b)

Figure 4.17 Comparison of the fracture pattern as obtained in (a) simulations for mesh 1 and (b) in the experiments

4.5 Conclusions

In this chapter, a regularized phenomenological multiscale model where elastic properties are computed using direct homogenization and subsequently evolved using a simple three-parameter orthotropic continuum damage model has been developed. A unified regularization scheme has been developed in the context of constitutive law rescaling and staggered nonlocal approaches. The method has been validated for three problems: (i) edge-cracked plate under impulsive loading, (ii) four-point bending of a steel wire reinforced cement beam, and (iii) mode I fracture of a two-dimensional triaxially braided carbon fiber composite. For all three test problems we show that: (i) the regularized phenomenological multiscale model is capable of reproducing the test data with each of the two regularization technique, and (ii) the simulation results obtained are practically mesh size independent.

The computational cost of the rescaling approach is lower than of the staggered nonlocal approach, but the crack propagation path as obtained with the staggered nonlocal approach is often smoother.

Several issues have not been addressed in the present work including:

(i) Crack propagation in meshes with large element aspect ratio. The rescaling approach might be more sensitive to the aspect ratio as it depends on the fracture surface introduced by the element deletion.

(ii) We have not studied crack problems with multiple solution branches that are energetically close to each other. Methods based on solution enrichment, such as XFEM, might be more suitable in this case.

Chapter 5

Automated Unit Cell Generation

In this chapter, a robust parametric model is presented for generating unit cells with randomly distributed inclusions. The proposed model is computationally efficient using a hierarchy of algorithms with increasing computational complexity, and is able to generate unit cells with different inclusion shapes. This chapter is reproduced from the paper co-authored with Mahesh Bailakanavar, Jacob Fish and Zheng Yuan, which was published in Engineering with Computers [224].

5.1 Introduction

Identification and generation of unit cell geometry is a vital step in the multiscale analysis of composite materials. Computational challenges in automatic generation of periodic microstructures, such as woven or fabric composites, have been by at large addressed (see for instance [225]. However, automatic generation of morphological details of materials with randomly distributed inclusions, such as defects in ceramics, hard and soft domains in polymers, chopped fiber composites, pore structures in porous and granular materials pose new challenges. Typical inclusions like ellipsoids, short fibers, platelets and discs found in heterogeneous materials are often of different shape and size. Parameters influencing the unit cell geometry are the shape and size of the inclusion, the volume fraction and the morphological details like the spatial orientation and spatial distribution of the inclusions. Statistical data about such morphological details may be obtained from X-ray tomography, and 3D image analysis. The key challenges that need to be addressed when generating the random inclusion unit cells are:

i. Accurate representation of the inclusion size and shape to minimize geometric approximation errors;
ii. Generation of unit cells with packing fraction as high as 70%, typically found in industrial grade composite materials;
iii. Determination of the unit cell size that constitutes a macroscopically homogeneous material;
iv. Generation of unit cells in quick succession with maximum computational efficiency for utilization in a stochastic multiscale framework.

A literature review points out to two main approaches being used to generate unit cells with randomly distributed inclusions namely the Concurrent Construction (CC) method [226-228] and the Random Sequential Adsorption (RSA) method [229-235]. The CC method is a two-step procedure. In the first step an initial configuration with an ordered packing of the inclusions is generated. In the second step these inclusions are perturbed in the phase space until the spatial orientation and distribution as observed in the statistical morphological data is achieved. The inclusions are not allowed to intersect or overlap as they reorient in the phase space. Duschlbauer et al. [228] used the CC method to generate short fiber composite unit cells with random orientations in 2D space. For a fiber aspect ratio (AR) of 10, they achieved a maximum of 21% fiber volume fraction without allowing any fiber intersections, which is about 75% of the maximum unforced packing limit for 2D random fibers [236].

Inclusions found in physical processes, such as burning of coal char, convective burning of porous explosives and regression of solid propellants, are often characterized by particular shapes, such as spheres, disks, spherocylinders and perforated rods. Lubachevsky and Stillinger [237] generated random packs of disks in 2D space by a concurrent construction algorithm. The inclusions start with random positions and velocities and they grow uniformly in size from a point in space to jammed disks as they move about in space. Stafford and Jackson [238] extended the Lubachevsky-Stillinger (LS) algorithm to create packs of non-spherical shapes for modeling heterogeneities in energetic materials like gun propellants.

In the RSA approach, a point in a given unit cell volume is randomly chosen and the first inclusion is placed with its center at the chosen position. Next, another point is randomly chosen from the diminished volume in the unit cell and the second inclusion is placed at this point. Likewise the process of sequentially and randomly positioning an inclusion is continued till the desired volume fraction is achieved or till the jamming limit is encountered. This method generates unit cells with non-intersecting inclusions wherein the gap between the inclusions is user-defined, typically of the order of inclusion size. The RSA algorithm have been employed for generating unit cells with various inclusions, including disks [239], spheres [240], ellipsoids [241] and spherocylinders [242]. Böhm et al. [230] modified the RSA algorithm to include user specified distance between adjacent inclusions to generate unit cells with cylindrical (AR=5) , sphero-cylindrical (AR=5) and spherical inclusions with inclusion volume fraction of 15%. Kari et al. [230] also used a modified RSA algorithm wherein the unit cells with cylindrical inclusions (AR=10) of up to a volume fraction of 25% were generated. For volume fractions greater than 25% cylindrical inclusions with decreasing aspect ratios (AR<10) were gradually added after the jamming limit. Pan et al. [235] used another variant of the modified RSA algorithm wherein a combination of straight and curved fibers (AR=20) were used to generate unit cells with fiber volume fraction of 35%.

Experimental study [243] of packing of short fibers in random orientation found that the packing fraction decreased rapidly with increasing aspect ratio of the rods. A theoretical study by Evans et al. [244] suggested that for fibers with AR>10, the fiber volume fraction should be proportional to the inverse aspect ratio, yielding a maximum fiber volume fraction of 20% for fibers with aspect ratio of 20. Likewise for fibers with aspect ratio of 20, Williams et al. [232] reported a maximum volume fraction of 22%, while Parkhouse et al. [243] reported a volume fraction of 28%. Toll [236] reported a maximum achievable volume fraction of 18.5% for unforced fiber packing. Toll suggests that forced packing of fibers governed by bending of fibers at contact points is imperative for attaining higher fiber volume fractions. It is important to note that in all these estimates, fibers were considered to be straight and nonintersecting.

Either of the methods mentioned above fails to generate unit cells with volume fractions as high as 45% found in various heterogeneous materials. A modified RSA algorithm by Pan et al. [235] can generate volume fractions of up to 35%. The algorithm is computationally expensive as it involves solving optimization problems to identify fiber intersection in 2D and 3D space. Additionally the algorithm is not robust and versatile to be implemented in a multiscale stochastic framework.

In the present chapter a parametric model for generating unit cells with randomly distributed inclusions is presented. The proposed algorithm possesses superior robustness, computationally efficiency and versatility compared to the previously developed RSA algorithms:

i. robustness: it yields unit cells with inclusion volume fraction of up to 55% for random packing and inclusion volume fraction of up to 70% for semi-random packing ;
ii. efficiency: it consists of a hierarchy of algorithms with increasing computational complexity;
iii. versatility: it generates unit cells with different inclusion shapes.

In Section 5.2 details of the proposed hierarchical RSA algorithm, hereafter to be referred to as HRSA, for various inclusions is presented. A simple algorithm to minimize the geometric approximation and mesh discretization errors is presented in Section 5.3.

5.2 Hierarchical random sequential adsorption (HRSA)

In this section a robust and computationally efficient unit cell generation algorithm for randomly distributed inclusions is presented. The two key features of the proposed HRSA algorithm are the capability to generate high packing fractions of up to 45% for inclusions with AR>10 and computational efficiency in generating unit cells in a quick succession. These two factors have not being addressed at tandem in the literature. These two objectives are accomplished by (i) forced packing aimed at achieving higher packing fractions followed by (ii) hierarchical inclusion generation strategy aimed at ensuring computational efficiency. The different levels in the HRSA algorithm are illustrated in Figure 5.1. A detailed flowchart of the HRSA algorithm is presented in Figure 5.3.

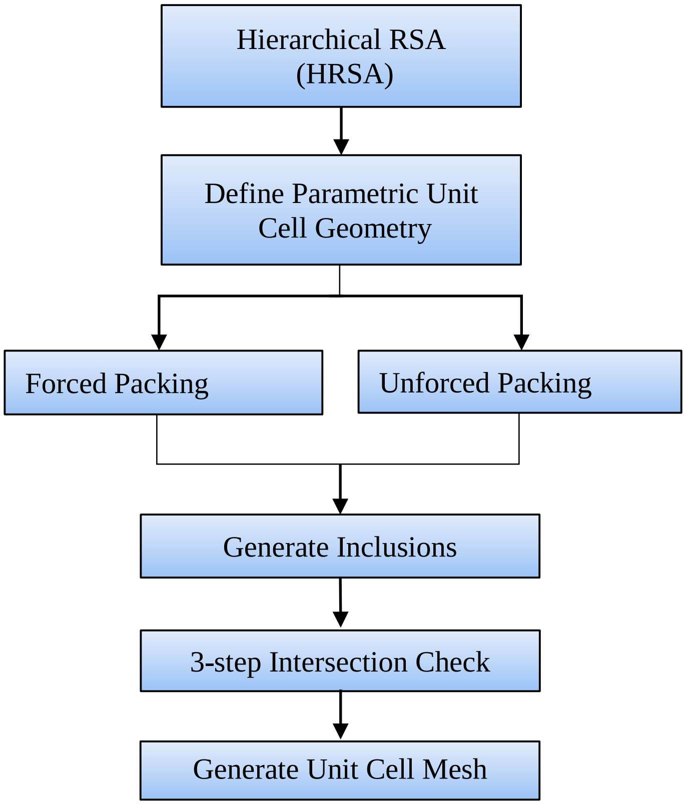

Figure 5.1 Hierarchal levels in the HRSA algorithm

5.2.1 Unit cell geometry definition

A set of independent user-defined model parameters along with dependent parameters uniquely define the unit cell geometry. The set of independent parameters is specific to the type of inclusion. The unit cell size is defined as a function of the inclusion's largest dimension. The Hierarchical Random Sequential Adsorption (HRSA) algorithm has been developed to include all possibilities of inclusion shapes found in heterogeneous materials. The size and shape of the inclusions are chosen based on the X-ray scans. Inclusions are approximated by piecewise polygons in 2D space and piecewise polyhedra in 3D space. A methodology to minimize the errors inherently introduced by approximating the geometry is built into the algorithm.

5.2.2 Random and semi-random packing

Having described the unit cell geometry, the next step in the HRSA algorithm is to develop strategies for attaining user-defined inclusion packing volume fractions. This can be achieved by unforced or forced packing. Forced packing is imperative in generating unit cells with higher packing volume fractions by either varying the size or shape of inclusions. For instance, microstructures of materials such as polyurea comprise of soft and hard domains. The hard domain comprises of inclusions of varying sizes in the form of ellipsoids. In generating such microstructures, first inclusions with highest AR are added. Once the jamming point is attained, inclusions with decreasing aspect ratios are gradually added.

For generating packs of spheres with volume fraction greater than 55%, forced packing is also accomplished by semi-random packing in which an initially ordered packing configuration with a predefined volume fraction is enforced at the beginning, i.e. an ordered packing with face-centered cubic (FCC) structure. Additional inclusions are then gradually added to fill the open spaces between FCC particles in the unit cell domain. The predefined volume fraction is determined from the user-defined target inclusion volume fraction through an empirical relation

$$\varphi_{pre} = f\ \ \varphi\ \ * \varphi; \quad f\ \ \varphi\ \ = a - b\Big/\varphi \tag{5.1}$$

where φ is the user-defined target volume fraction of inclusions, a and b are calibrated coefficients, for example, in our implementation values of a and b were chosen as 4.4 and 2.34 for $0.55 \le \varphi \le 0.60$, 3.0 and 1.5 for $0.60 \le \varphi \le 0.70$, 2.0 and 0.80 for $0.70 \le \varphi \le 0.74$, and 0 and 0.74 for $\varphi > 0.74$. A maximum inclusion volume fraction of 78% can be achieved by semi-random packing.

Microstructures with either a low inclusion aspect ratio or a low volume fraction (i.e. $\varphi \le 55\%$) obviate the necessity to forced packing. In generating such unit cells the initial ordered packing is not enforced. Given the set of independent and dependent parameters, inclusions are randomly generated and sequentially added in the unit cell domain.

5.2.3 Hierarchical inclusion generation strategy

Optimization tools have been previously used [235] to check for inclusion intersections in 3D space. In the HRSA algorithm, closed form solutions are incorporated to check for inclusion intersections in 3D space rather than optimization tools to provide increased efficiency. This step is executed after the inclusions are generated in 3D and preceded by either the forced or the unforced packing phase.

The method of separating axis serves as the main engine for checking whether or not the inclusions intersect in 3D space. However, the computational cost of this method is enormous. To reduce the computational cost, the method of separating axis is preceded by hierarchy of less costly methods, such as estimating the distance between inclusions and the method of separating planes. Consequently, very few inclusions need to be checked for intersections using the method of separating axis and somewhat large set is checked for intersections using significantly less costly method of separating planes. This results in a significant increase in the computational efficiency of the RSA algorithm. The three methods are explained in the following sections in the order of their implementation in the algorithm.

5.2.3.1 Radial distance between inclusions

This is the first method in the three-step hierarchical approach wherein the computational cost is decreased by only considering the inclusions in the near field of the inclusion being added and excluding all other inclusions in the far field. It is trivial exercise to show that inclusion of any shape can be contained in a convex ellipsoid with three semi principal axes a, b, and c with $R = \max \quad a,b,c$. Thus, for two ellipsoids with centers A and B, if the distance between A and B is larger than 2R, then these two ellipsoids do not intersect. Thus all the inclusions that are at a radial distance greater than 2R from the center of the inclusion being added can be excluded from the next intersection check in the three-step hierarchy.

5.2.3.2 Method of separating planes

The method of the separating planes is based on determining whether two convex objects are intersecting with each other by detecting if there is a node on one object that lies on or inside the other object given the relative position of the node on one object with respect to all the planes on the other object. Consider a plane in the infinite space that has two sides: the inner side and the outer side. By using the right-handed rule, it is possible to distinguish between the two sides. Let $\Delta\mathrm{ABC}$ be the triangle lying on this plane with nodal coordinates denoted by $A\quad x_a, y_a, z_a$, $B\quad x_b, y_b, z_b$ and $C\quad x_c, y_c, z_c$. The nodes are numbered counterclockwise. Consider an arbitrary node $P\quad x, y, z$. We determine its location relatively to the triangle $\Delta\mathrm{ABC}$ by calculating

$$\Delta = \begin{vmatrix} 1 & x_A & y_A & z_A \\ 1 & x_B & y_B & z_B \\ 1 & x_C & y_C & z_C \\ 1 & x & y & z \end{vmatrix} = \begin{vmatrix} x_B - x_A & y_B - y_A & z_B - z_A \\ x_C - x_A & y_C - y_A & z_C - z_A \\ x - x_A & y - y_A & z - z_A \end{vmatrix} \tag{5.2}$$

If $\Delta > 0$, then node P is at the outer side of the plane and vice versa; if $\Delta \leq 0$, then P is on the plane or at the inner side of the plane. If a node on a convex object lies inside all the surfaces of the other object, then the two convex objects are intersecting.

5.2.3.3 Method of separating axes

This section discusses the method of separating axis - the method employed to determine whether two stationary convex objects are intersecting or not. It can be proved that, two convex stationary objects will not intersect if there exists a line for which the intervals of projection of the two objects onto that line do not intersect. This line is termed as a *separating line* or, more commonly, as a *separating axis* [245].

Consider two compact, convex sets C_1 and C_2 and a line *D* passing through the origin. The projection intervals of these compact, convex sets on to the line *D* are given by

$$\begin{aligned} I_1 &= \left[\xi^1_{\min}(D), \xi^1_{\max}(D)\right] = \left[\min\{D\bullet X : X \in C_1\}, \max\{D\bullet X : X \in C_1\}\right] \\ I_2 &= \left[\xi^2_{\min}(D), \xi^2_{\max}(D)\right] = \left[\min\{D\bullet X : X \in C_2\}, \max\{D\bullet X : X \in C_2\}\right] \end{aligned} \tag{5.3}$$

where ξ is the projection vector on *D* and the superscripts corresponds to the index of the convex set. The two convex sets do not intersect, if $\xi^1_{\min}(D) > \xi^2_{\max}(D)$ or $\xi^1_{\max}(D) < \xi^2_{\min}(D)$. A 2D example is shown in Figure 5.2 to illustrate the idea of this method.

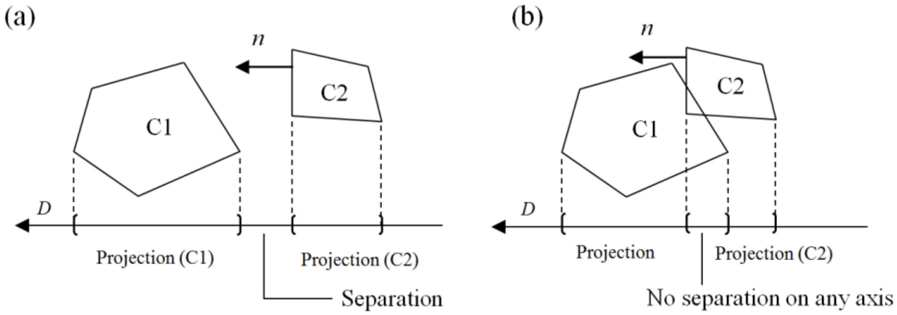

Figure 5.2 Intersection check in 2D using method separating axes

To check for the intersection of convex polyhedra in 3D space the set of direction vectors includes the normal vectors to the faces of the convex polyhedra and vectors generated by the cross product of two edges, one from each polyhedron. The curved fibers are considered to be comprising of *s* piecewise compact, convex sets. Let C_j with $j = 1,2$ be the convex polyhedra with vertices $\{V_i^{(j)}\}_{i=1}^{L}$ edges $\{E_i^{(j)}\}_{i=1}^{M}$ and faces $\{F_i^{(j)}\}_{i=1}^{N}$ with outward pointing normal to each face being computed and stored.

Alternatively, a separation check for convex polyhedra in 3D space can be performed by solving an optimization problem. Two convex polyhedra containing s faces can be algebraically defined by a set of solutions to a linear system of equations defined by

$$A_1\vec{x}_1 \leq b_1; \quad A_2\vec{x}_2 \leq b_2 \tag{5.4}$$

where A_1 and A_2 are real $s \times 3$ matrices, b_1 and b_2 are real $s \times 1$ matrices, and x_1 and x_2 are vectors of the coordinates of the convex polyhedra in 3D space.

The minimum distance between two inclusions in 3D space can then be determined by solving the convex optimization problem

$$d_{\min}^{3D} = \min[d(x_1, x_2)] \tag{5.5}$$

The minimization solution is computationally less efficient compared to method of separating axis. The flowchart for the hierarchical RSA algorithm is shown in Figure 5.3.

5.2.4 Random inclusion composite in three-dimensional space

The process of generating a random inclusion composite unit cell in 3D consists of placing inclusions of a given shape and size (or size range) and rotation angle (or rotation angle range) one by one in randomly selected positions in the unit cell domain. Each time a new inclusion is attempted to be placed in the unit cell domain, the overlaps with existing inclusions are detected. If a newly introduced inclusion does not overlap with others, it is allowed to stay in the RVE; otherwise, another position is attempted. If, after a predefined number of trials, the inclusion has not found its place so that it does not overlap with existing inclusions, it is discarded and another inclusion is selected and tried in the same manner. This process is repeated until a predefined inclusion volume fraction is reached. The algorithm can be easily implemented for complex inclusion geometries. However, the method is very time consuming and, for non-spherical inclusions, rearrangement by way of rotation is often not possible. Moreover, since some inclusions may have to be discarded, the size distribution of packed inclusions may be different from the intended. The packing density depends on the sequence of inclusion addition. For example, if larger inclusions are added first, the final packing density tends to be higher than if smaller inclusions are placed first. In the following paragraphs we describe the algorithm for unit cells with inclusions in the form of straight chopped fibers randomly oriented in 3D space and unit cells with ellipsoidal inclusions.

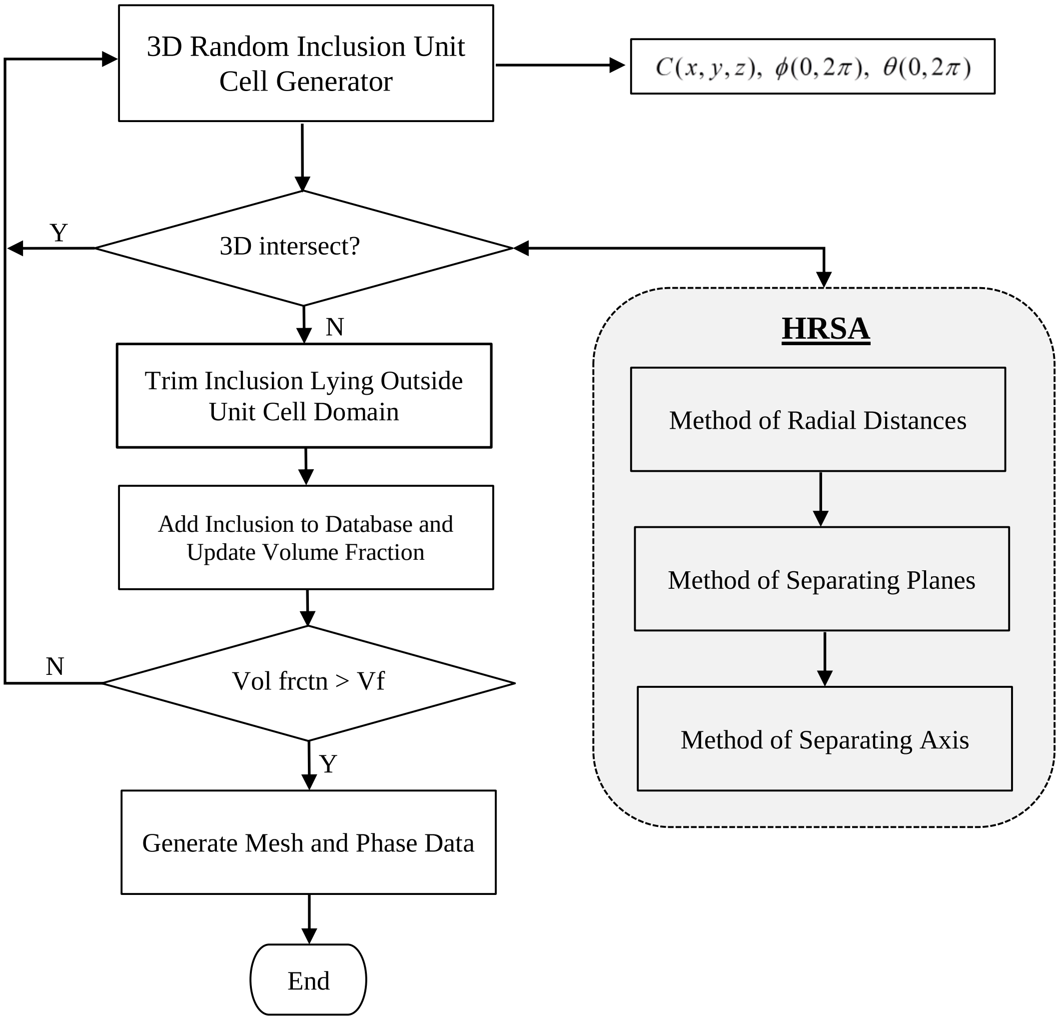

Figure 5.3: Hierarchical RSA algorithm

5.2.4.1 Unit cell with straight chopped fibers randomly oriented in 3D space

The microstructure of materials such as phenolic impregnated carbon ablators (PICA) consists of chopped fibers randomly dispersed in resin. The volume fraction of fibers is typically very small. The algorithm developed to generate the randomly oriented chopped fibers in 2D space can be tailored to generate the unit cell for carbon phenolic impregnated carbon ablators (PICA). The inclusions are idealized by straight cylinders, with user-defined cross-section and length. Since the inclusions are randomly oriented in 3D space, the center $C(x, y, z)$ and the in-plane $\phi(0, 2\pi)$ and the out-of-plane $\theta(0, 2\pi)$ angles are randomly generated. The random orientation in 3D space obviates the intersection check in 2D space. The aforementioned three-step intersection check process is used to check for fiber intersections in 3D space. A newly generated fiber is rejected if it fails the intersection check in 3D space. The unit cell with straight chopped fibers randomly oriented in 3D space is shown in Figure 5.4.

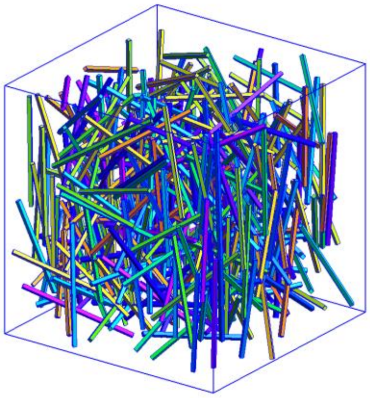

Figure 5.4 Straight chopped fibers randomly distributed in 3D

5.2.4.2 Unit cell with randomly oriented bonded chopped fibers free of matrix material (FiberForm)

FiberForm is a low density very porous carbon fiber insulation material designed for high temperatures applications. It consists of a group of carbon fibers bonded to each other by means of an organic binder that is carbonized at very high temperature as shown in Figure 5.5. The FiberForm unit cell is defined parametrically as a function of handful parameters, such as fiber characteristics (volume fraction, dimensions, orientations) and the dimensional characteristics of binders. The FiberForm unit cell generation process consists of two steps. In Step 1, a unit cell with randomly oriented disconnected fibers embedded in matrix material as described in the previous section is generated. In Step 2, the binders connecting the fibers are generated as follows. For each fiber, loop over all the other fibers and calculate the nearest distances. If the distance between two fibers is less than the user-prescribed binder length, a bond in the form of a cylinder is created to connect the nearest points on each fiber. After identifying all the bonds, assign matrix elements, which lie inside the cylindrical connectors, binder material properties. The resulting FiberForm unit cell consists of three phases: fibers, binders and fictitious matrix phase, which excludes the binders. There are two possibilities to proceed. Matrix elements lying outside the fiber and binder phases can be removed resulting in a two-phase material consisting of fibers and binders. Alternatively, one can assign negligible elastic material properties to the fictitious matrix phase resulting in a three phase material. The former is obviously computationally advantageous, while the latter provides additional robustness in case some fibers are “not sufficiently connected”, i.e. connected at a fewer than two nodes resulting in a mechanism and ultimately singularity of the resulting stiffness matrix. In the latter case, the fictitious matrix serves as a stabilizer. The FiberForm unit cell is depicted in Figure 5.5.

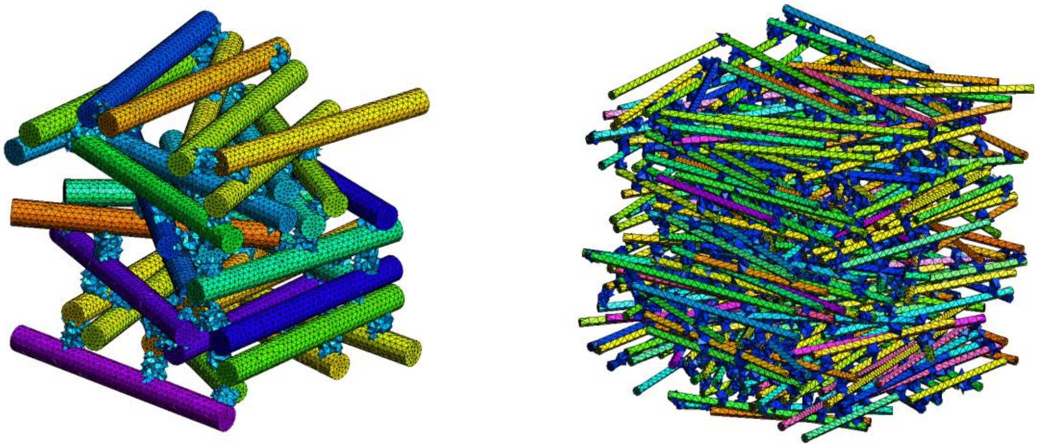

(a) (b)

Figure 5.5 (a) FiberForm unit cell with fiber volume fraction 5% and cross section radius=2.4; (b) FiberForm unit cell with fiber volume fraction 10% and cross section radius=0.6

5.2.4.3 Unit cell with ellipsoidal inclusions randomly oriented in 3D space

The ellipsoids geometry is defined by the coordinates of the center $C(x, y, z)$, the semi-principal axes a, b and c, the in-plane angle $\phi(0, 2\pi)$ and the out-of-plane angle $\theta(0, 2\pi)$. The center is generated randomly whereas the major axis a, minor axes b and c, and the in-plane angle ϕ and out-of-plane angle θ are user defined parameters. One can generate these parameters randomly or to specify exact values in order to generate unit cells with preferential size and packing angles of the ellipsoids. The ellipsoids are randomly oriented in 3D space. The geometry of an ellipsoidal inclusion is shown in Figure 5.6(a). As in the case of chopped fibers the ellipsoids are checked for intersection in 3D space using the three-step hierarchical approach discussed above. To this effect, an ellipsoid is discretized into a convex polyhedron with 48 sub-surfaces, as shown in Figure 5.7. A unit cell with randomly sized and oriented ellipsoids is depicted in Figure 5.6(b).

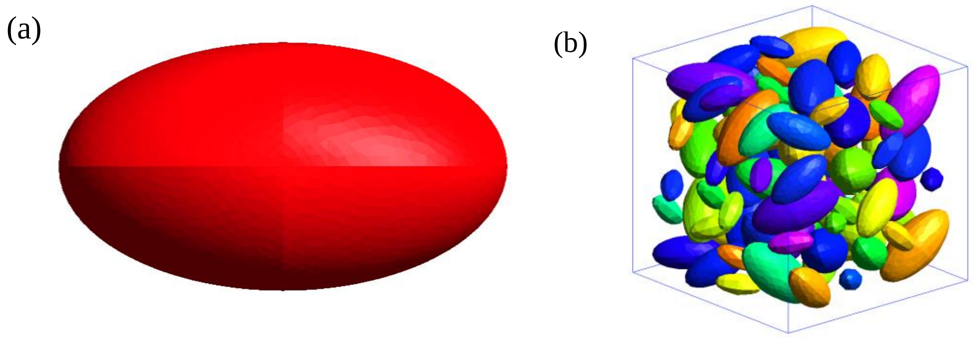

Figure 5.6 (a) Geometry of an ellipsoidal inclusion, (b) an ellipsoidal inclusion unit cell

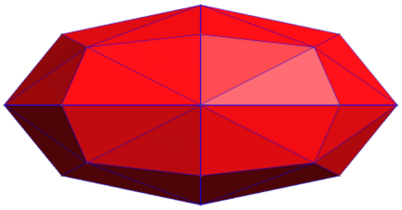

Figure 5.7 Discretization of an ellipsoidal inclusion into 48 faces

The computational times involved in generating a unit cell with ellipsoidal inclusions by employing the method of separating axes alone and the three step hierarchical approach for is shown in Figure 5.8. It is evident that the three-step intersection checking approach significantly reduces computational cost compared to the methods of separating axes alone.

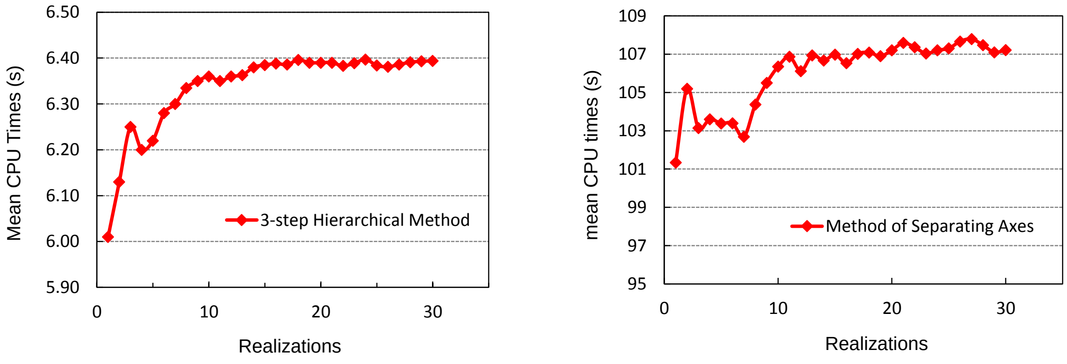

(a) (b)

Figure 5.8 Comparison of CPU times between the (a) 3-step hierarchical method and (b) method of separating axes

5.2.4.4 Unit cell with spherical inclusions in random and semi-random packing

Sphere packs have been used to model heterogeneous and porous material morphologies and to predict thermo-mechanical, permeability, packing density, and dissolution characteristics of various materials [246]. A maximum sphere volume fraction of 55% can be achieved through random packing algorithm without any intersection between spheres. Higher inclusion volume fraction can be achieved through semi-random packing. A unit cell with randomly packed spheres is shown in Figure 5.9. Unit cells with semi-random packed spheres for two predefined ordered patterns are depicted in Figure 5.10 and Figure 5.11.

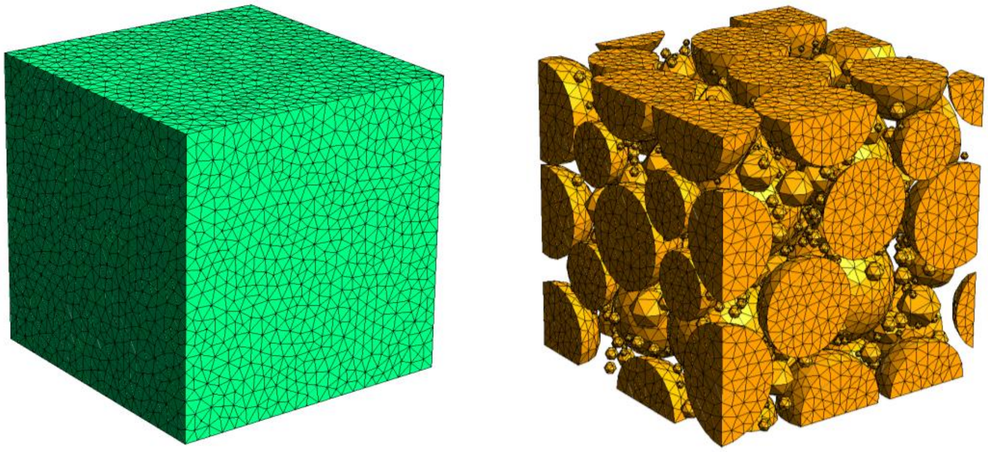
(a) (b)

Figure 5.9 Spherical inclusion unit cell using random packing (inclusion volume fraction is 52.3%)

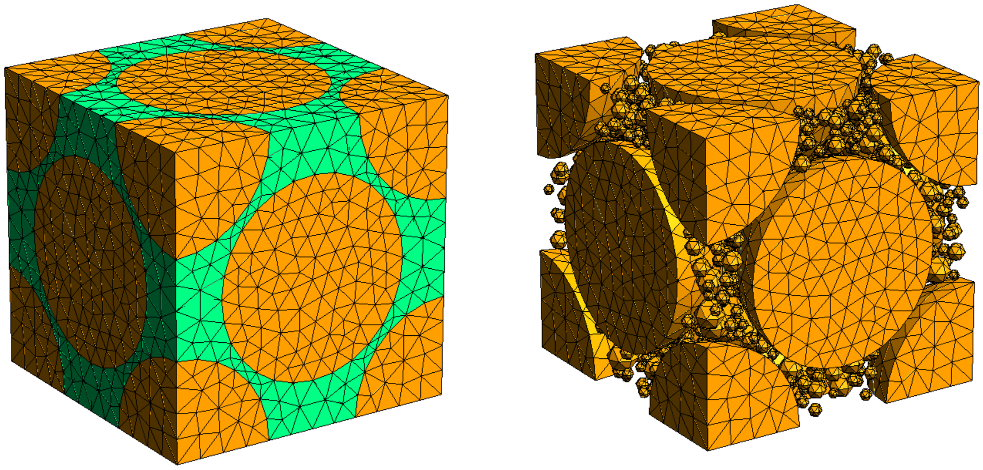
(a) (b)

Figure 5.10 Spherical inclusion unit cell using semi-random packing with pattern-1 (inclusion volume fraction is 68.4%)

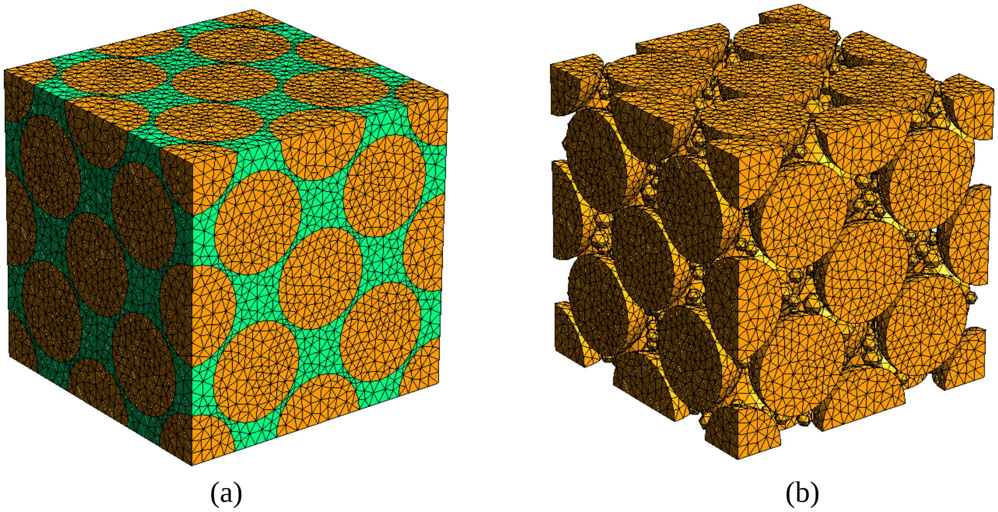
(a) (b)

Figure 5.11 Spherical inclusion unit cell using semi-random packing with pattern-2 (inclusion volume fraction is 65.6%)

5.2.4.5 Sphere packs with prescribed particle size distribution

In addition to particle size, shape and spatial orientations, the particle size distribution is another important feature to realistically model the microstructure of heterogeneous materials. The inclusion size distribution of a heterogeneous material can be obtained from X-ray CT image or laboratory tests. For example, average values of percent passing and grain size can be found in the mechanical sieve analysis for different types of sand, based on which grain assemblies with predefined particle size distribution can be generated by the proposed HRSA. In this section, we show an example of unit cell which is generated to represent the microstructure of Nevada sand. Figure 5.12(a) shows the unit cell with 5435 particles without particle intersection. The comparison between the particle size distributions of the generated virtual sphere packing and laboratory testing data is shown in Figure 5.12(b).

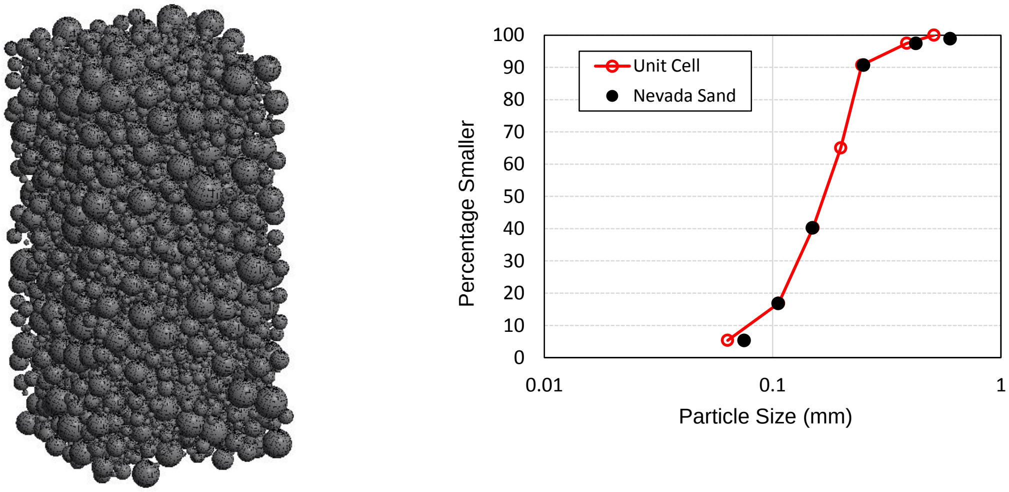

(a) (b)

Figure 5.12 (a) Sphere pack of 5435 particles; (b) comparison of particle size distributions between virtual sphere pack and laboratory test data for Nevada sand [184]

5.3 Methodology to control the volume fractions of constituent phases in the unit cell

The volume fractions of the constituent phases in the unit cell are affected by the geometry idealization and mesh size. Geometric approximation errors are introduced when curved features in the geometry are approximated by planar surfaces. Consequently, the resulting volume fractions of the constituent phases may vary from the actual volume fractions of phases. The errors introduced by mesh discretization can be reduced by refining the mesh, but this will significantly increase the computational cost involved in solving the unit cell problem. Alternatively, one can generate a higher volume fraction of the constituent phases than required, so that the resultant volume fraction attained is equal to the actual volume fraction of the constituent phase [225]. In the present chapter, the mesh density parameter is specified as a multiple of the fiber cross-section semi-minor axis b. For a mesh seeding size equal to b, the error introduced by mesh discretization has been found to be approximately 7%. The volume fraction errors introduced by finer mesh densities have been precomputed by numerical experiments. The following empirical equation was employed to obtain desired volume fraction

$$V_f^{gen} = V_f^{act}(1 + V_f^{error}) \tag{5.6}$$

where V_f^{gen} is the volume fraction generated, V_f^{des} is the desired volume fraction of the inclusion in the random chopped fiber composite and V_f^{error} is the error in the volume fraction introduced by mesh discretization.

5.4 Conclusion

A parametric model for generating unit cells with randomly distributed inclusions is presented in this chapter. The proposed algorithm has the following features: (i) robustness by yielding unit cells with inclusion volume fraction of up to 70%, (ii) computationally efficiency accomplished through a hierarchy of algorithms with increasing computational complexity, and (iii) versatility by generating unit cells with different inclusion shapes. The method has been applied to generate various random inclusion microstructure composites and granular assembly.

Chapter 6

Conclusions

The concluding chapter presents the main contributions and some concluding remarks of this dissertation. Directions of future research are also included.

6.1 Main contributions and concluding remarks

This dissertation explores and introduces new state-of-the-art multiscale modeling techniques that incorporate microstructural information to predict macroscopic mechanical behaviors for granular materials. We propose numerical methods and models to address the challenges associated with granular modeling. The new contribution of this research includes the development efficient predictive multiscale methods that (i) link coarse- and fine-scale governing equations, (ii) identify material parameters at different scales, (iii) alleviating mesh pathological dependency, and (iv) generate compatible unit cells with versatile morphological details. The first two chapters (Chapters 2 and 3) are the central theme of this work, followed by two supporting chapters (Chapters 4 and 5) for detailed demonstration of the proposed methods.

The author's main contributions in the field of multiscale modeling of granular materials presented in this dissertation are summarized as follows:

- **Nonlocal multiscale DEM-FEM model:** a three-dimensional nonlocal multiscale discrete-continuum model is presented for modeling the mechanical behavior of granular materials. We establish an information-passing coupling between DEM, which explicitly replicates granular motion of individual particles, and a finite element continuum model, which captures nonlocal overall response of the granular assemblies. The multiscale coupling scheme is able to capture the plastic dilatancy and pressure-sensitive frictional responses commonly observed inside dilatant shear bands, without employing a macroscopic phenomenological plasticity model. The simple shear and the biaxial compression tests are used to analyze the onset and evolution of shear bands in granular materials and sensitivity to mesh density. The robustness and accuracy of the proposed multiscale model are verified in comparisons with single-scale benchmark DEM simulations.

- **Multilevel material parameter identification:** a new staggered multilevel material identification procedure is presented for phenomenological critical state plasticity models. The emphasis is placed on cases in which available experimental data and constraints are insufficient for calibration. The key idea is to create a secondary virtual experimental database from high-fidelity models, such as discrete element simulations, then merge both the actual experimental data and secondary database as an extended digital database to determine material parameters for the phenomenological macroscopic critical state plasticity model. The expansion of database provides additional constraints necessary for calibration of the phenomenological critical state plasticity models. The robustness of the proposed material identification framework is demonstrated in the context of the Dafalias-Manzari plasticity model.
- **Regularized phenomenological multiscale damage model:** a regularized phenomenological multiscale model is developed, where elastic properties are computed using direct homogenization and subsequently evolved using a simple three-parameter orthotropic continuum damage model. A unified regularization scheme is proposed in the context of constitutive law rescaling and staggered nonlocal approaches. The method has been validated for three problems: (i) edge-cracked plate under impulsive loading, (ii) four-point bending of a steel wire reinforced cement beam, and (iii) mode I fracture of a two-dimensional triaxially

braided carbon fiber composite. For all three test problems we show that: (i) the regularized phenomenological multiscale model is capable of reproducing the test data with each of the two regularization technique, and (ii) the simulation results obtained are practically mesh size independent. In addition, the computational cost of the rescaling approach is lower than of the staggered nonlocal approach, but the crack propagation path as obtained with the staggered nonlocal approach is often smoother.

- **Automated unit cell generation:** a parametric model for generating unit cells with randomly distributed inclusions. The proposed algorithm possesses the following characteristics: (i) robustness by yielding unit cells with inclusion volume fraction of up to 78%, (ii) computationally efficiency accomplished through a hierarchy of algorithms with increasing computational complexity, and (iii) versatility by generating unit cells with different inclusion shapes. A statistical study aimed at determining the effective size of the unit cell is conducted. The method has been applied to various random inclusion microstructure composites including polyurea or polyethene coating consisting of hard and soft domains, and fiber framework embedded in an amorphous matrix used as heat shield on space crafts. The proposed automated unit cell generation algorithm can be potentially used in generating mircrostructures for numerical simulation and analysis of composite materials.

6.2 Future research directions

Some other interesting studies could be further explored beyond the scope of this dissertation. Based on the advancements and progresses of this present work, future research can be directed as follows:

- **Multiscale DEM-FEM model considering diffusive tensors:** the present multiscale DEM-FEM model only deals with single-phase granular materials consisting of solid particles, which has limitations in application to solve multiphysics problems. In many real problems, the mechanical responses of granular materials are quite likely to couple with other physical processes, such as heat transfer, chemical reaction and pore-fluid diffusions. The work presented in this dissertation provides a good starting point for new multiscale/multiphysics discrete-continuum models that deal with granular materials interacting with species in pore space. New models that extend the current spatial homogenization techniques to the deformation-diffusion coupled processes may have significant impacts for a number of engineering applications.

- **Modeling DEM assembly with grains of arbitrary geometries:** in the present study, the particles used in the grain assemblies are mostly spherical which cannot realistically represent the real granular particles. Though the automated unit cell generation technique presented in Chapter 5 is able to generate inclusions with different shapes for the representation of composite microstructures, the algorithm has yet been applied to generate DEM assemblies. Since the particle shapes affect the mechanical behavior of a granular system, it is necessary to realistically model the actual particle geometries. Therefore, a possible research direction could be realistically modeling grain assemblies with arbitrarily shaped particles using NURBS [247] or potential element methods.

- **Robust material parameter calibration approach:** the present inversion approach used in the multilevel material parameter calibration is a traditional gradient-based optimization method. Several issues exist when applying this optimization technique to determine the materials parameters: (i) strong dependence on the initial guess, (ii) difficulty to distinguish global and local minima in the parametric space, (3) convergence problem associated with the number of parameters and the availability of test data. To overcome the above listed issues, in the future, it will be interesting to exploit new robust algorithms to solve such an inverse problem. Statistical optimization such as the Markov chain Monte Carlo (MCMC) simulation based on Bayesian inference might be a good alternative. In this way, probabilistic distributions of the material parameters instead of deterministic values could be obtained and be used for robust mechanical behavior prediction of the granular materials.

Bibliography

1. Klose, M., B. Damm, and B. Terhorst, *Landslide cost modeling for transportation infrastructures: a methodological approach*. Landslides, 2015. **12**(2): p. 321-334.
2. Schuster, R.L. and R.W. Fleming, *Economic losses and fatalities due to landslides.* Bulletin of the Association of Engineering Geologists, 1986. **23**(1): p. 11-28.
3. Prager, W., *Introduction to mechanics of continua*. 2004: Courier Corporation.
4. Cosserat, E. and F. Cosserat, *Théorie des corps déformables.* Paris, 1909.
5. Duncan, J.M. and C.-Y. Chang, *Nonlinear analysis of stress and strain in soils.* Journal of the soil mechanics and foundations division, 1970. **96**(5): p. 1629-1653.
6. Drucker, D.C. and W. Prager, *Soil mechanics and plastic analysis or limit design.* Quarterly of applied mathematics, 1952. **10(2)**: p. 157-165.
7. Rowe, P.W. *The stress-dilatancy relation for static equilibrium of an assembly of particles in contact*. in *Proceedings of the Royal Society of London A: Mathematical, Physical and Engineering Sciences*. 1962. The Royal Society.
8. DiMaggio, F.L. and I.S. Sandler, *Material model for granular soils.* Journal of the Engineering mechanics Division, 1971. **97**(3): p. 935-950.
9. Lade, P.V. and J.M. Duncan, *Elastoplastic stress-strain theory for cohesionless soil.* Journal of the Geotechnical Engineering Division, 1975. **101**(10): p. 1037-1053.
10. Bardet, J., *Bounding surface plasticity model for sands.* Journal of engineering mechanics, 1986. **112**(11): p. 1198-1217.
11. Oka, F., T. Adachi, and A. Yashima, *A strain localization analysis using a viscoplastic softening model for clay.* International journal of plasticity, 1995. **11**(5): p. 523-545.
12. Nemat-Nasser, S. and J. Zhang, *Constitutive relations for cohesionless frictional granular materials.* International Journal of Plasticity, 2002. **18**(4): p. 531-547.
13. Yang, Z. and A. Elgamal, *Multi-surface cyclic plasticity sand model with Lode angle effect.* Geotechnical and Geological Engineering, 2008. **26**(3): p. 335-348.
14. Schofield, A. and P. Wroth, *Critical state soil mechanics.* 1968.

15. Dafalias, Y.F. and M.T. Manzari, *Simple plasticity sand model accounting for fabric change effects.* Journal of Engineering mechanics, 2004. **130**(6): p. 622-634.
16. Jefferies, M., *Nor-Sand: a simle critical state model for sand.* Géotechnique, 1993. **43**(1): p. 91-103.
17. Borja, R.I. and S.R. Lee, *Cam-clay plasticity, part 1: implicit integration of elasto-plastic constitutive relations.* Computer Methods in Applied Mechanics and Engineering, 1990. **78**(1): p. 49-72.
18. Rudnicki, J.W. and J. Rice, *Conditions for the localization of deformation in pressure-sensitive dilatant materials.* Journal of the Mechanics and Physics of Solids, 1975. **23**(6): p. 371-394.
19. Borja, R.I. and A. Aydin, *Computational modeling of deformation bands in granular media. I. Geological and mathematical framework.* Computer Methods in Applied Mechanics and Engineering, 2004. **193**(27): p. 2667-2698.
20. Lade, P.V., *Static instability and liquefaction of loose fine sandy slopes.* Journal of Geotechnical Engineering, 1992. **118**(1): p. 51-71.
21. Tsang, C.-F., et al., *Coupled thermo-hydro-mechanical processes in the near field of a high-level radioactive waste repository in clay formations.* International Journal of Rock Mechanics and Mining Sciences, 2012. **49**: p. 31-44.
22. Terzaghi, K.v., *Old earth pressure theories and new test results.* Engineering News Record, 1920. **85**(14): p. 632-637.
23. Christoffersen, J., M. Mehrabadi, and S. Nemat-Nasser, *A micromechanical description of granular material behavior.* Journal of Applied Mechanics, 1981. **48**(2): p. 339-344.
24. Bagi, K., *Stress and strain in granular assemblies.* Mechanics of materials, 1996. **22**(3): p. 165-177.
25. Cundall, P.A. and O.D. Strack, *A discrete numerical model for granular assemblies.* Geotechnique, 1979. **29**(1): p. 47-65.
26. O'Sullivan, C., J.D. Bray, and M.F. Riemer, *Influence of particle shape and surface friction variability on response of rod-shaped particulate media.* Journal of Engineering Mechanics, 2002. **128**(11): p. 1182-1192.
27. Lin, X. and T.-T. Ng, *A three-dimensional discrete element model using arrays of ellipsoids.* Geotechnique, 1997. **47**(2): p. 319-329.
28. Sadd, M.H., G. Adhikari, and F. Cardoso, *DEM simulation of wave propagation in granular materials.* Powder Technology, 2000. **109**(1-3): p. 222-233.
29. Kuhn, M.R., W. Sun, and Q. Wang, *Stress-induced anisotropy in granular materials: fabric, stiffness, and permeability.* Acta Geotechnica, 2015: p. 1-21.
30. Borja, R.I. and W.C. Sun, *Estimating inelastic sediment deformation from local site response simulations.* Acta Geotechnica, 2007. **2**(3): p. 183-195.

31. Borja, R.I. and W. Sun, *Coseismic sediment deformation during the 1989 Loma Prieta earthquake.* Journal of Geophysical Research: Solid Earth (1978–2012), 2008. **113**(B8).
32. Viggiani, G., et al., *Laboratory X-ray Tomography: A Valuable Experimental Tool for Revealing Processes in Soils.* GEOTECHNICAL TESTING JOURNAL, 2015. **38**(1): p. 61-71.
33. Sun, W., et al., *Connecting microstructural attributes and permeability from 3D tomographic images of in situ shear‐enhanced compaction bands using multiscale computations.* Geophysical Research Letters, 2011. **38**(10).
34. Fish, J., *Practical multiscaling*. 2013: John Wiley & Sons.
35. Guedes, J. and N. Kikuchi, *Preprocessing and postprocessing for materials based on the homogenization method with adaptive finite element methods.* Computer methods in applied mechanics and engineering, 1990. **83**(2): p. 143-198.
36. Matsui, K., K. Terada, and K. Yuge, *Two-scale finite element analysis of heterogeneous solids with periodic microstructures.* Computers & structures, 2004. **82**(7): p. 593-606.
37. Ghosh, S., K. Lee, and S. Moorthy, *Two scale analysis of heterogeneous elastic-plastic materials with asymptotic homogenization and Voronoi cell finite element model.* Computer Methods in Applied Mechanics and Engineering, 1996. **132**(1): p. 63-116.
38. Michel, J., H. Moulinec, and P. Suquet, *Effective properties of composite materials with periodic microstructure: a computational approach.* Computer methods in applied mechanics and engineering, 1999. **172**(1): p. 109-143.
39. Yuan, Z. and J. Fish, *Toward realization of computational homogenization in practice.* International Journal for Numerical Methods in Engineering, 2008. **73**(3): p. 361.
40. Miehe, C. and A. Koch, *Computational micro-to-macro transitions of discretized microstructures undergoing small strains.* Archive of Applied Mechanics, 2002. **72**(4-5): p. 300-317.
41. Feyel, F., *A multilevel finite element method (FE< sup> 2</sup>) to describe the response of highly non-linear structures using generalized continua.* Computer Methods in applied Mechanics and engineering, 2003. **192**(28): p. 3233-3244.
42. Miehe, C. and J. Dettmar, *A framework for micro–macro transitions in periodic particle aggregates of granular materials.* Computer Methods in Applied Mechanics and Engineering, 2004. **193**(3): p. 225-256.
43. Onate, E. and J. Rojek, *Combination of discrete element and finite element methods for dynamic analysis of geomechanics problems.* Computer methods in applied mechanics and engineering, 2004. **193**(27): p. 3087-3128.
44. Wellmann, C., C. Lillie, and P. Wriggers, *Homogenization of granular material modeled by a three-dimensional discrete element method.* Computers and Geotechnics, 2008. **35**(3): p. 394-405.

45. Andrade, J.E. and X. Tu, *Multiscale framework for behavior prediction in granular media.* Mechanics of Materials, 2009. **41**(6): p. 652-669.
46. Miehe, C., J. Dettmar, and D. Zäh, *Homogenization and two‐scale simulations of granular materials for different microstructural constraints.* International Journal for Numerical Methods in Engineering, 2010. **83**(8‐9): p. 1206-1236.
47. Regueiro, R.A. and B. Yan, *Concurrent multiscale computational modeling for dense dry granular materials interfacing deformable solid bodies*, in *Bifurcations, Instabilities and Degradations in Geomaterials*. 2011, Springer. p. 251-273.
48. Wellmann, C. and P. Wriggers, *A two-scale model of granular materials.* Computer Methods in Applied Mechanics and Engineering, 2012. **205**: p. 46-58.
49. Sun, W., M.R. Kuhn, and J.W. Rudnicki, *A multiscale DEM-LBM analysis on permeability evolutions inside a dilatant shear band.* Acta Geotechnica, 2013. **8**(5): p. 465-480.
50. Guo, N. and J. Zhao, *A coupled FEM/DEM approach for hierarchical multiscale modelling of granular media.* International Journal for Numerical Methods in Engineering, 2014. **99**(11): p. 789-818.
51. Li, X. and K. Wan, *A bridging scale method for granular materials with discrete particle assembly–Cosserat continuum modeling.* Computers and Geotechnics, 2011. **38**(8): p. 1052-1068.
52. Stránský, J. and M. Jirásek, *OPEN SOURCE FEM-DEM COUPLING.* Engineering Mechanics, 2012: p. 18.
53. Nguyen, T.K., et al., *FEM× DEM modelling of cohesive granular materials: Numerical homogenisation and multi-scale simulations.* Acta Geophysica, 2014. **62**(5): p. 1109-1126.
54. Chen, W. and J. Fish, *A generalized space–time mathematical homogenization theory for bridging atomistic and continuum scales.* International Journal for Numerical Methods in Engineering, 2006. **67**(2): p. 253-271.
55. Chen, W. and J. Fish, *A mathematical homogenization perspective of virial stress.* International journal for numerical methods in engineering, 2006. **67**(2): p. 189-207.
56. Fish, J., W. Chen, and R. Li, *Generalized mathematical homogenization of atomistic media at finite temperatures in three dimensions.* Computer methods in applied mechanics and engineering, 2007. **196**(4): p. 908-922.
57. Liu, Y., et al., *A nonlocal multiscale discrete-continuum model for predicting mechanical behavior of granular materials.* International journal for numerical methods in engineering, 2015. **Accepted**.
58. de Borst, R., *A generalisation of J2-flow theory for polar continua.* Computer Methods in Applied Mechanics and Engineering, 1993. **103**(3): p. 347-362.
59. Vermeer, P.A. and R. De Borst, *Non-associated plasticity for soils, concrete and rock.* 1984.

60. Kingston, M. and A. Spencer, *General yield conditions in plane deformations of granular media.* Journal of the Mechanics and Physics of Solids, 1970. **18**(3): p. 233-243.
61. Pestana, J.M. and A.J. Whittle, *Formulation of a unified constitutive model for clays and sands.* International Journal for Numerical and Analytical Methods in Geomechanics, 1999. **23**(12): p. 1215-1243.
62. Pestana, J.M., A.J. Whittle, and L.A. Salvati, *Evaluation of a constitutive model for clays and sands: Part I–sand behaviour.* International journal for numerical and analytical methods in geomechanics, 2002. **26**(11): p. 1097-1121.
63. Assimaki, D., E. Kausel, and A. Whittle, *Model for dynamic shear modulus and damping for granular soils.* Journal of Geotechnical and Geoenvironmental Engineering, 2000. **126**(10): p. 859-869.
64. Wang, Z.-L., Y.F. Dafalias, and C.-K. Shen, *Bounding surface hypoplasticity model for sand.* Journal of engineering mechanics, 1990. **116**(5): p. 983-1001.
65. Manzari, M.T. and Y.F. Dafalias, *A critical state two-surface plasticity model for sands.* Geotechnique, 1997. **47**(2): p. 255-272.
66. De Borst, R., et al., *Fundamental issues in finite element analyses of localization of deformation.* Engineering computations, 1993. **10**(2): p. 99-121.
67. Rechenmacher, A., S. Abedi, and O. Chupin, *Evolution of force chains in shear bands in sands.* Geotechnique, 2010. **60**(5): p. 343-351.
68. Cundall, P.A. *A computer model for simulating progressive large scale movements in blocky rock systems*. in *Proc. Symp. Rock Fracture (ISRM), Nancy*. 2013.
69. Kouznetsova, V., M.G. Geers, and W.M. Brekelmans, *Multi‐scale constitutive modelling of heterogeneous materials with a gradient‐enhanced computational homogenization scheme.* International Journal for Numerical Methods in Engineering, 2002. **54**(8): p. 1235-1260.
70. Geers, M., V. Kouznetsova, and W. Brekelmans, *Multi-scale computational homogenization: Trends and challenges.* Journal of computational and applied mathematics, 2010. **234**(7): p. 2175-2182.
71. Bardet, J. and J. Proubet, *A numerical investigation of the structure of persistent shear bands in granular media.* Geotechnique, 1991. **41**(4): p. 599-613.
72. Sun, W.C., M.R. Kuhn, and J.W. Rudnicki. *A Micromechanical Analysis on Permeability Evolutions of a Dilatant Shear Band*. in *48th US Rock Mechanics/Geomechanics Symposium*. 2014. American Rock Mechanics Association.
73. Fish, J., T. Jiang, and Z. Yuan, *A staggered nonlocal multiscale model for a heterogeneous medium.* International Journal for Numerical Methods in Engineering, 2012. **91**(2): p. 142-157.

74. Liu, Y., et al., *A regularized phenomenological multiscale damage model.* International Journal for Numerical Methods in Engineering, 2014. **99**(12): p. 867-887.
75. Rothenburg, L. and A. Selvadurai, *A micromechanical definition of the {C} auchy stress tensor for particulate media.* 1981.
76. Newland, P. and B. Allely, *Volume Changes in Drained Taixial Tests on Granular Materials.* Geotechnique, 1957. **7**(1): p. 17-34.
77. Oda, M. and K. Iwashita, *Study on couple stress and shear band development in granular media based on numerical simulation analyses.* International Journal of Engineering Science, 2000. **38**(15): p. 1713-1740.
78. Mühlhaus, H. and I. Vardoulakis, *The thickness of shear bands in granular materials.* Geotechnique, 1987. **37**(3): p. 271-283.
79. Brown, C. and R. Evans, *On the application of couple-stress theories to granular media.* Geotechnique, 1972. **22**(2): p. 356-361.
80. Fish, J., V. Filonova, and S. Kuznetsov, *Micro‐inertia effects in nonlinear heterogeneous media.* International Journal for Numerical Methods in Engineering, 2012. **91**(13): p. 1406-1426.
81. Mühlhaus, H. and F. Oka, *Dispersion and wave propagation in discrete and continuous models for granular materials.* International Journal of Solids and Structures, 1996. **33**(19): p. 2841-2858.
82. Belytschko, T., et al., *Nonlinear finite elements for continua and structures*. 2013: John Wiley & Sons.
83. Bardet, J. and J. Proubet, *Adaptative dynamic relaxation for statics of granular materials.* Computers & structures, 1991. **39**(3): p. 221-229.
84. Ng, T.-T., *Input parameters of discrete element methods.* Journal of Engineering Mechanics, 2006. **132**(7): p. 723-729.
85. Suzuki, K. and M.R. Kuhn, *Uniqueness of discrete element simulations in monotonic biaxial shear tests.* International Journal of Geomechanics, 2013.
86. Tu, X. and J.E. Andrade, *Criteria for static equilibrium in particulate mechanics computations.* International journal for numerical methods in engineering, 2008. **75**(13): p. 1581-1606.
87. Padbidri, J.M. and S.D. Mesarovic, *Acceleration of DEM algorithm for quasistatic processes.* International Journal for Numerical Methods in Engineering, 2011. **86**(7): p. 816-828.
88. Filonova, V., et al., *Corotational formulation of reduced order homogenization.* CMC: Computers, Materials & Continua, 2013. **34**(3): p. 177-198.
89. Yuan, Z. and J. Fish, *Reusable, Extensible and Computationally Efficient Three-Dimensional Nonlinear Multiphysics Finite Element Code Architecture in Object Oriented Fortran Environment.* Finite Elements in Analysis and Design, 2014. **[submitted]**.

90. Kuhn, M.R., *OVAL and OVALPLOT: Programs for analyzing dense particle assemblies with the discrete element method*. 2006, 98p.
91. Kuhn, M.R., *Structured deformation in granular materials.* Mechanics of materials, 1999. **31**(6): p. 407-429.
92. Cundall, P., *Distinct element models of rock and soil structure.* Analytical and computational methods in engineering rock mechanics, 1987. **4**: p. 129-163.
93. Thornton, C., *Numerical simulations of deviatoric shear deformation of granular media.* Géotechnique, 2000. **50**(1): p. 43-53.
94. Makse, H.A., et al., *Why effective medium theory fails in granular materials.* Physical Review Letters, 1999. **83**(24): p. 5070.
95. Hill, R., *Elastic properties of reinforced solids: some theoretical principles.* Journal of the Mechanics and Physics of Solids, 1963. **11**(5): p. 357-372.
96. Ostoja-Starzewski, M., *Material spatial randomness: From statistical to representative volume element.* Probabilistic Engineering Mechanics, 2006. **21**(2): p. 112-132.
97. Ostoja-Starzewski, M., et al., *Comparisons of the size of the representative volume element in elastic, plastic, thermoelastic, and permeable random microstructures.* International Journal for Multiscale Computational Engineering, 2007. **5**(2).
98. Sun, W., J.E. Andrade, and J.W. Rudnicki, *Multiscale method for characterization of porous microstructures and their impact on macroscopic effective permeability.* International Journal for Numerical Methods in Engineering, 2011. **88**(12): p. 1260-1279.
99. Meier, H., P. Steinmann, and E. Kuhl, *Towards multiscale computation of confined granular media-Contact forces, stresses and tangent operators.* Technische Mechanik, 2008. **28**(1): p. 32-42.
100. Belytschko, T., S. Loehnert, and J.H. Song, *Multiscale aggregating discontinuities: a method for circumventing loss of material stability.* International Journal for Numerical Methods in Engineering, 2008. **73**(6): p. 869-894.
101. Belytschko, T. and L.P. Bindeman, *Assumed strain stabilization of the eight node hexahedral element.* Computer Methods in Applied Mechanics and Engineering, 1993. **105**(2): p. 225-260.
102. Sun, W., J.T. Ostien, and A.G. Salinger, *A stabilized assumed deformation gradient finite element formulation for strongly coupled poromechanical simulations at finite strain.* International Journal for Numerical and Analytical Methods in Geomechanics, 2013. **37**(16): p. 2755-2788.
103. Bao, H., et al., *Large-scale simulation of elastic wave propagation in heterogeneous media on parallel computers.* Computer methods in applied mechanics and engineering, 1998. **152**(1): p. 85-102.
104. Zeghal, M. and A.W. Elgamal, *Site response and vertical seismic arrays.* Progress in Structural Engineering and Materials, 2000. **2**(1): p. 92-101.

105. Zeghal, M. and C. Oskay, *Local system identification analyses of the dynamic response of soil systems.* Soil Dynamics and Earthquake Engineering, 2002. **22**(9): p. 985-993.
106. Bielak, J. and P. Christiano, *On the effective seismic input for non‐linear soil‐structure interaction systems.* Earthquake engineering & structural dynamics, 1984. **12**(1): p. 107-119.
107. Yoshimura, C., et al., *Domain reduction method for three-dimensional earthquake modeling in localized regions, part II: Verification and applications.* Bulletin of the Seismological Society of America, 2003. **93**(2): p. 825-841.
108. Prevost, J.H., *A simple plasticity theory for frictional cohesionless soils.* International Journal of Soil Dynamics and Earthquake Engineering, 1985. **4**(1): p. 9-17.
109. Zamani, N. and U. El Shamy, *Analysis of wave propagation in dry granular soils using DEM simulations.* Acta Geotechnica, 2011. **6**(3): p. 167-182.
110. Sadd, M.H., Q. Tai, and A. Shukla, *Contact law effects on wave propagation in particulate materials using distinct element modeling.* International Journal of Non-Linear Mechanics, 1993. **28**(2): p. 251-265.
111. Zeghal, M., *Discrete-element method investigation of the resilient behavior of granular materials.* Journal of Transportation Engineering, 2004. **130**(4): p. 503-509.
112. Wang, C., D. Tannant, and P. Lilly, *Numerical analysis of the stability of heavily jointed rock slopes using PFC2D.* International Journal of Rock Mechanics and Mining Sciences, 2003. **40**(3): p. 415-424.
113. Casagrande, A., *Characteristics of cohensionless soils affecting the stability of slops and earth fills.* J Boston Soc Civil Eng, 1936(23): p. 13-32.
114. Bazant, Z.P. and M. Jirásek, *Nonlocal integral formulations of plasticity and damage: survey of progress.* Journal of Engineering Mechanics, 2002. **128**(11): p. 1119-1149.
115. Sun, W. and A. Mota, *A multiscale overlapped coupling formulation for large-deformation strain localization.* Computational Mechanics, 2014: p. 1-18.
116. Fleck, N. and J. Hutchinson, *A reformulation of strain gradient plasticity.* Journal of the Mechanics and Physics of Solids, 2001. **49**(10): p. 2245-2271.
117. Belytschko, T., J. Fish, and B.E. Engelmann, *A finite element with embedded localization zones.* Computer Methods in Applied Mechanics and Engineering, 1988. **70**(1): p. 59-89.
118. Borja, R.I., *A finite element model for strain localization analysis of strongly discontinuous fields based on standard Galerkin approximation.* Computer Methods in Applied Mechanics and Engineering, 2000. **190**(11): p. 1529-1549.
119. Borja, R.I., *Finite element simulation of strain localization with large deformation: capturing strong discontinuity using a Petrov–Galerkin multiscale formulation.* Computer Methods in Applied Mechanics and Engineering, 2002. **191**(27): p. 2949-2978.

120. Dolbow, J. and T. Belytschko, *A finite element method for crack growth without remeshing.* Int. J. Numer. Meth. Engng, 1999. **46**(1): p. 131-150.

121. Yang, Q., A. Mota, and M. Ortiz, *A class of variational strain‐localization finite elements.* International Journal for Numerical Methods in Engineering, 2005. **62**(8): p. 1013-1037.

122. Liu, Y., W.C. Sun, and J. Fish, *Determining material parameters for critical state plasticity models based on multilevel extended digital database.* Journal of Applied Mechanics 2015. **Accepted**.

123. Liam Finn, W., K.W. Lee, and G. Martin, *An effective stress model for liquefaction.* Electronics Letter, 1977. **103**(ASCE 13008 Proceeding).

124. Anandarajah, A. *VELACS project: elasto-plastic finite element prediction of the liquefaction behavior of centrifuge models nos. 1, 3 and 4a*. in *Proc., Int. Conf. on the Verification of Numerical Procedures for the Analysis of Soil Liquefaction Problems*. 1993. Balkema, Rotterdam, The Netherlands.

125. Borja, R.I., et al., *Nonlinear ground response at Lotung LSST site.* Journal of geotechnical and geoenvironmental engineering, 1999. **125**(3): p. 187-197.

126. Jeremic, B., K. Runesson, and S. Sture, *A model for elastic-plastic pressure sensitive materials subjected to large deformations.* International journal of solids and structures, 1999. **36**(31): p. 4901-4918.

127. Lashkari, A. and M. Latifi, *A non‐coaxial constitutive model for sand deformation under rotation of principal stress axes.* International journal for numerical and analytical methods in geomechanics, 2008. **32**(9): p. 1051-1086.

128. Andrade, J.E. and K.C. Ellison, *Evaluation of a predictive constitutive model for sands.* Journal of geotechnical and geoenvironmental engineering, 2008. **134**(12): p. 1825-1828.

129. Li, L., M. Aubertin, and A. Shirazi, *Implementation and application of a new elastoplastic model based on a multiaxial criterion to assess the stress state near underground openings.* International Journal of Geomechanics, 2010.

130. Roscoe, K.H., A. Schofield, and C. Wroth, *On the yielding of soils.* Geotechnique, 1958. **8**(1): p. 22-53.

131. Roscoe, K.H. and J. Burland, *On the generalized stress-strain behaviour of wet clay.* 1968.

132. Nova, R. and D.M. Wood, *A constitutive model for sand in triaxial compression.* International Journal for Numerical and Analytical Methods in Geomechanics, 1979. **3**(3): p. 255-278.

133. Borja, R.I. and J.E. Andrade, *Critical state plasticity. Part VI: Meso-scale finite element simulation of strain localization in discrete granular materials.* Computer Methods in Applied Mechanics and Engineering, 2006. **195**(37): p. 5115-5140.

134. Gao, Z., et al., *A critical state sand plasticity model accounting for fabric evolution.* International journal for numerical and analytical methods in geomechanics, 2014. **38**(4): p. 370-390.

135. Tanaka, M. and G.S. Dulikravich, *Inverse problems in engineering mechanics*. 1998: Elsevier.
136. Chaparro, B., et al., *Material parameters identification: Gradient-based, genetic and hybrid optimization algorithms.* Computational Materials Science, 2008. **44**(2): p. 339-346.
137. Yang, Z. and A. Elgamal, *Application of unconstrained optimization and sensitivity analysis to calibration of a soil constitutive model.* International journal for numerical and analytical methods in geomechanics, 2003. **27**(15): p. 1277-1297.
138. Blaheta, R., et al., *Material parameter identification with parallel processing and geo-applications*, in *Parallel Processing and Applied Mathematics*. 2012, Springer. p. 366-375.
139. Feng, X.-T., et al., *Identification of visco-elastic models for rocks using genetic programming coupled with the modified particle swarm optimization algorithm.* International Journal of Rock Mechanics and Mining Sciences, 2006. **43**(5): p. 789-801.
140. Ghaboussi, J., et al., *Autoprogressive training of neural network constitutive models.* International Journal for Numerical Methods in Engineering, 1998. **42**(1): p. 105-126.
141. Li, X. *Calibration of an anisotropic sand model*. in *Calibration of Constitutive Models*. 2005. ASCE.
142. Papadimitriou, A.G. and G.D. Bouckovalas, *Plasticity model for sand under small and large cyclic strains: a multiaxial formulation.* Soil Dynamics and Earthquake Engineering, 2002. **22**(3): p. 191-204.
143. Shahir, H., et al., *Evaluation of variation of permeability in liquefiable soil under earthquake loading.* Computers and Geotechnics, 2012. **40**: p. 74-88.
144. Choi, C., P. Arduino, and M.D. Harney. *Two-Surface Soil Constitutive Model Calibration for Coarse Granular Materials*. in *Calibration of Constitutive Models*. 2005. ASCE.
145. Mahnken, R. and E. Stein, *The identification of parameters for visco-plastic models via finite-element methods and gradient methods.* Modelling and simulation in materials science and engineering, 1994. **2**(3A): p. 597.
146. Mahnken, R. and E. Stein, *A unified approach for parameter identification of inelastic material models in the frame of the finite element method.* Computer methods in applied mechanics and engineering, 1996. **136**(3): p. 225-258.
147. Rechenmacher, A.L. and Z. Medina-Cetina, *Calibration of soil constitutive models with spatially varying parameters.* Journal of Geotechnical and Geoenvironmental Engineering, 2007. **133**(12): p. 1567-1576.
148. Arnold, S.M., F. Holland, and B.A. Bednarcyk. *Robust informatics infrastructure required for ICME: combining virtual and experimental data*. in *55th AIAA/ASMe/ASCE/AHS/SC structures, structural dynamics, and materials conference*. 2014.
149. Broderick, S.R., H. Aourag, and K. Rajan, *Data mining of Ti–Al semi-empirical parameters for developing reduced order models.* Physica B: Condensed Matter, 2011. **406**(11): p. 2055-2060.

150. Feng, X.T. and C. Yang, *Coupling recognition of the structure and parameters of non‐linear constitutive material models using hybrid evolutionary algorithms.* International journal for numerical methods in engineering, 2004. **59**(9): p. 1227-1250.
151. Alexandrov, N.M., et al., *Optimization with variable-fidelity models applied to wing design*. 1999, DTIC Document.
152. Alexandrov, N.M., et al., *A trust-region framework for managing the use of approximation models in optimization.* Structural Optimization, 1998. **15**(1): p. 16-23.
153. Jäger, J., *Uniaxial deformation of a random packing of particles.* Archive of Applied Mechanics, 1999. **69**(3): p. 181-203.
154. Jaeger, J., *New solutions in contact mechanics*. 2005: Wit Pr/Computational Mechanics.
155. Kuhn, M.R., *Implementation of the Jäger contact model for discrete element simulations.* International Journal for Numerical Methods in Engineering, 2011. **88**(1): p. 66-82.
156. Kuhn, M.R., et al., *Investigation of Cyclic Liquefaction with Discrete Element Simulations.* Journal of Geotechnical and Geoenvironmental Engineering, 2014. **140**(12): p. 04014075.
157. Satake, M., *Constitution of mechanics of granular materials through the graph theory.* Continuum Mechanical and Statistical Approaches in the Mechanics of Granular Materials, 1978: p. 47-62.
158. Pastor, M., O. Zienkiewicz, and A. Chan, *Generalized plasticity and the modelling of soil behaviour.* International Journal for Numerical and Analytical Methods in Geomechanics, 1990. **14**(3): p. 151-190.
159. Pestana, J.M. and A. Whittle, *Compression model for cohesionless soils.* Géotechnique, 1995. **45**(4): p. 611-631.
160. Ling, H.I. and S. Yang, *Unified sand model based on the critical state and generalized plasticity.* Journal of Engineering Mechanics, 2006.
161. Jefferies, M. and K. Been, *Implications for critical state theory from isotropic compression of sand.* Géotechnique, 2000. **50**(4): p. 419-429.
162. Wood, D.M., *Soil behaviour and critical state soil mechanics*. 1990: Cambridge university press.
163. Li, X.-S. and Y. Wang, *Linear representation of steady-state line for sand.* Journal of geotechnical and geoenvironmental engineering, 1998. **124**(12): p. 1215-1217.
164. Been, K. and M.G. Jefferies, *A state parameter for sands.* Géotechnique, 1985. **35**(2): p. 99-112.
165. Nazzal, M.D., M.Y. Abu-Farsakh, and L.N. Mohammad, *Implementation of a critical state two-surface model to evaluate the response of geosynthetic reinforced pavements.* International Journal of Geomechanics, 2010.
166. Andrade, J.E., A.M. Ramos, and A. Lizcano, *Criterion for flow liquefaction instability.* Acta Geotechnica, 2013. **8**(5): p. 525-535.
167. Conn, A.R., N.I. Gould, and P.L. Toint, *Trust region methods*. Vol. 1. 2000: Siam.

168. Marquardt, D.W., *An algorithm for least-squares estimation of nonlinear parameters.* Journal of the Society for Industrial & Applied Mathematics, 1963. **11**(2): p. 431-441.
169. Arulmoli, K., *Velacs verification of liquefaction analyses by centrifuge studies laboratory testing program: Soil data report*. 1992: Earth Technology Corporation.
170. Kammerer, A.M., et al., *Cyclic simple shear testing of Nevada sand for PEER Center project 2051999*. 2000: University of California, Department of Civil Engineering.
171. Charalampidou, E.-M., et al., *Characterization of shear and compaction bands in a porous sandstone deformed under triaxial compression.* Tectonophysics, 2011. **503**(1): p. 8-17.
172. Boon, C., G. Houlsby, and S. Utili, *A new algorithm for contact detection between convex polygonal and polyhedral particles in the discrete element method.* Computers and Geotechnics, 2012. **44**: p. 73-82.
173. Lim, K.W. and J.E. Andrade, *Granular element method for three‐dimensional discrete element calculations.* International Journal for Numerical and Analytical Methods in Geomechanics, 2014. **38**(2): p. 167-188.
174. Salot, C., P. Gotteland, and P. Villard, *Influence of relative density on granular materials behavior: DEM simulations of triaxial tests.* Granular matter, 2009. **11**(4): p. 221-236.
175. Hardin, B.O., *Crushing of soil particles.* Journal of Geotechnical Engineering, 1985. **111**(10): p. 1177-1192.
176. Cheng, Y., M. Bolton, and Y. Nakata, *Crushing and plastic deformation of soils simulated using DEM.* Geotechnique, 2004. **54**(2): p. 131-141.
177. Lade, P.V., J.A. Yamamuro, and P.A. Bopp, *Significance of particle crushing in granular materials.* Journal of Geotechnical Engineering, 1996. **122**(4): p. 309-316.
178. ASTM, *D4253, Standard test methods for maximum index density and unit weight of soils using a vibratory table. ASTM International, West Conshohocken, Pa*. 2006(a).
179. ASTM, *D4254, Standard test methods for minimum index density and unit weight of soils and calculation of relative density. ASTM International, West Conshohocken, Pa*. 2006(b).
180. Hardin, B.O. *The nature of stress-strain behavior for soils*. in *From Volume I of Earthquake Engineering and Soil Dynamics--Proceedings of the ASCE Geotechnical Engineering Division Specialty Conference, June 19-21, 1978, Pasadena, California. Sponsored by Geotechnical Engineering Division of ASCE in cooperation with:*. 1978.
181. Wichtmann, T. and T. Triantafyllidis, *Influence of the grain-size distribution curve of quartz sand on the small strain shear modulus G max.* Journal of Geotechnical and Geoenvironmental Engineering, 2009. **135**(10): p. 1404-1418.

182. Cho, G.-C., J. Dodds, and J.C. Santamarina, *Particle shape effects on packing density, stiffness, and strength: natural and crushed sands.* Journal of Geotechnical and Geoenvironmental Engineering, 2006. **132**(5): p. 591-602.
183. Lade, P.V., *Failure criterion for cross-anisotropic soils.* Journal of geotechnical and geoenvironmental engineering, 2008. **134**(1): p. 117-124.
184. Kutter, B.L., Y.-r. Chen, and C. Shen, *Triaxial and torsional shear test results for sand*. 1994, DTIC Document.
185. Andrade, J.E., et al., *Granular element method for computational particle mechanics.* Computer Methods in Applied Mechanics and Engineering, 2012. **241**: p. 262-274.
186. Bensoussan, A., J.-L. Lions, and G. Papanicolaou, *Asymptotic analysis for periodic structures*, in *Studies in Mathematics and Its Applications*. 1978, Elsevier: Amsterdam.
187. Sanchez-Palencia, E., *Non-homogeneous media and vibration theory*. 1980, Amsterdam: North-Holland Publishing Company.
188. Aboudi, J., *Mechanics of composite materials - a unified micromechanical approach*, in *Studies in Applied Mechanics*. 1991, Elsevier: Amsterdam.
189. Aboudi, J., *Micromechanical Analysis of Composites by the Method of Cells.* Applied Mechanics Reviews, 1989. **42**(7): p. 193-221.
190. Ghosh, S., K. Lee, and S. Moorthy, *Multiple scale analysis of heterogeneous elastic structures using homogenization theory and voronoi cell finite element method.* International Journal of Solids and Structures, 1995. **32**(1): p. 27-62.
191. Ghosh, S. and S. Moorthy, *Elastic-plastic analysis of arbitrary heterogeneous materials with the Voronoi Cell finite element method.* Computer Methods in Applied Mechanics and Engineering, 1995. **121**(1–4): p. 373-409.
192. Aboudi, J., *A continuum theory for fiber-reinforced elastic-viscoplastic composites.* International Journal of Engineering Science, 1982. **20**(5): p. 605-621.
193. Chen, J.-S., et al., *Reproducing Kernel Particle Methods for large deformation analysis of non-linear structures.* Computer Methods in Applied Mechanics and Engineering, 1996. **139**(1–4): p. 195-227.
194. Chen, J.-S., et al., *A stabilized conforming nodal integration for Galerkin mesh-free methods.* International Journal for Numerical Methods in Engineering, 2001. **50**(2): p. 435-466.
195. Moore, B., *Principal component analysis in linear systems: Controllability, observability, and model reduction.* Automatic Control, IEEE Transactions on, 1981. **26**(1): p. 17-32.
196. Green, M., *A relative error bound for balanced stochastic truncation.* Automatic Control, IEEE Transactions on, 1988. **33**(10): p. 961-965.

197. Glover, K., *All optimal Hankel-norm approximations of linear multivariable systems and their L ∞-error bounds.* International Journal of Control, 1984. **39**(6): p. 1115-1193.
198. Krysl, P., S. Lall, and J.E. Marsden, *Dimensional model reduction in non-linear finite element dynamics of solids and structures.* International Journal for Numerical Methods in Engineering, 2001. **51**(4): p. 479-504.
199. Dvorak, G.J., *Transformation Field Analysis of Inelastic Composite Materials.* Proceedings: Mathematical and Physical Sciences, 1992. **437**(1900): p. 311-327.
200. Bahei-El-Din, Y.A., A.M. Rajendran, and M.A. Zikry, *A micromechanical model for damage progression in woven composite systems.* International Journal of Solids and Structures, 2004. **41**(9–10): p. 2307-2330.
201. Fish, J., et al., *Computational plasticity for composite structures based on mathematical homogenization: Theory and practice.* Computer Methods in Applied Mechanics and Engineering, 1997. **148**(1–2): p. 53-73.
202. Fish, J., Q. Yu, and K. Shek, *Computational damage mechanics for composite materials based on mathematical homogenization.* International Journal for Numerical Methods in Engineering, 1999. **45**(11): p. 1657-1679.
203. Oskay, C. and J. Fish, *Eigendeformation-based reduced order homogenization for failure analysis of heterogeneous materials.* Computer Methods in Applied Mechanics and Engineering, 2007. **196**(7): p. 1216-1243.
204. Oskay, C. and J. Fish, *On calibration and validation of eigendeformation-based multiscale models for failure analysis of heterogeneous systems.* Computational Mechanics, 2008. **42**(2): p. 181-195.
205. Yuan, Z. and J. Fish, *Multiple scale eigendeformation-based reduced order homogenization.* Computer Methods in Applied Mechanics and Engineering, 2009. **198**(21–26): p. 2016-2038.
206. Fish, J. and Z. Yuan, *Bridging the Scales in Science and Engineering*. 2008, London: Oxford University Press.
207. Talreja, R., *Transverse Cracking and Stiffness Reduction in Composite Laminates.* Journal of Composite Materials, 1985. **19**(4): p. 355-375.
208. Allen, D.H., C.E. Harris, and S.E. Groves, *A thermomechanical constitutive theory for elastic composites with distributed damage—I. Theoretical development.* International Journal of Solids and Structures, 1987. **23**(9): p. 1301-1318.
209. Allen, D.H., C.E. Harris, and S.E. Groves, *A thermomechanical constitutive theory for elastic composites with distributed damage—II. Application to matrix cracking in laminated composites.* International Journal of Solids and Structures, 1987. **23**(9): p. 1319-1338.

210. Allix, O., et al., *Damage mechanics for composite laminates under complex loading*. Yielding Damage and Failure of Anisotropic Solids, EGF5. 1990, London: Mechanical Engineering Publications. 551-569.
211. Ladevèze, P., A. Gasser, and O. Allix, *Damage Mechanisms Modeling for Ceramic Composites.* Journal of Engineering Materials and Technology, 1994. **116**(3): p. 331-336.
212. Kattan, P.I. and G.Z. Voyiadjis, *Overall damage and elastoplastic deformation in fibrous metal matrix composites.* International Journal of Plasticity, 1993. **9**(8): p. 931-949.
213. Chow, C.L. and F. Yang, *Three-Dimensional Inelastic Stress Analysis of Center Notched Composite Laminates with Damage.* International Journal of Damage Mechanics, 1997. **6**(1): p. 23-50.
214. Chaboche, J., O. Lesne, and T. Pottier, *Continuum damage mechanics of composites: Towards a unified approach*. Damage Mechanics in Engineering Materials. 1998, Amsterdam: Elsevier.
215. Kanouté, P., et al., *Multiscale Methods for Composites: A Review.* Archives of Computational Methods in Engineering, 2009. **16**(1): p. 31-75.
216. Bazant, Z.P. and J. Planas, *Fracture and size effect in concrete and other quasibrittle materials*. Vol. 16. 1997: CRC press.
217. Chow, C. and J. Wang, *An anisotropic theory of elasticity for continuum damage mechanics.* International Journal of Fracture, 1987. **33**(1): p. 3-16.
218. Sidoroff, F., *Description of anisotropic damage application to elasticity*, in *Physical Non-Linearities in Structural Analysis*, J. Hult and J. Lemaitre, Editors. 1981, Springer. p. 237-244.
219. Simo, J. and J. Ju, *Strain-and stress-based continuum damage models—I. Formulation.* International journal of solids and structures, 1987. **23**(7): p. 821-840.
220. Kalthoff, J. and S. Winkler, *Failure mode transition at high rates of shear loading*, in *International conference on impact loading and dynamic behavior of materials*. 1988. p. 185-195.
221. Song, J.-H., H. Wang, and T. Belytschko, *A comparative study on finite element methods for dynamic fracture.* Computational Mechanics, 2008. **42**(2): p. 239-250.
222. Jiang, H., et al., *The strength and toughness of cement reinforced with bone-shaped steel wires.* Composites science and technology, 2000. **60**(9): p. 1753-1761.
223. Salvi, A.G., A.M. Waas, and A. Caliskan, *Energy absorption and damage propagation in 2D triaxially braided carbon fiber composites: effects of in situ matrix properties.* Journal of Materials Science, 2008. **43**(15): p. 5168-5184.
224. Bailakanavar, M., et al., *Automated modeling of random inclusion composites.* Engineering with Computers, 2014. **30**(4): p. 609-625.
225. Wentorf, R., Collar, R., Shephard M.S., Fish, J., *Automated modeling for complex woven mesostructures.* Comput. Meth. Appl. Mech. Engng, 1999. **172**(1): p. 273-291.

226. Gusev, A.A., *Representative volume element size for elastic composites: a numerical study.* Journal of Mechanics and Physics of Solids, 1997. **45**: p. 1449-59.

227. Gusev, A.A., Heggli, M., Lusti, H.R., Hine, P.J., *Orientation averaging for stiffness and thermal expansion of short fiber composites.* Advanced Engineering Materials, 2002. **4**(12): p. 931-933.

228. Duschlbauer, D., Bohm, H.J., Pettermann, H.E., *Computational Simulation of Composites Reinforced by Planar Random Fibers: Homogenization and Localization by Unit Cell and Mean Field Approaches* Journal of Composite Materials, 2006. **40**(24): p. 2217–2234.

229. Widom, B., *randomsequential adition of hard spheres to a volume.* Journal of Chemical Physics, 1966. **44**(10): p. 3888-3894.

230. Bohm, H.J., Eckschlager, A., Han, W., , *Multinclusion unit cell models for metal matrix composites with randomly oriented discontinuous reinforcements.* Computational Materials Science, 2002. **25**: p. 42-53.

231. Torquato S., H.H., *Random heterogeneous materials: microstructure and macroscopic properties.* Applied Mechanics Reviews, 2002. **55**(4): p. B62.

232. Williams, S.R., Philipse, A.P., *Random packing of spheres and spherocylinders simulated by mechanical contraction.* Physics review E, 2003. **67**: p. 051301-1-9.

233. Tu, S.T., Cai, W.Z., Yin, Y., Ling, X., *Numerical simulationof saturation behavior of physical properties in composites with randomlyu distributed second phase.* Journal of Composite Materials, 2005. **39**(7): p. 671-631.

234. Kari, S., Berger, H., Gabbert, U., *Numerical evaluation of effective material properties of randomly distributed short cylindrical fiber composites.* Computational Materials Science, 2007. **39**: p. 198-204.

235. Pan, Y., Iorga, L., Pelegri, A.A., *Numerical generation of a random chopped fiber composite RVE and its elastic properties.* Composites Science and Technology, 2008. **68**: p. 2792-2798.

236. Toll, S., *Packing mechanics of fiber reinforcements.* Polymer Engineering and Sciemce, 1998. **38**(18): p. 1337-1350

237. Lubachevsky, B.D., Stillinger, F.H., *Geometric properties of random disk packings.* Journal of Statistical Physics, 1990. **60**: p. 561-583.

238. Stafford DS., J.T., *Unisng level sets for creating virtual random packs of non spherical convex shapes.* Journal of COmputational Physics, 2010. **229**(9): p. 3295-3315.

239. Hinrichsen, E.L., Feder, J., Jossang, T., *Geometry of random sequential adsorption.* Journal of Statistical Physics, 1986. **44**: p. 793-827.

240. Cooper, D.W., *Random sequential packing simulations in three dimensions for spheres.* Physics Review A, 1988. **38**: p. 522-524.

241. Sherwood, J.D., *Packing of spheroids in three-dimensional space by random sequential addition.* Journal of Physics A, 1997. **30**(24).
242. Evans, K.E., Ferrar, M.D., *The packing of thick fibers.* Journal of Physics D, 1989. **22**: p. 354-360.
243. Parkhouse, J.G., Kelly, A., *The random packing of fibers in three dimensions.* Proceedings: Mathematical and Physical Sciences, 1995. **451**(1943): p. 737-746.
244. Evans, K.E., Gibson, A.G., *Prediction of the maximum packing fraction achievable in randomly oriented short fiber-composites.* Composites Science and Technology, 1986. **25**: p. 149-162.
245. Eberley, D. *Intersection of convex objects: The method of separating axis*. 2001; Available from: http://www.geometrictools.com/.
246. Stafford, D.S. and T.L. Jackson, *Using level sets for creating virtual random packs of non-spherical convex shapes.* Journal of Computational Physics, 2010. **229**(9): p. 3295-3315.
247. Hughes, T.J.R., J.A. Cottrell, and Y. Bazilevs, *Isogeometric analysis: CAD, finite elements, NURBS, exact geometry and mesh refinement.* Computer Methods in Applied Mechanics and Engineering, 2005. **194**(39–41): p. 4135-4195.